

Integrated analysis of wind turbines - The impact of power systems on wind turbine design

Barahona Garzón, Braulio; Sørensen, Poul Ejnar; Hansen, Anders Melchior; Hansen, Anca Daniela; Cutululis, Nicolaos Antonio

Publication date:
2012

Document Version
Publisher's PDF, also known as Version of record

[Link back to DTU Orbit](#)

Citation (APA):
Barahona Garzón, B., Sørensen, P. E., Hansen, A. M., Hansen, A. D., & Cutululis, N. A. (2012). Integrated analysis of wind turbines - The impact of power systems on wind turbine design. Kgs. Lyngby: Technical University of Denmark (DTU).

DTU Library Technical Information Center of Denmark

General rights

Copyright and moral rights for the publications made accessible in the public portal are retained by the authors and/or other copyright owners and it is a condition of accessing publications that users recognise and abide by the legal requirements associated with these rights.

- Users may download and print one copy of any publication from the public portal for the purpose of private study or research.
- You may not further distribute the material or use it for any profit-making activity or commercial gain
- You may freely distribute the URL identifying the publication in the public portal

If you believe that this document breaches copyright please contact us providing details, and we will remove access to the work immediately and investigate your claim.

Integrated analysis of wind turbines – The impact of power systems on wind turbine design

Braulio Barahona

Ph.D. Thesis, January 2012

This report was prepared by

Braulio Barahona

Supervisors at DTU Wind Energy

Poul Sørensen

Nicolaos A. Cutululis

Anca D. Hansen

Anders H. Hansen

DTU Wind Energy
Technical University of Denmark
Frederiksborgvej 399
4000 Roskilde
Denmark

www.vindenergi.dtu.dk
Tel: (+45) 46 77 46 77
Fax: (+45) 46 77 56 88
E-mail: risoe@risoe.dk

Release date:	XX-XXX-2012
Category:	1 (public)
Edition:	First
Comments:	This report is part of the requirements to achieve the Philosophy Doctorate in Engineering at the Technical University of Denmark.
Rights:	©Braulio Barahona, 2012

Preface

This thesis was prepared at the Technical University of Denmark, DTU Wind Energy , in partial fulfillment of the requirements for acquiring the Ph.D. degree in engineering.

The Ph.D. project has been carried out at DTU Wind Energy, in the Wind Energy Systems Programme and in collaboration with the Aeroelastic Design Programme.

The Danish Energy Agency is acknowledged for funding partly this work in contract number EFP07-II for the EFP project titled “Integrated design of wind power systems.”

I would like to acknowledge the people that have collaborated in this Ph.D. project, that has been largely multidisciplinary: Peter Bjørn Andersen, Lars Henriksen, Helen Markou, and Anders M. Hansen from the aeroelastic group, and my supervisors and colleagues at the wind energy systems group Poul, Nikos, and Anca.

Braulio Barahona

Roskilde, January 2012

Summary

Megawatt-size wind turbines nowadays operate in very complex environmental conditions, and increasingly demanding power system requirements. Pursuing a cost-effective and reliable wind turbine design is a multidisciplinary task. However nowadays, wind turbine design and research areas such as aeroelastic and mechanical, electrical and control, and grid integration, make use of simulation tools dedicated to specific areas. Practical experience shows there is a need to bridge the expertise from different design areas.

The focus of this Ph.D. study is on the integrated dynamic analysis of operating conditions that stem from disturbances in the power system. An integrated simulation environment, wind turbine models, and power system models are developed in order to take an integral perspective that considers the most important aeroelastic, structural, electrical, and control dynamics.

Applications of the integrated simulation environment are presented. The analysis of an asynchronous machine, and numerical simulations of a fixed-speed wind turbine in the integrated simulation environment, demonstrate the effects on structural loads of including the generator rotor fluxes dynamics in aeroelastic studies. Power system frequency control studies of variable-speed wind turbines with the integrated simulation environment, show that is possible to make a sensible estimation of the contribution of a wind farm to power system frequency control, while studying the impact on wind turbine structural loads.

Finally, studies of the impact that voltage faults have on wind turbine loads are presented. The case of unbalanced faults is addressed, the possibilities and drawbacks for reduction of structural loads using electrical control actions is investigated. Load reduction using resonant damping control is proven and quantified.

Contents

Preface	i
Summary	ii
Notation	viii
List of Figures	x
List of Tables	xiii
1 Introduction	1
1.1 Background	1
1.2 Motivation	3
1.3 Integrated analysis and design	3
1.4 Objectives	5
1.5 Outline and contributions	5
2 Integrated dynamic analysis environment	7
2.1 Conceptual framework	7
2.2 Framework for simulation environment	8
2.2.1 Model formulation	10
2.2.2 Existing software	11

2.2.3	Simulator coupling schemes	14
2.3	HAWC2 – Matlab simulation environment	15
2.3.1	Options for interfacing with Matlab	16
2.3.2	HAWC2-Matlab coupling	19
2.4	Summary	23
3	General description of models	24
3.1	Overview	24
3.2	Wind turbine model	25
3.2.1	Aeroelastic model	26
3.2.2	Drive train model	29
3.2.3	Generator system	30
3.2.4	Blade angle control	39
3.3	Power system models	41
3.3.1	Background for power system model development . . .	41
3.3.2	Grid equivalent model	42
3.3.3	Model for frequency control	43
3.4	Summary	44
4	Application examples	46
4.1	Dynamic analysis of fixed-speed wind turbine	46
4.1.1	Analysis of asynchronous generator	46
4.1.2	Numerical simulation of fixed-speed wind turbine . . .	48
4.2	Dynamic analysis of wind turbines providing frequency support	55
4.3	Summary	60
5	Impact of voltage faults on wind turbine structural loads	61
5.1	Introduction	61
5.2	Balanced voltage fault	63
5.2.1	Wind disturbances and fault	63
5.2.2	Fault and reconnection	68

5.3	Unbalanced voltage fault	71
5.3.1	Torque oscillations due to unbalanced voltage	71
5.3.2	Review of control techniques	72
5.3.3	1-Hz equivalent loads	73
5.3.4	Simulation results	73
5.3.5	Quantification of load reduction	74
5.4	Summary	82
6	Conclusions	83
	Publication list	85
	Appendix	87
A	Modeling of asynchronous generator	87
A.1	Basic concepts.	87
A.1.1	Symmetry.	88
A.2	Steady-state model.	89
A.2.1	Torque and power characteristic.	91
A.3	Dynamic model.	93
A.3.1	Voltage equations.	94
A.3.2	Selection of reference frame.	98
A.3.3	state space model.	102
A.3.4	Dynamic response of asynchronous machine.	104
A.3.5	Control of doubly-fed asynchronous generator.	108
B	Linear transformations	111
B.1	Inversion of transformation matrix	111
C	DFAG initialization	113
D	Toy example in HAWC2	116

D.1	Natural frequency of disc-rod system	116
D.2	Simulation of disc-shaft-disc system	119
D.2.1	Free - free torsional vibration	120
D.2.2	Numerical damping	120
D.3	Summary	121
List of references		123

Notation

$\dot{(\)}$ Derivative with respect to time.

f Frequency in Hz.

θ Angular position in rad, or degrees (mechanical or electrical).

i instantaneous current, subindices will indicate the frame and the corresponding circuit.

I_s Per-phase stator current, complex variable whose magnitude is an RMS value.

I'_r Per-phase rotor current referred to stator side, whose magnitude is an RMS value.

λ flux linkages (i.e. fluxlinkage times angular speed is a voltage induced by the rotation of a circuit).

$\dot{\lambda}$ flux linkages per second (i.e. voltage induced by change of flux with time).

\mathcal{L}_m Magnetizing inductance.

$\mathcal{L}_s, \mathcal{L}_r$ stator, rotor self-inductances.

L_m Per-phase magnetizing inductance.

L_{ms}, L_{mr} Stator, rotor self-magnetizing inductance.

L_s, L_r Stator, rotor self-inductance.

L_{sr} Stator-to-rotor mutual inductance.

L_{ss}, L_{rr} Stator-to-stator, rotor-to-rotor mutual inductance.

N_{gb} Gearbox ratio.

ω Angular speed in rad/s.

p_f Number of magnetic poles in the rotor.

R_c Equivalent per-phase resistance of magnetic core.

R_r Per-phase resistance of rotor windings.

R'_r Rotor resistance R_r referred to stator side.

R_s Per-phase resistance of stator windings.

s Slip.

S_{gsc} Grid-side power converter apparent power.

S_s Stator apparent power.

U_n RMS line-to-line voltage.

v instantaneous voltage, subindices will indicate the frame and the corresponding circuit.

V_r RMS per-phase rotor voltage.

V'_r Rotor voltage V_r referred to stator side.

V_s RMS per-phase stator voltage.

X_m Per-phase magnetizing reactance.

X_r Per-phase leakage reactance of rotor windings.

X'_r Rotor leakage reactance X_r referred to stator side.

X_s Per-phase leakage reactance of stator windings.

List of Figures

2.1	Illustration of wind turbine design process	8
2.2	Illustration of wind turbine integral design framework	9
2.3	Illustrations of simulator coupling schemes	15
2.3	Illustrations of simulator coupling schemes	16
2.4	Available external interfaces to HAWC2	16
2.5	HAWC2 - Matlab interfacing using shared libraries and TCP/IP sockets	20
2.6	Flowchart of integrated dynamic analysis environment	21
3.1	Block diagram of models for integrated analysis of wind turbines	25
3.2	Illustration of wind turbine subsystems.	25
3.3	Structural and standard drive train model implemented in HAWC2	28
3.4	Block diagram of first-order generator model.	30
3.5	Block diagram of Asynchronous generator model.	32
3.6	Block diagram of Doubly-fed Asynchronous generator model.	33
3.7	Doubly-fed asynchronous generator control.	33
3.8	Inertia response control -based on torque set point.	35
3.9	Inertia response control -based on power set point.	35
3.10	Damping control for balanced fault operation.	36

3.11 Proportional set point damper for balanced fault operation. . .	36
3.12 Damping control for unbalanced supply voltage operation. . .	36
3.13 Illustration of a resonant filter used for resonant damping control (RDC).	37
3.14 Damping control plus compensators resonant filters with phase compensation (RD-Comp control).	38
3.15 Resonant damping control with switching functions (RD-SW): q -axis loop (d -axis has the same structure with the variables corresponding to those of d -axis of normal operation control)	39
3.16 Blade angle control for fixed-speed wind turbine	40
3.17 Blade angle control for variable-speed wind turbine.	40
3.18 Line diagram of grid equivalent model.	42
3.19 Power system model for frequency control.	44
4.1 Eigen values of asynchronous machine with short circuited rotor, over different operating points of generator mode -blue lines are read with the vertical axis on the left, read lines are red with the vertical axis on the right.	47
4.2 Wind speed, blade angle and power	49
4.3 Top and bottom tower bending moments, from top to bottom: tilt, side-to-side, and yaw.	50
4.4 Blade root moments	51
4.5 Spectrum of blade root bending moments and electromagnetic torque	52
4.6 Spectra of tower bottom bending moments and electromag- netic torque	53
4.7 Spectra of shaft bending moments and electromagnetic torque	53
4.8 Comparison of spectra with full-order, and slip generator model.	54
4.9 Integrated dynamic analysis model for power system frequency control.	56
4.10 Power system response to loss of generation	57
4.11 Wind turbine loads while emulating inertia.	59

5.1	Block diagram illustrating the subsystems modeled with the main variables they exchange, (blue quantities are references or measurements).	64
5.2	Case 1. Response to wind gust, turbulent wind, and AC fault.	65
5.2	Case 1. Response to wind gust, turbulent wind, and AC fault.	67
5.3	Case 2. Response to AC fault with over-current protection	69
5.3	Case 2. Response to AC fault with over-current protection	70
5.4	Voltage at stator terminals at start of unbalanced fault.	74
5.5	Electrical loads from top to bottom: rotor voltage and current, total active power and stator active power. In each plot, normal operation with dash-dot (normal), unbalanced fault with RD-SW in solid thick (damper), and unbalanced fault with normal control in solid thin line (unctrl.fault).	75
5.6	Structural loads from top to bottom: shaft torsion , tower bottom (T.B.) and tower top (T.T.) side-to-side moment. In each plot, normal operation with dash-dot (normal), unbalanced fault with RD-SW in solid thick (damper), and unbalanced fault with normal control in solid thin line (unctrl.fault).	76
5.7	Normalized 1-Hz equivalent loads vs. turbulence intensity.	79
5.8	Comparison of extreme loads given different levels of turbulence intensity, from left to right shaft torsion, tower bottom (T.B.), and tower top (TP).	80
5.9	Comparison maximum values of rotor voltage (left), and current (right) magnitude given different levels of turbulence intensity	80
5.10	Rotor voltage magnitude vs. 1-Hz equivalent loads for different values of control gain H_1	81
A.1	Simplified diagram of asynchronous machine (the rotor voltage is $V_r = 0$ in an induction machine, and in the case of a doubly-fed machine it is supplied by a power converter).	89
A.2	Per-phase diagram of asynchronous generator (rotor quantities are referred to stator side).	90
A.3	Per-phase equivalent circuit of asynchronous generator. This signs of voltages and currents are set with motor convention, which is the most common.	91

A.4	Asynchronous machine steady-state torque.	92
A.5	Asynchronous machine steady-state active, and reactive power.	92
A.6	Contour plots of DFAG torque (top $s - \theta$ for two values of $ V_r $, bottom $s - V_r $ for two values of θ).	93
A.7	Contour plots of DFAG $ S_{\text{tot}} $, $ I_r $, and T_{em} at nominal slip (top left the control variable V_r).	94
A.8	Representation of functions of time as space-vectors in a planar space. Given a 3-phase balanced system (i.e. $f_a = \text{Re} [Ae^{j\omega t}]$, $f_b = \text{Re} [Ae^{j(\omega t - \frac{2\pi}{3})}]$, and $f_c = \text{Re} [Ae^{j(\omega t + \frac{2\pi}{3})}]$), the resultant of such vector set would be a vector with an amplitude A that rotates in space at an angular speed ω	95
A.9	Torque characteristic	104
A.10	Transient response of asynchronous machine	106
A.11	Eigen values of asynchronous machine with short circuited rotor, over different operating points.	108
B.1	Illustration of linear transformation.	112
C.1	Initialization of DFAG control variables	115
D.1	Disc-rod system	117
D.2	Natural frequency of disc-rod system	119
D.3	Disc-shaft-disc system	120
D.4	Natural frequency of disc-shaft-disc system –with $\beta = 0.27$ and $\gamma = 0.51$	121
D.5	Natural frequency of disc-shaft-disc system –with $\beta = 0.26$ and $\gamma = 0.50$	122

List of Tables

2.1	Software for dynamic analysis	12
4.1	Eigen values of asynchronous generator at 0.4% slip.	48
4.2	P-frequencies at $\omega_h = 1.9713$ rad/s	50
A.1	Asynchronous machine data ($p_f = 4$)	91
A.2	DFAG data ($p_f = 4$)	93
D.1	Data for disc-rod system	117
D.2	Data of disc-shaft-disc system	120

Introduction

This work is in the area of dynamic analysis of wind turbines. The focus is on the analysis of operating conditions that stem from disturbances in the power system. The approach is to take an integral perspective that considers the most important aeroelastic, structural, electrical, and control dynamics. For this purpose, a simulation environment and wind turbine models are developed.

Concepts and design details of the simulation environment are described in Chapter 2. Models of wind turbine subsystems and controls, and power systems models are described in Chapter 3. Applications of this integrated design analysis environment and models are illustrated with two examples in Chapter 4. Analysis of the impact of voltage faults on wind turbine structural loads, and reduction of loads are presented in Chapter 5. Conclusions and further work are discussed in Chapter 6.

1.1 Background

The design objective of modern wind turbines has evolved from medium-size wind turbines connected to distribution grids, to large offshore wind farms connected to the transmission level of power systems. Megawatt-size wind turbines nowadays operate in very complex environmental conditions, and increasingly demanding power system requirements. Therefore it is important to improve the understanding of their overall dynamics, and interaction amongst different subsystems, in order to achieve a cost-effective and reliable

design.

Pursuing an integral design is a multidisciplinary task that can be undertaken from different perspectives, in any case it should include an analysis stage. Modern engineering design relies on computational codes for dynamic analysis as part of the design cycle, however in wind turbine design practice such codes are oriented to specific disciplines. Some of the earlier attempts to bridge design areas are [1, 2], where a database of models in different specialized software is created with the vision to use it to optimize wind turbine designs. The specialized software packages considered covered aeroelasticity –HAWC–, power systems –PowerFactory–, power electronics –Saber–, and control design –Matlab/Simulink–. Control design and generic models created in Matlab were input to the other software, a description of such models can be found in [3].

In the design cycle, once a given preliminary design is drafted –optimal or not, it is important to analyze the global dynamics to verify the design in terms of stability and loads. Therefore the interest in coupling computational codes oriented to different disciplines, for example the coupling of aeroelastic with hydroelastic codes for analyzing floating offshore wind turbines [4].

On the other hand, many issues regarding the interaction of wind turbines with power systems were outlined when small scale development started back in the 80s-90s [5, 6], for example:

- Inter-machine oscillations,
- Inter-area oscillations,
- Low voltage ride-through, and
- Frequency support

Since then, these issues have been addressed –to some extent, in a large amount of publications mainly dealing with modeling and control of electrical machines and power systems. More recently, the research community has addressed the mechanical and electrical interactions of wind turbine subsystems during low voltage due to faults [7–10]. Wind turbine design standards, and grid codes include some requirements to ride-through faults. However they are generally not considered in the structural wind turbine design nor in the mechanical component design. In the case of frequency support, while it is not yet required by power system operators, it is regarded as a very important feature in order to meet high shares of electricity produced by wind energy. Furthermore, operation of wind turbines under exceptional

meteorological conditions that may imposed prohibiting loads, is also of importance to the operation of modern power systems, and therefore for wind turbine design.

1.2 Motivation

The ambitions to extend the development of wind energy, and other renewable energy sources lies in the need to meet the challenges of climate change. The large expectations to increase the share of electricity produced by wind energy in modern power systems, make the interaction of wind farms with power systems an important research topic for the community. From a technical and economical point of view, improving and proving specific wind turbine designs –and the design process itself if possible!, would lean wind power towards becoming a main stream technology. This is the context that makes the impact of power system conditions on the dynamics of individual wind turbines an important topic.

Nowadays however, wind turbine design and research areas such as aeroelastic and mechanical, electrical and control, and grid integration, make use of simulation tools dedicated to specific areas. Namely, mechanical design of wind turbine components is usually undertaken with tools dedicated to mechanical design, assuming a characteristic loading instead of analyzing the overall dynamics of aeroelastic, mechanical, electrical, and control systems. Similarly, for grid integration studies, power system simulation tools with network models are used to design wind turbine electrical components, while structural loads are analyzed separately in aeroelastic codes. Therefore, the expertise in these design areas is developed independently. Practical experience shows there is a need to bridge the expertise from different design areas.

Ultimately, the motivation of this Ph.D. project is the reduction of the cost of producing electricity from wind energy, and therefore a better understanding of the compromises in the design of wind turbines for large scale power production is a driver for this research, in the hope of helping to close the gaps amongst the design of different wind turbine components.

1.3 Integrated analysis and design

Integrated design and analysis of wind turbines involves variety of topics, those related to simulation tools are particularly relevant [11], because coupling or combining different specialized software [4, 7–9, 12–22], or further developing a given computational code [10, 23, 24] allows an *integrated dy-*

dynamic analysis to shed light on the dynamic interactions of different sub-systems.

Naturally, (1) the design of wind turbines for offshore operation, and (2) the design and development of new wind energy conversion systems, are areas where combination of knowledge from different disciplines is important in order to succeed. Combination of simulation tools in these area has been undertaken, for example the aeroelastic code HAWC2 has been coupled to the marine structures code SIMO/RIFLEX in order to simulate a floating wind turbine concept –HYWIND– [4]. A SIMO/RIFLEX-HAWC2 model of a scaled prototype of HYWIND was developed and tested. Another application is the Aero-Hydro-Elastic Simulation Platform for wave energy systems and floating wind turbines [22]. This simulation platform couples HAWC2 and WASIM –tool for analysis of floating structures–, it has been used to simulate the wind and wave energy platform Poseidon. Furthermore, aeroelastic tools such as FLEX, Bladed, and Phatas have been extended to include hydrodynamic loading models [11], one example when is FLEX and POSEIDON –finite element code for structural analysis– that have been combined to model the dynamic response with different support structures [18]. However, these work do not consider the dynamics of the generator system.

There is also a need from the electrical, and the control perspective, to combine software tools in order to study the dynamic response of wind turbines under specific power system conditions. For example under a voltage fault: (1) HAWC2 and PowerFactory have been interfaced offline to study fixed-speed wind turbines [7, 15, 19], and (2) FAST and Matlab/Simulink to study variable-speed wind turbines [8, 9, 14]. In general it was observed that shaft torsion, and side-to-side tower moment are qualitatively affected during a voltage fault [7–9, 14], in the case of a fixed-speed active stall wind turbine –depending on the control–, the blade flap moments may be affected [15]. Furthermore, the computational approach based on offline interfacing of HAWC2 and PowerFactory, has also been used to quantify the loading imposed on wind turbines that ride-through a voltage fault in [19], it was proven that neither fatigue nor ultimate loads induced by balanced faults on tower and blades are large enough to condition a given wind turbine life-time design verification, meaning that a given fixed-speed active stall wind turbine design would not be challenged by faults nor fault ride-through requirements because other load cases considered in certification standards are more demanding.

1.4 Objectives

The general objective of this Ph.D. project is to develop an integrated design approach to study the dynamic response of wind turbines under specific power system conditions. The purpose is to study the impact of such power system conditions on wind turbine loads and draw conclusion about the influence on wind turbine design.

Given this general objective, a necessary task is to integrate dynamic models of electrical components, controls, and power system, into dynamic analysis codes of wind turbines. The integration of such models such yield a general framework or environment for pursuing integrated analysis and design of wind turbines. However, the objectives of this Ph.D. study are oriented to cases relevant to the stability of power systems, such as low voltage ride-through, and power system frequency control.

1.5 Outline and contributions

Chapter 1. Introduction chapter that presents the background to the multidisciplinary view of wind turbine design undertaken in this study, the motivation that lies on combining simulation tools is stated, the state-of-the-art of integrated design and analysis of wind turbines is presented, and the objectives of this project described.

Chapter 2. This chapter first puts in place the role that the integrated dynamic analysis environment has in the context of a conceptual integrated design framework. It then describes mathematical and technical considerations taken in the development of the integrated dynamic analysis environment. The contribution of this chapter is the development of the software interface that couples the simulation tools in the integrated dynamic analysis environment.

Chapter 3. Wind turbine models and controls, and power system models are presented in this chapter. Those models are used in different research areas, in this study they are developed for integrated dynamic analysis. Most of the controls are generic and some are new. A new damping control for reduction of wind turbine loads under unbalance voltage operation is a contribution of chapter.

Chapter 4. Examples of application of the integrated dynamic analysis environment are presented in this chapter. The first example is an analytical

analysis of a generator, and numerical analysis of a fixed-speed wind turbine, it shows the interaction of electromechanical and structural modes. The second application demonstrates qualitatively, the impact on structural loads of inertial response control of wind turbines, this is the main contribution of this chapter.

Chapter 5. The impact of voltage faults on structural loads is studied in this chapter. The wind turbine structural and electrical response to a balanced fault, and to wind gusts is studied. Furthermore, the impact of unbalance faults on structural and electrical variables is studied and quantified. The contribution of this chapter is the use of the damping control developed in this Ph.D. project to reduce loads structural loads, while demonstrating that the capabilities of the electrical systems are not compromised.

Chapter 6. Final considerations and outlook to future work are discussed in this chapter.

Appendix A. This appendix show a detailed derivation of asynchronous generator dynamic models. The reduced order model derivation is also described in detail. The steady state solution of the dynamic models is verified with that obtained from the steady state equivalent circuit.

Appendix B. Definitions of linear transformations, and a matrix inversion procedure that are relevant for the derivation of the asynchronous generator dynamic models are described in this appendix.

Appendix C. This appendix derives the a system of equations of the doubly-fed asynchronous machine for calculation of control settings from operation conditions, this is useful for initialization and for design.

Appendix D. A toy example that illustrates the construction of a multi-body structure in HAWC2 is presented in this appendix.

Integrated dynamic analysis environment

This section describes an integrated dynamic analysis environment for wind turbines. A concept of an integrated design framework is presented in Section 2.1 with an outlook towards the role that integrated dynamic analysis has within such integrated design process. Section 2.2 gives an overview of the methods, and theories behind the coupling of simulators for the purpose of dynamic simulations. The software interface developed during this Ph.D. project is described in Section 2.3.

2.1 Conceptual framework

A basic picture of the design process of wind turbines is shown in Figure 2.1. The process starts from a preliminary design, with given design requirements, and environmental conditions. The preliminary design provides input parameters to simulation models, that are then used to run dynamic analysis for a series of cases –defined by design requirements and environmental conditions– in order to verify life-time in terms of fatigue, and extreme loads. Once fatigue and extreme loads design criteria are met, the next step is the detail design of individual wind turbine components.

In this thesis an integrated design approach is proposed, as shown in Figure 2.2. The intention is to improve the design verification stage by means of an integrated dynamic analysis, and a design optimization stage. This conceptual framework draws from research on multidisciplinary design op-

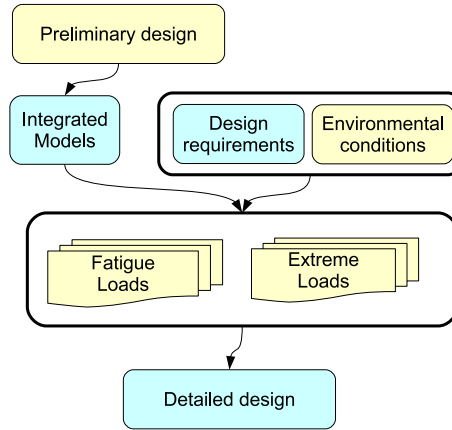


Figure 2.1: Illustration of wind turbine design process

timization (MDO) [25–28], integrated dynamic analysis for offshore wind turbines [4], and design optimization applications to wind turbines [29–33]. The integrated design process illustrated in Figure 2.2 starts by defining

- Integrated models
- Design code requirements –those defined by standards
- Design constraints –those derived from environmental conditions, or specific design objectives

It follows with an iterative process, where parametric dynamic analysis are run until design constraints are met. When the constraints are not met, new parameters of the design are calculated by sensitivity analysis and optimization routines. Once design constraints are met the standard design verification follows.

2.2 Framework for simulation environment

This section discusses some possible frameworks for simulations intended for integrated analysis of wind turbines. Section 2.2.1 describes advantages of using a modular formulation of models, and gives an overview of software available. Section 2.2.3 describes coupling schemes for simulators.

A framework for simulation environment consists in (1) model formulation, and (2) interaction amongst software. These aspects are related, namely in some cases the model formulation will define requirements for software interaction.

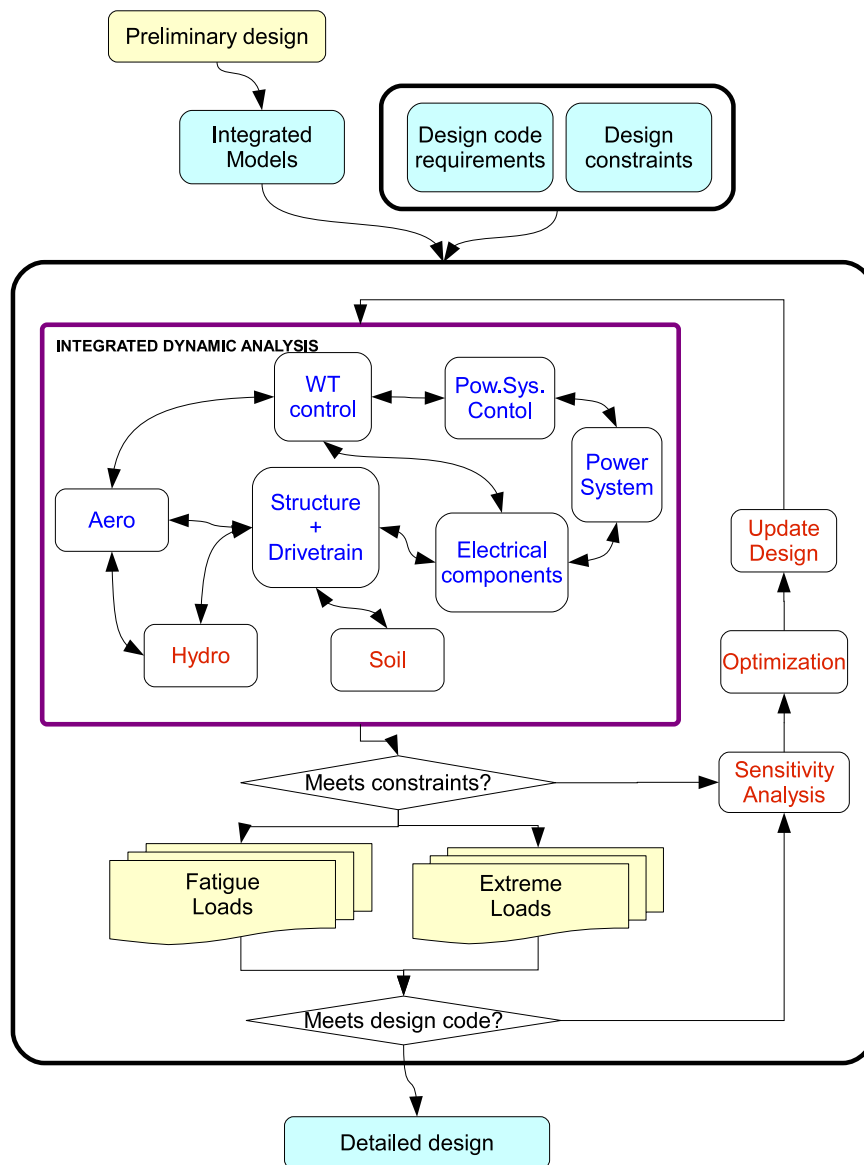


Figure 2.2: Illustration of wind turbine integral design framework

First of all, let us put forward the question of whether *extending a given software package or computational code* to include more domains, or *coupling specialized software* should be the paradigm? There are clearly no simple answers, as there may be very different motivations, advantages, and drawbacks from either. Some motivations may be economical, as for software that is licensed, and therefore provided that there is a market need, extending the capabilities seems appealing; or if building a given interface (for example shared memory) would involve a considerable investment in terms of hardware and manpower. It seems that the industry and academia work in either direction, integrating different software packages or extending a given code. In both cases, finding compromises between detailed models and computation time, investing in new software or developing their own, but certainly with different priorities.

The approach taken in this Ph.D. study was rather pragmatic, though based on well established conventions, the following sections describe

- Two paradigms for model formulation –unified theories, and modular approach in Section 2.2.1
- Software for wind turbine design in Section 2.2.2
- Schemes for coupling of simulators in Section 2.2.3

2.2.1 Model formulation

Mathematical models of complex dynamic systems may be achieved by means of *unified theories*, such as virtual work principle, linear graph theory, and bond graph theory. Another approach is to create submodels based on the physical laws of specific domains, and then to couple these subsystems to model the overall behavior. Although unified theories are appealing for multi domain systems, they still have important limitations, particularly for three dimensional (3D) systems [34]. Virtual work principle, and linear graph theory are computationally very inefficient, virtual work principle loses physical insight when applied in the electrical domain, and bond graph theory requires yet further theoretical development [34].

On the other hand, a *modular approach* [35–40], where subsystems are modeled separately and then coupled together, is used in many fields of engineering because it builds on the formulations, and the tools already developed for specific domains. For example, multibody dynamics allows by its nature to include different descriptions of external forces, and controls [41]. In general, a modular approach also lends it self for multidisciplinary design optimization applications. In this case the challenges are the definition of boundaries of the subsystems, and the input-output variables of the blocks.

Moreover, given the possibility of utilizing different software tools for different domains, the task of coupling simulators may arise numerical, and causality problems.

A modular approach is taken in this study. Taking advantage of the practical benefits from including a detail aeroelastic code that has been developed and verified over many years. This modular approach, uses the aeroelastic code HAWC2, and the interactive environment –and high level programming language– for scientific computations Matlab. Matlab supports Simulink that is a model-based graphical environment for simulations of dynamic systems.

2.2.2 Existing software

In the last few years, wind energy related industry, research, and education has grown substantially. Many general purpose (i.e. finite element analysis –FEA–, dynamic analysis, control, power system analysis) software companies have developed wind turbine models –with varying extend of detail, depending on their main purpose–. A comprehensive list of state-of-the-art wind turbine *design codes* –most of them aeroelastic codes, or FEA/multi-body with aerodynamic modules– that were available in the year 2006 can be found in [42], and a benchmark of aeroelastic codes oriented to offshore wind turbines in [43].

A brief description of some of the relevant codes, and software packages in the context of this work is presented in Table 2.1. State-of-the-art aeroelastic codes, general purpose multibody dynamics (MBD) software that is used in the wind turbine design industry, software for dynamic analysis of complex systems that include wind turbine or wind farm models, and power system analysis software that includes wind turbine and/or wind farm models for stability studies.

Table 2.1: Aeroelastic codes, general purpose MBD software used for wind turbine analysis, software for dynamic analysis of complex systems that include wind turbine models, and power systems analysis software

Name	Additional software	Developer	Description
FAST	AeroDyn, TurbSim	National Energy Laboratory (NREL)	Modal/multibody formulation, 3-bladed wind turbine model with 24 DOF, certified for <i>calculation of onshore wind turbine loads for design and certification</i> , it can interface with Simulink and ADAMS, it can output linearized state matrices [44].
Flex5	stand alone	DTU MEK	Aeroelastic design code, certified, modal formulation, De facto standard tool in Danish industry.
Bladed	stand alone	Garrad Hassan	Modal formulation with the possibility to add drive train and generator degrees of freedom, user-defined models can be added as dynamic libraries, Acciona Windpower has used it to analyzed gearbox dynamics [20].
HAWC2	stand alone	DTU Wind	Aeroelastic code for research, multibody formulation, aerodynamics include dynamic inflow, dynamic stall, skew inflow, shear and induction effects, wind conditions with turbulence in cartesian or polar forms [45]
S4WT	SAMCEF Mecano	SAMTECH	Based on the general purpose SAMCEF Mecano –FEM solver with multibody simulation features–, S4WT can be used load assessment, mechanical and structural component design. It has been used for fatigue load analysis of gearboxes [23].
SimPack	stand alone	SimPack AG	General purpose multibody software, good for: static and quasi-static analyses; analysis of linear systems, and resonance; non-linear transients in time domain; can include aerodynamics, control, and grid; stress/durability; and optimization [46].
MBDyn	stand alone	Dipartimento di Ingegneria Aerospaziale, Politecnico di Milano	General purpose multibody dynamics software, integrated multidisciplinary analysis of multiphysics systems, can be coupled to external solvers [47]
Wind Turbine Model	Simulink® (SimDriveline, SimElectronics, SimHydraulics, SimMechanics, SimPowerSystems, Simscape, Stateflow)	MathWorks	Wind turbine model with 3D mechanical model of tower, nacelle, and blades, blade angle and yaw actuators, simple generator and electrical grid [48].

Continued on Next Page...

Table 2.1 – Continued

Name	Additional software	Developer	Description
Wind Turbine Block set	Matlab [®] /Simulink [®]	Aalborg University, Risø	Wind turbine models used as a <i>general developer tool</i> , then to be implemented in other tools (i.e. Saber, HAWC, DIgSilent) as part of a common simulation platform[1–3].
CDT	Matlab [®] /Simulink [®]	University of Strathclyde	Test bed for controller design, similar input to that of Flex/Bladed[49].
TURBU	stand alone (source code in Matlab)	Energy Research Center of the Netherlands (ECN)	Linear models of 3-bladed wind turbines, aeroelastic models (pre-bend, shear offset, unsteady), allows order reduction of structural models, aimed at control design [39].
MapleSim5	Maplesoft [™]	Maplesoft [™]	Multidomain modeling software, with a broad range of applications from mechatronic systems to design of controllers for wind power.
PowerFactory	stand alone	DIgSILENT	Wind turbine models for stability analysis [50] and wind turbine control [51–53], it can run batch mode, user-defined models develop in DIgSILENT Simulation Language (DSL) and connected to library models by a graphical interface [54]. It can be interfaced with Matlab/Simulink [16], and with HAWC2 [7, 15, 19].
PSCAD [®]	stand alone	Manitoba HVDC Research Centre	Electromagnetic simulation program, it can interface with Matlab [55, 56]
PSAT	Matlab [®] /Simulink [®]	Universidad de Castilla-La Mancha	Library of power systems models in Matlab/Simulink with its own graphical user interface, mostly oriented to optimal power flow studies. It supports also time-domain studies. Though it is for free the documentation has to be bought, it is no longer supported by the author. A similar release in Python (dynamic programming language), designed for multi-core 64-bit Unix platforms is on its way.
PLECS	Matlab [®] /Simulink [®] or stand alone	Plexim GmbH	PLECS is a circuit simulator oriented to complex electrical systems and their controls. The <i>blockset</i> version consists of a model library of power system components –including electrical machines and drives, with graphical representation and manipulation of models, drawing from Simulink environment and using it to solve the systems circuit and control equations.

2.2.3 Simulator coupling schemes

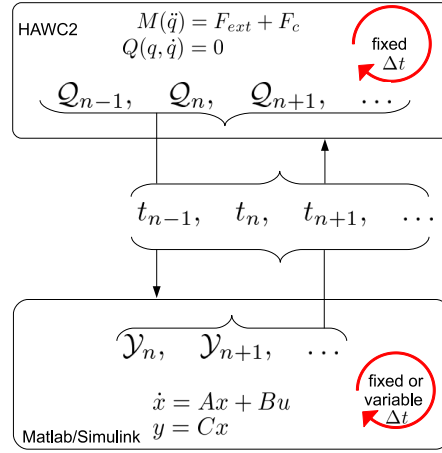
Coupling of simulators for numerical simulations of systems that extend over different domains has been done, for example, in [57] where two simulators for electro-thermal simulations of circuits are coupled together in a scheme of *step size control*. Namely, the time step is variable, depending on the convergence properties of the systems. The coupling of the simulators works using an extrapolation of the interface variables \mathcal{Q}_A , from t_n to t_{n+k} of simulator A, to solve subsystem 1 in simulator B. Then the interface variables \mathcal{Y}_B of simulator B are used to solve subsystem 2 in simulator A for time steps smaller than t_{n+k} , while a given error criterion is met. When the criterion is no longer met the next time step is defined t_{n+e} , and another extrapolation of \mathcal{Q}_A at a new time interval is taken. Such coupling is similar to that referred to as a *non iterative* simulator coupling in [35], and a *walking* time stepping method in [37]. [35] presents a *block* representation of a simple multibody system, and investigates the coupling of simulators with non iterative, and iterative schemes. It concluded that the stability of non iterative schemes is not guaranteed if the systems solved have algebraic loops.

The concept of iterative, and non iterative simulator coupling schemes are illustrated in Figure 2.3 between HAWC2 and Matlab, where \mathcal{Q} and \mathcal{Y} are the interface variables from HAWC2 to Matlab, and vice versa. t is the synchronization time step. The variables from HAWC2 to Matlab can be states (i.e. q, \dot{q}) or other variables like wind speed for example. The variables from Matlab to HAWC2 are the output of models and control variables, for example electromagnetic torque, and blade angle. HAWC2 uses the generic fixed step Newmark integration scheme, that is typical in multibody codes. Matlab/Simulink has a variety of variable and fixed step solvers.

The interface between HAWC2 and Matlab developed in this Ph.D. study, is tested with a non iterative coupling scheme as that in Figure 2.3a. Furthermore, when this scheme is used with a variable step solver in Matlab, an estimator of the interfaced variables that are send from HAWC2 to Matlab is used. This simulator coupling scheme is similar to that of *step size control*, except that in this case there is a *synchronization* time-step predefined, and is kept constant throughout a simulation. The selection of *synchronization* time-step guarantees that the interface variables do not change severely between time steps. The time-step in HAWC2 solver is the same as the *synchronization* time-step. Therefore, it is heuristically chosen to be small enough to represent the fastest dynamics in the system modeled with HAWC2, usually in the range of 0-20 Hz, a time-step in the range of 0.01-0.001 s proved sufficient. The selection of the estimator influences the accuracy, and the computational time. A first order estimator on the interface variables from HAWC2 is proven to give good results. Upon a

good selection of synchronization time-step this non iterative scheme with estimator, is robust, and theoretically faster than an iterative scheme.

The iterative scheme in Figure 2.3b, involves a routine that (1) estimates an output \hat{y}_n , (2) calculates interface variables \mathcal{Y} , (3) HAWC2 then solves its system and returns interface variables Q , (4) Matlab calculates output y_n and compares it to the estimation \hat{y}_n , (5) if the error is met then goes on to the next time-step, otherwise it makes another estimation \hat{y}_n and repeats the sequence for the same time-step.



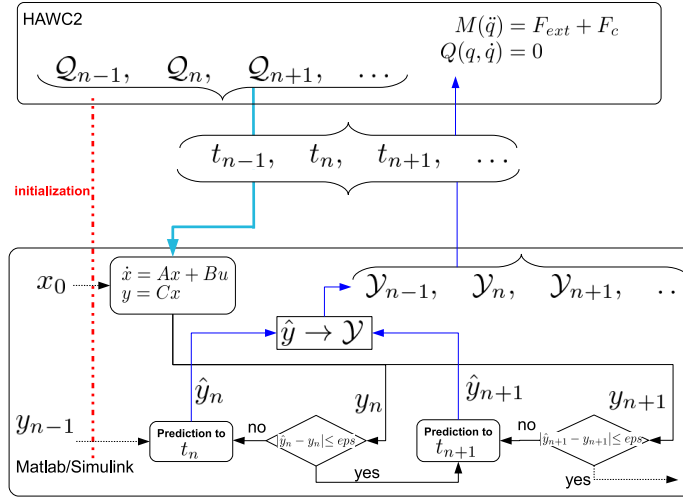
(a) Non iterative simulator coupling

Figure 2.3: Illustrations of simulator coupling schemes

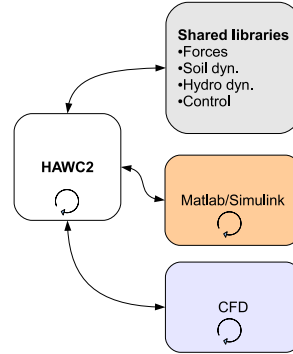
2.3 HAWC2 – Matlab simulation environment

This section describes an integrated dynamic analysis environment with HAWC2-Matlab/Simulink –that is the core of this project. Having HAWC2 a multibody dynamics formulation of the structure it lends itself for interacting with other simulators, Figure 2.4 illustrates the available external interfaces available. Share libraries (i.e. dlls) include external forces, soil dynamics, hydrodynamics, and control. The Matlab/Simulink interface is part of the Ph.D. study presented in this thesis. Other research projects are looking at interfacing HAWC2 with CFD codes, and previous work has interfaced HAWC2 with codes for simulation of floating structures [4, 22].

A thorough research of the possibilities to interface with Matlab was undertaken in order to find a suitable option. Different options for interfacing with Matlab are described in Section 2.3.1, with reference to some of their applications.



(b) Iterative simulator coupling with predictor scheme

Figure 2.3 continued: Illustrations of simulator coupling schemes**Figure 2.4:** Available external interfaces to HAWC2

2.3.1 Options for interfacing with Matlab

There are several possibilities to interface a given application with Matlab and Simulink. This section explores some of the concepts and methods commonly used to interface with Matlab/Simulink. Normally making available to Matlab a given program, or function written in a different language is done with the objective of taking advantage of the given application for use in Matlab programs. In some cases, saving computation time can be the driver for accessing shared libraries. Also the matrix manipulation, visualization and control tools in Matlab are attractive to other applications.

For example, the interfacing of GAMS (optimization software) and Matlab as described in [58], is done in order to combine the GAMS ability for large

nonlinear optimization with the Matlab visualization tools. This is achieved by having a *gams mex interface*, which basically comes down to a shared library compiled as Matlab executable (MEX-file) that is available from the Matlab command line as any other built-in function.

Another example is how PSCAD/EMT (electromagnetic transients simulation program) and Matlab are coupled [55]. This interface takes advantage of inter-process communication capabilities in both software using: 1) a Fortran subroutine (for PSCAD/EMT) and, 2) the *Matlab engine* (for Matlab). The Fortran subroutine starts a Matlab engine, and initiates the communication process, making Matlab functions and control system blocks (written in a Matlab m-file) available to PSCAD. This interface also allows the Matlab engine to run on a different computer on the same network, thereby allowing *parallelism* of the computation time. Another power system software that allows interfacing with Matlab is PowerFactory. Mainly, with the objective of taking advantage of the control design capabilities in Simulink [54]. It launches a Matlab engine that can execute a Simulink model restarting it every time PowerFactory gives a time-step. This frame keeps Matlab as a *slave* of PowerFactory [16].

Another way of interfacing with Matlab is the so-called *parallelization* of Matlab. In the sense that some of the tools used in order to run various Matlab engines (slaves) in a cluster called by another Matlab engine (master), can be attractive to interface Matlab with other applications. There has been more than a few initiatives to develop a parallel Matlab [59]. Nowadays, Matlab provides a Distributed Computing Server interface that supports a variety of platforms and operating systems. Also other platforms can be integrated using other generic application programming interfaces (APIs) [60].

2.3.1.1 Shared libraries

The concept of *shared libraries* can be ambiguous to some extent. In this document a shared library is considered a collection of functions that can be dynamically loaded by Matlab at run time [61]. The objective of shared libraries is that various programs can access a given set (i.e. library) of functions, subroutines, classes, etc., coded in another language (C, C++, Fortran, Delphi). It can be said that a shared library consists of a header file and the library itself (a *.dll file in Windows OS). The header file provides the *signatures* (or *prototypes*) of the functions, in other words the declaration of the function's name, type and number of arguments. Whereas the library file provides the actual definitions of the functions.

In order to give Matlab access to an external function in a shared library

the user needs to:

- load the shared library, and
- call the desired function.

This simple process involves knowing the full path of the library and the header file. It is then necessary to know the signature of the shared library functions (SL functions) and the type of arguments to be passed to it. Some argument types in Matlab are, in practical terms, the same as the corresponding type in the language the library is programmed. However, if the types are different they can be automatically or manually converted using Matlab functions as described in [61].

2.3.1.2 mex-files

Similarly, MEX-files are functions originally written in another programming language (i.e. source MEX-files in C or Fortran) and compiled to be Matlab *executable files* (namely, *.mexw32 files in Windows OS). Once these binary files are loaded, they work like Matlab built-in functions. These definitions are further explained in [61]. The structure of a source MEX-file is basically:

- comments,
- headers,
- computational routine and
- gateway routine.

A standard gateway routine, named `mexFunction`, is available. This is the actual interface to Matlab. Within `mexFunction` there is a section of declaration of variables, then the inputs and outputs are assigned to the corresponding variables. Finally the computational routine is called, again with arguments corresponding to the input and output variables requested from Matlab. A MEX-file can actually contain a set of functions, therefore it is similar to a shared library, with the difference that the MEX-file functions can be called like native Matlab functions.

2.3.1.3 S-functions

A system-function (S-function) is a Simulink block written in computer language (i.e. Matlab, C, C++, Fortran) [62]. Basically, it can be implemented as:

- a Level-1 or Level-2 M-file S-function (written in Matlab) or
- as a C MEX S-function (hand written in practically any modern language, via the S-Function Builder or via the Legacy Tool Code).

2.3.1.4 TCP/IP communication

The Transmission Control Protocol/Internet Protocol is a mechanism for transferring data between applications over multiple networks [63]. The origins of this protocol lie in the predecessor of the Internet and it is the under laying working architecture of the Internet as it is known today. Some of the features of TCP/IP are:

- quick and simple to configure,
- one end is the client and the other server, but once the link has been establish both can send and receive data,
- non-transactional, not persistent (i.e. it uses memory buffer),
- no built in security, and
- no standard way of signaling end and start of message.

It is possible to make applications talk to Matlab using TCP/IP. Such feature is included in the Instrument Control Toolbox and it is oriented to communicating with instruments that support this protocol [64]. It has been used to communicate with remote applications as described in [65].

2.3.1.5 Matlab engine

This feature allows external applications to call Matlab software and to run it in the background as a separate process. In Windows OS it uses a Component Object Model (COM) interface [61], which enables interprocess communication between applications. The engine library has routines available that allow the external application to control Matlab computation engine (i.e. to make it a *slave*). These functions basically come down to start up/shut down and send/receive data.

2.3.2 HAWC2-Matlab coupling

The solution developed is based on keeping HAWC2 as a stand-alone application while letting Matlab *manage* some HAWC2 processes and have

dynamic access to data and input variables every time-step. Thereby, the interfaces described with the illustrations in Figure 2.5 using dynamic libraries, and TCP/IP sockets was implemented and tested. On this interface HAWC2 and Matlab run as separate processes –on the same, or on different computers, Matlab acts as a client and HAWC2 as a server using local TCP/IP sockets (i.e. local IP addresses and port numbers). Once the connection is established both ends can send and receive data. HAWC2 is set to remaining *listening* for the client to send inputs and requests.

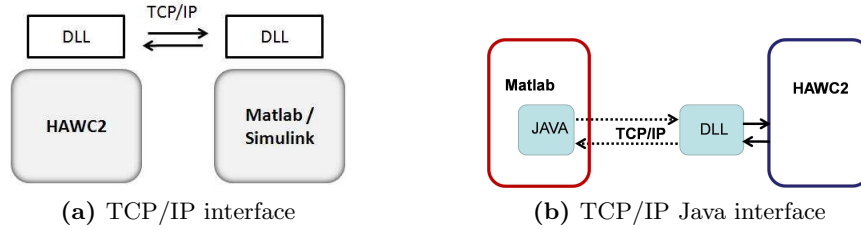


Figure 2.5: HAWC2 - Matlab interfacing using shared libraries and TCP/IP sockets

The version in Figure 2.5a was tested with a fixed-speed wind turbine model [66] on one computer. It consist of two dlls call by the applications, and connecting to each other by TCP/IP. The same concept is used in the latter version, described in Figure 2.5b. However in this case it uses built-in java capabilities in Matlab. Namely, a built-in routine [67], that sets up a Java object with a local TCP/IP socket (i.e. client), is run from Matlab while HAWC2 calls a DLL that listens to this socket every time-step (i.e. server). In this way the HAWC2 simulation runs as an independent process, sending and receiving data through the TCP/IP socket. Therefore, this interface of HAWC2, and Matlab can be run in different computers, allowing some degree of parallelization. This interface is successfully tested a cluster, opening the possibility to parallel computing.

A flowchart of the simulation process with HAWC2-Matlab integrated dynamic analysis environment is illustrated in Figure 2.6. The simulation process takes the following steps

1. Previous to the flow depicted in figure 2.6
 - (a) Time-data management variables, generator model, and controls are initialized in Matlab
 - (b) The shared library developed to interface with HAWC2 is loaded, functions of this library are used to startup HAWC2
 - (c) At startup, HAWC2 uses specified input files and sets a local TCP/IP socket listening to Matlab

- (d) Matlab then asks HAWC2 to step to a given *initialization* time and wait
2. Once the systems in both applications are initialized, the simulation continues with Matlab reading information of the relevant states (i.e. shaft speed ω) and variables (i.e. wind speed v , blade angle θ) from HAWC2
3. Matlab solver solves its systems (i.e. generator model, and control), and outputs forces and constraints
4. Forces (i.e. torque T), and constraints (i.e. control variable: blade angle θ) are sent back to HAWC2 along with the indication of taking a time-step
5. HAWC2 solves its system, sends states and variables back, and waits again for Matlab
6. The process is then repeated until the end of the simulation, as long as each solver converges

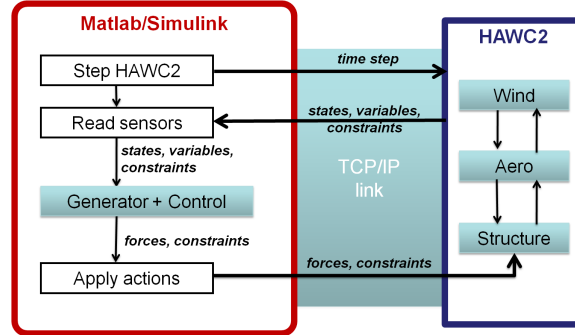


Figure 2.6: Flowchart of integrated dynamic analysis environment

2.3.2.1 Implementation hurdles

Some remarks regarding the implementation, that maybe useful for other users of Matlab/Simulink-HAWC2 are

- *Sign conventions.* In this thesis the generator model is in motor convention, therefore torque, and power are negative for generator mode. HAWC2 takes the input of external torque as positive relative to the coordinates of the body to which it is applied (see command `body moment_int` in [45]).

- *Solving systems with different time steps.* In the case that the system in Matlab is solved at a different time-step (or at a variable time-step) than the system in HAWC2 one should take measures to avoid numerical noise, or divergence of the time kept by Matlab compared to time kept by HAWC2.
- *Matlab memory.* It can be an issue to save a large amount of data from a Simulink model to the workspace. Saving data as an array, instead of an structure will save space and time. However, some variables may be sampled at different rates and will therefore need to be saved as an structure with time.
- *Enabled subsystems.* The Simulink block containing the link to the m-file that executes the TCP/IP link to HAWC2 cannot be used as an enabled subsystem. Therefore, during the initialization phase of the simulation use the m-file itself, if it is necessary to keep some initial values of the interfaced variables.
- *Test models.* Using a simple model of a wind turbine in Simulink to test, and tune a given controller before using it in the integrated analysis environment can be helpful. However, such simple model ought to include the most relevant dynamics.
- *Solver selection.* Time constants and/or order of transfer functions will influence the simulation time, particularly if the system becomes stiff and the Simulink solver is not chosen accordingly.
- *Interfaced signals verification.* Use the sensors of HAWC2 corresponding to the sent by Matlab to test that signs and units are as expected.
- *Algebraic loops.* Dealing with complex systems of differential algebraic equations (DAE) will most likely yield algebraic loops, Simulink's solver handles them quite well but sometimes it may need your help, using first order filters with very small time constants is suggested in the manual, the user may also consider including more states of the system. For example, one may use a full order generator model instead of a reduced order one, if some of the signals that are used as inputs to the generator model depend algebraically on some of the generator outputs.
- *Solver coupling with different time-step.* When using a variable-step solver in Simulink the signals from Matlab should be passed by a first order filter with a time constant equal to the time-step of the HAWC2 simulation.

- *Discrete time blocks.* In general, including blocks with large discrete sampling rates will increase the simulation time. Particularly, when those blocks store data between sampling times.
- *Low pass filters.* Naturally, very low cut-off frequencies in low pass filters will increase the simulation time considerably.

2.4 Summary

A new simulation environment for integrated dynamic analysis is presented in the context of a conceptual integrated design approach. The simulation environment features the aeroelastic code HAWC2, and the high level programming language Matlab with its graphical environment Simulink. The state-of-the-art capabilities for aeroelastic analysis of HAWC2, and its proven capability of interfacing with other codes for floating structures and hydrodynamic loading, together with the flexibility of Matlab/Simulink, makes this integrated simulation environment very powerful for research purposes.

A modular approach is taken in the formulation of models for this integrated simulation environment, because this is the most flexible approach, and builds on formulations already implemented in modern engineering practice. Nevertheless, the structural formulation in HAWC2 is based on multi-body dynamics, which is naturally suited for modular formulation, and for inclusion of external systems as forces or by means of constraints.

A benchmark of software for aeroelastic analysis, for dynamic analysis, and for power systems analysis, yields a tendency towards development of more advanced wind turbine models for various purposes. Such models may be directly developed in a specific code or software package; or they may be based on interfacing with other codes. Furthermore, commercial general purpose commercial software packages are entering the wind turbine design market.

The simulation environment developed in this Ph.D. study couples the solvers in Matlab and HAWC2 in a non iterative scheme. Taking advantage of the diversity of solvers available in Matlab, it is possible to solve the systems in Matlab with variable step, by using a linear estimator between synchronization time-steps. Synchronization time-steps in the range of 0.01-0.001 s are used.

The software interface to couple simulation tools keeps both applications as stand alone. The interface utilizes TCP/IP communications between HAWC2 and Matlab, the latter version makes use of built-in java capabilities in Matlab, and opens the possibility to parallel computing.

General description of models

This chapter introduces the models developed in the context of this work, some of which are used for the study cases in Chapters 4 and 5.

Section 3.2 describes the submodels that compose two types of wind turbine models, and Section 3.3 describes two power system models used for (1) voltage faults, and (2) frequency control.

3.1 Overview

During this Ph.D. study models for integrated dynamic analysis of fixed-speed active-stall (FSWT), and variable-speed wind turbines (VSWT) have been developed. They are implemented in the integrated dynamic analysis environment, described in Section 2.3.2. In Chapter 4, application examples of the integrated dynamic analysis environment using FSWT and VSWT models, are presented.

The block diagram in Figure 3.1, illustrates the submodels described in this chapter. Wind and aeroelastic model are simulated in HAWC2, while generator system, blade angle control, and power system are simulated in Matlab/Simulink.

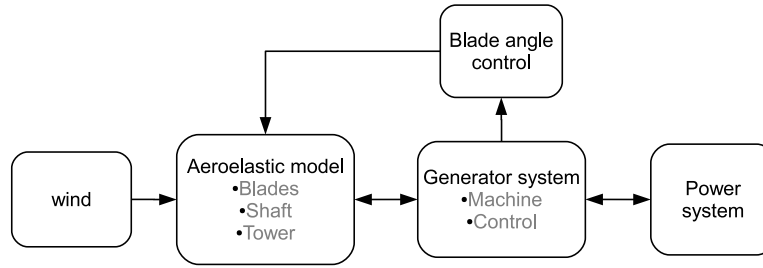


Figure 3.1: Block diagram of models for integrated analysis of wind turbines

3.2 Wind turbine model

Integrated wind turbine models described here are beyond the standard models used for load certification. Furthermore, using HAWC2 it is possible to also couple foundation structures to the aeroelastic model. Foundations can be fixed to a marine soil, under waves and marine currents loading. On the electrical side, including detail models of electrical components, advanced controls at wind turbine, and at wind farm level is at hand with the Matlab/Simulink integrated analysis environment. Figure 3.2 is an illustration of wind turbine subsystems.

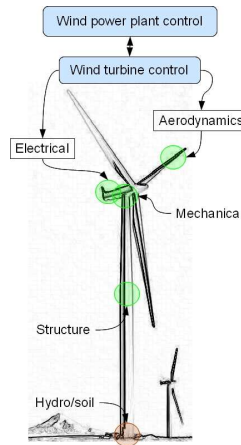


Figure 3.2: Illustration of wind turbine subsystems.

There are many submodels that build up a wind turbine model for integrated dynamic analysis, ultimately depending on the focus of the study. It can be interesting to discuss how to categorize or to group such submodels, specially if it brings implications to the variables they exchange. Even more so, if those variables are exchanged across different software within an integrated simulation environment, this discussion is partly taken in Chapter 2. In this section the objective is to describe the following submodels of a wind turbine

model

- Aeroelastic described in Section 3.2.1
- Drive train described in Section 3.2.2
- Generator system (electrical generator and its control), described in Section 3.2.3
- Blade angle control described in Section 3.2.4

Such grouping is only *semantic*, and it is adopted here to describe the models because it is simple and it gives an overview of the components involved.

3.2.1 Aeroelastic model

This section describes the aeroelastic model implemented in HAWC2 –from a user perspective, since a rigorous description is outside the scope of this work. The acronym HAWC stands for Horizontal Axis Wind turbine Code, this is the name of the first generation of the code started in 1986, that had a finite element method formulation (FEM). The second generation code –HAWC2– has a multibody dynamics formulation in a floating reference frame, allowing large rotations and deflections to be properly considered [22, 68].

In HAWC2, The structural subsystems are composed of bodies, each of which is in turn composed of a number of Timoshenko three-dimensional beams with their own coordinate system (elements with 6 degrees-of-freedom). Each body has a set of algebraic equations –constraints– that relate its movements, and forces to those of other bodies. Constraints are solved together with the equations of motion (second order, non-linear differential equations) [22, 68].

The following features are available in HAWC2

Wind conditions. Mean wind speed, wind steps, ramps, gusts, different options for shears, turbulence is generated or loaded from outside (cartesian coordinates –Mann, or polar coordinates –Veers).

Aerodynamics. Unsteady blade element momentum –dynamic inflow, dynamic stall, skew inflow, shear effects on the induction, and effects from large deflections.

Dynamic stall. Two models are available: 1) Øye model –stall separation lag, 2) modified Beddoes-Leishmann model –effects of shed vorticity from the trailing edge.

Tower shadow. The fact that wind conditions change locally near the tower can be simulated by potential flow (normally used for up wind turbines) or jet-model (better for downwind turbines).

External forces. In general external forces are placed on the structure in the deformed state, which is especially important for pitch loads, and twist of the blades.

Large rotations. The multibody formulation of the structure makes it possible to represent more accurately large deflections, by representing a given structural part (i.e. body) by many elements.

3.2.1.1 HAWC2 structure and modules

The structure of a HAWC2 model can be summarized describing the contents of a main input file.

Main input file. It is formed of commands and command options, the commands are gathered in their corresponding command/sub command block to keep a logical structure. The order of the command blocks is not important, but it is typical to keep the order as follows:

- **simulation** (commands use to set parameters of the simulation: time duration, time step, solver parameters)
- **new_htc_structure** (bodies, their orientations, and constraints are created with commands corresponding to this command block)
- **dll** (commands corresponding to external interfaces)
- **wind** (wind conditions such as mean wind speed, density, shear and turbulence format, tower shadow method, turbulence intensity)
- **aero** (set the number of blades for the aerodynamics to link structural bodies to aerodynamic blades, layout data and profile coefficients data, induction method, tip loss, dynamic stall)
- **output** (file name and data format of output files, select output signal from sensors, constraints, and dll inputs)

Note, that within the command blocks in some cases it is necessary to have a specific command as the first line [45]. In terms of data files a HAWC2 model requires:

1. Structural input file, which it is loaded within the command block

`new_htc_structure,`

one file can contain the data from many different bodies, each body is created with a set of structural data. A *toy* example is shown in Appendix D.

2. Aeroelastic data files, which constrain layout, and aerodynamic profile coefficients of sections of wind turbine blades. These files are loaded within the command block `aero`.
3. Turbulence files, which are loaded or created according to the commands in the command block `wind`.
4. Output file, which contain the outputs of a simulation as specified by subcommands in the command block `output`. The name of an output file is also specified in the command block `output`.

The structural model in HAWC2 is illustrated in Figure 3.3, where one of the blades, and the tower are represented with their main bodies, constraints, and forces external to HAWC2 model (i.e. generator torque). The standard drive train, described in Section 3.2.2.1, is also illustrated. Namely, by the main body (shaft) that defines it, and the constraints and external forces that link it to other bodies and to the generator system.

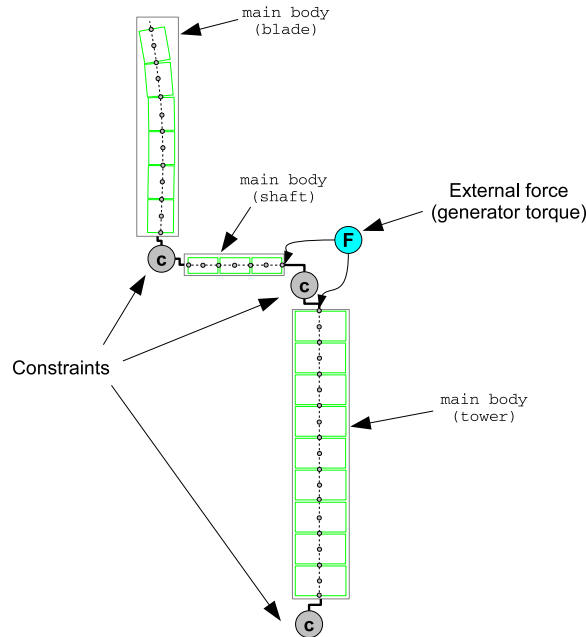


Figure 3.3: Structural and standard drive train model implemented in HAWC2

3.2.2 Drive train model

A wind turbine drive train consists of many components placed on a main frame, inside a nacelle. The main frame bears a yaw system, and is placed on the tower top. The components of the drive train inside the nacelle are shafts, shaft couplings, bearings, torque limiters, gears, brake. In case of a geared drive train, a very complex component is the gearbox. A detailed analysis of the drive train components dynamics, their interaction with the main frame, and the dynamics inside the gearbox, is beyond the scope of this study. The following sections describe standard drive train models, and a simplified gearbox model. The standard drive train models consider the gearbox ideal, or as a system with torsional stiffness. The simplified gearbox model represents to some extent the dynamics of gearbox, and the way torque is transferred from rotor, through gearbox into the tower top.

3.2.2.1 Standard drive train models

Ideal gearbox This model consists of the low speed shaft and the generator rotor inertia. The low speed shaft is a single rotating beam, that in one end is

1. Constrained to rotate relative to tower top
2. Attached to the generator rotor inertia, either as a concentrated mass or as an element with the corresponding inertia

The inertia of generator is referred to the low speed side by scaling it by the square of the gearbox speed ratio. The other end of the shaft is attached rigidly to the aerodynamic rotor. The transfer of loading from aerodynamic rotor, through the shaft, into the tower is equal to the torque exerted by the generator magnetic field on the generator rotor mass. Bearings are considered rigid in radial and axial directions.

Gearbox with torsional stiffness Modeling a geared wind turbine drive train by representing the gearbox as a system with only torsional stiffness has been described in [69]. In such model, the gearbox is considered to be a single stage of parallel gears, where each gear has only one rotational degree of freedom co-axial to the axis of the shaft. The contact forces between gears are assumed linearly proportional to the deformation along the line of contact, and written in terms of torque and angular rotations. These simplifications yield a model of two masses connected by a stiffness constant. Such model has two eigen frequencies one at 0 Hz, and the second at around 3 kHz [69].

3.2.2.2 Detailed nacelle dynamics

This model was developed in the context of applied aeroelastic research as described in [70]. The main objective of this model was to study the transfer of loading from aerodynamic rotor to the tower. The single stage gearbox consists of a ring, a sun, a planet carrier, and 3 planets. All of them with the same stiffness. In order to couple this simplified gearbox and main frame model to beam elements in HAWC2, a module that allows to solve other dynamic systems was developed as described in [70]. The inconvenience of using this model for aeroelastic simulations is that a very small time step is required.

3.2.3 Generator system

In aeroelastic simulations it is common to model the generator system as a first-order system. However, in [71] an asynchronous generator dynamic model was developed for HAWC2, and [72] developed a reduced model of a doubly-fed asynchronous generator (DFAG), consisting of the active power controller, disregarding the dynamics of the generator. In this study dynamic models of asynchronous generator, and DFAG are developed and coupled to aeroelastic models.

This section describes first-order, asynchronous, and doubly-fed asynchronous (DFAG) generator models. Their couplings to other systems and controls are described.

3.2.3.1 First-order generator model

The standard generator model provided with HAWC2 [73] is a *slip generator* model, it is based on a linear approximation of the torque versus generator rotor speed characteristic, and it assumes that the generator dynamics can be approximated as a first-order system. For this study, this slip generator model is implemented as a look-up table of generator torque-rotor speed characteristic in steady-state, and a first-order filter as illustrated in Figure 3.4.

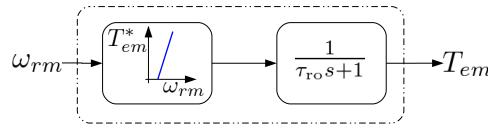


Figure 3.4: Block diagram of first-order generator model.

3.2.3.2 Asynchronous generator model

A detailed derivation of the classical asynchronous generator dynamic model is presented in Appendix A, namely

- A basic introduction in Section A.1
- Steady-state circuit model, and torque characteristics of asynchronous generator and DFAG in Section A.2
- Derivation of dynamic model in dq -frame in Section A.3
 - Full order model: Section A.3.3
 - Reduced order model: Section A.3.3.1
 - Comparison of dynamic and steady state models: Section A.3.3.2

The full-order dynamic model of asynchronous generator is implemented with flux linkages λ as state variables, the detailed derivation in Section A.3.3 is done including the zero component of dq -transformation (i.e. Eq. A.42-A.44). Let us here

1. Disregard the zero component of the dq -transformation
2. Define the arbitrary reference frame oriented and rotating with the stator flux space vector

The model is then, in matrix form expressed by Eq. 3.1. The system matrix \mathcal{M} is composed of generator parameters ($R_s, R_r, \mathcal{L}_s, \mathcal{L}_r, \mathcal{L}_m$), and speed of stator (ω_{se}) and rotor ($\omega_{se} - \omega_{re}$) dq -frame. The rotor voltage \mathbf{v}_{dqr} is zero.

$$\begin{aligned}
 \begin{bmatrix} \dot{\lambda}_{dqs} \\ \dot{\lambda}_{dqr} \end{bmatrix} &= \mathcal{M} \begin{bmatrix} \lambda_{dqs} \\ \lambda_{dqr} \end{bmatrix} + \begin{bmatrix} \mathbf{v}_{dqs} \\ \mathbf{v}_{dqr} \end{bmatrix} \quad (3.1) \\
 \mathcal{M} &= \begin{bmatrix} \frac{R_s \mathcal{L}_r}{\mathcal{D}} & -\omega_{se} & \frac{-R_s \mathcal{L}_m}{\mathcal{D}} & 0 \\ \omega_{se} & \frac{R_s \mathcal{L}_r}{\mathcal{D}} & 0 & \frac{-R_s \mathcal{L}_m}{\mathcal{D}} \\ \frac{-R_r \mathcal{L}_m}{\mathcal{D}} & 0 & \frac{R_r \mathcal{L}_s}{\mathcal{D}} & \omega_{re} - \omega_{se} \\ 0 & \frac{-R_r \mathcal{L}_m}{\mathcal{D}} & \omega_{se} - \omega_{re} & \frac{R_r \mathcal{L}_s}{\mathcal{D}} \end{bmatrix} \quad \text{with} \\
 \mathcal{D} &= \mathcal{L}_m^2 - \mathcal{L}_s \mathcal{L}_r; \\
 \begin{bmatrix} \lambda_{dqs} \\ \lambda_{dqr} \end{bmatrix} &= [\lambda_{ds} \quad \lambda_{qs} \quad \lambda_{dr} \quad \lambda_{qr}]^T; \quad \text{and} \\
 \begin{bmatrix} \mathbf{v}_{dqs} \\ \mathbf{v}_{dqr} \end{bmatrix} &= [v_{ds} \quad v_{qs} \quad v_{dr} \quad v_{qr}]^T
 \end{aligned}$$

Given the solution of the fluxes linkages λ_{dq} , currents \mathbf{i}_{dq} and electromagnetic torque T_{em} can be calculated as indicated by Eq. 3.2, and Eq. 3.3.

$$\mathbf{i}_{dq} = \mathbf{L}_{dq}^{-1} \lambda_{dq} \quad (3.2)$$

$$\mathbf{L}_{dq}^{-1} = \frac{1}{\mathcal{L}_s \mathcal{L}_r - \mathcal{L}_m^2} \begin{bmatrix} \mathcal{L}_r & 0 & -\mathcal{L}_m & 0 \\ 0 & \mathcal{L}_r & 0 & -\mathcal{L}_m \\ -\mathcal{L}_m & 0 & \mathcal{L}_s & 0 \\ 0 & -\mathcal{L}_m & 0 & \mathcal{L}_s \end{bmatrix}$$

$$T_{em} = \frac{3}{2} \frac{p_f}{2} \frac{\mathcal{L}_m}{\mathcal{D}} (\lambda_{qs} \lambda'_{dr} - \lambda_{ds} \lambda'_{qr}) \quad (3.3)$$

Figure 3.5 illustrates the variables that couple the asynchronous generator model to other systems, namely stator and rotor terminal voltage, speed of stator frame, and speed of rotor frame. The speed of the stator frame is the frequency of the stator voltages. This asynchronous generator model is used for the fixed-speed wind turbine model in Section 4.1.

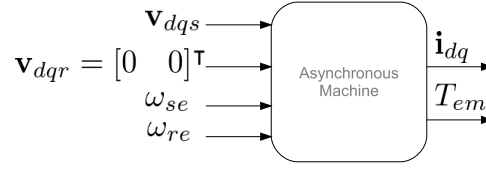


Figure 3.5: Block diagram of Asynchronous generator model.

3.2.3.3 Doubly-fed asynchronous generator model

The doubly-fed asynchronous generator (DFAG) consists of an asynchronous generator, rotor-side converter (RSC), dc-link, grid-side converter (GSC), and smoothing inductor. RSC and GSC are considered control-lable voltage sources, therefore the switchings of the converters are neglected, and phase-locked loops (PLL) controls are considered ideal. Figure 3.6 illustrates the components of DFAG, the control of RSC and GSC is described in Section 3.2.3.4. The dynamics of the dc-link neglecting power losses [74, 75] are represented according to Eq. 3.4. The active power P_{gsc} , flowing through the smoothing inductor X_{sl} , is calculated according to Eq. 3.5 based on the concept of power transferred between two sources [76].

$$V_{dc} = \sqrt{\frac{2}{C_{dc}} \int (P_r - P_{gsc}) dt} \quad (3.4)$$

$$P_{gsc} = \frac{3}{2} \frac{|\mathbf{v}_{gsc}| |\mathbf{v}_{dqs}|}{X_{sl}} \sin \delta \quad (3.5)$$

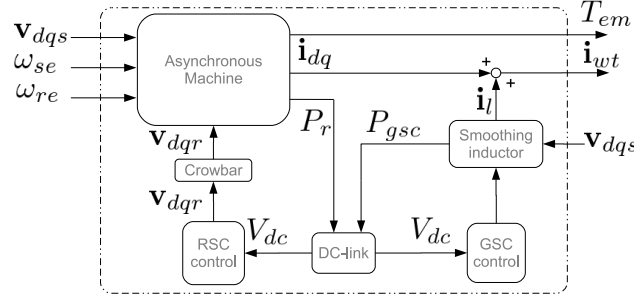


Figure 3.6: Block diagram of Doubly-fed Asynchronous generator model.

A crowbar is used to protect the RSC from over currents [75]. It consists of a switch that short-circuits the rotor through an external resistance, thereby isolating the RSC. It has a duty cycle of 0.5 s, it activates when $|\mathbf{i}_r| \geq 2$ p.u., and it deactivates if $|\mathbf{v}_s| \approx 1$ p.u., and if the duty cycle is met. For the reconnection of the RSC once the crowbar is deactivated, the RSC control is reset to avoid larger transients [74].

3.2.3.4 Generator control

The control of RSC, and GSC is implemented as generic cascade proportional-integral (PI) controls [52, 74, 77]. Figure 3.7 shows these control loops. RSC control in Figure 3.7a, controls total active power P_t , and stator reactive power Q_s . GSC control in Figure 3.7b, controls the dc-link voltage V_{dc} , and operate the converter at unity power factor (i.e. $i_{dl}^{ref} = 0$). The doubly-fed

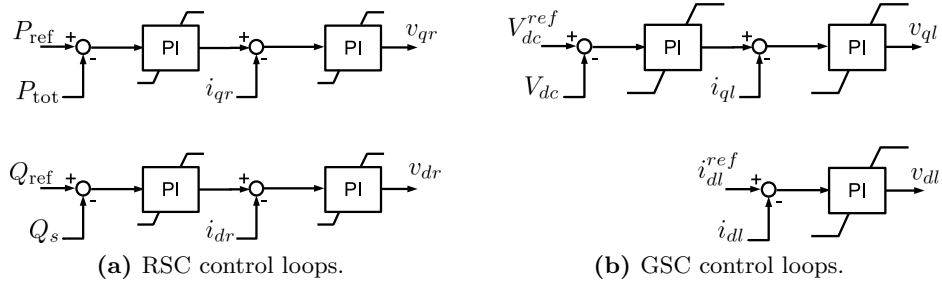


Figure 3.7: Doubly-fed asynchronous generator control.

asynchronous generator (DFAG) is used for the variable-speed wind turbine in Section 4.2 and Chapter 5.

3.2.3.5 Inertial response control

Inertial response can be provided by wind turbines to support a power system on conditions of sudden loss of generation. However, in the case of variable-speed wind turbines (VSWTs), auxiliary control loops are needed in order to provide an inertial response. This section describes control concepts for inertial response of wind turbines.

VSWTs need specific inertial response controls because the voltage at the terminals of the generator is decoupled from the power system voltage. Therefore, the electromagnetic torque will not be directly influenced by changes on the frequency of power system voltage ω_s . This means that without specific control actions the speed of the wind turbine rotor will not vary according to changes of ω_s (i.e. the wind turbine will not show an *inertial response*).

Demonstration of control concepts that tap kinetic energy of a wind turbine rotor to *emulate* an inertial response, has been done in [78–87]. All of them based on the fundamental relationship between rotational speed, and kinetic energy. For example, the work in [78] derived an *inertial response* control law to tap kinetic energy from the wind turbine rotor, as indicated in Eq. 3.6

$$T_{ir}^* = 2H_{wt}\dot{\omega}_s \quad (3.6)$$

where H_{wt} is the so-called *inertia constant* [76], and $\dot{\omega}_s$ is the time derivative of frequency of power system voltage. Observe that in Eq. 3.6 a negative slope of $\omega_s(t)$ yields a negative torque T_{ir}^* .

The inertia constant of wind turbines is, in this study defined by Eq. 3.7, where J_{wt} is the lumped moment of inertia of the wind turbine rotor J_{rot} plus the moment of inertia of the generator rotor J_{gen} . In drive trains with gearbox, J_{rot} is referred to the high-speed side (i.e. to the mechanical speed of the generator rotor). ω_{sm} is the *mechanical* synchronous frequency, and S_{base} is the apparent power base of the generator.

$$H_{wt} = \frac{J_{wt}\omega_{sm}^2}{2S_{base}} \quad (3.7)$$

The implementation of the control law for inertial response (Eq. 3.6) in [78, 80], includes a first order filter of $\dot{\omega}_s$ that is said to limit rate of change, and the maximum peak of torque. Such implementation is illustrated in Figure 3.8, where the torque set point T_{ir}^* , calculated with the inertial response control law, is subtracted to a torque set point T_{ref} , calculated from the torque-speed operation curve of the wind turbine. T_{ref} is then converted to a current set point i_{qr}^* , that is the input to the current control loop. In [79], the same approach is taken but instead of a filter, a compensation element $k/(s^2 + 2\xi\omega_n s + \omega_n^2)$ is used.

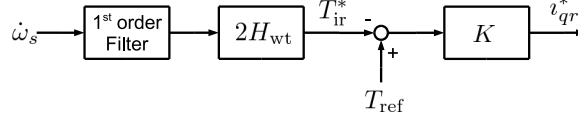


Figure 3.8: Inertia response control -based on torque set point.

Furthermore, in [80] the inertial response control in Figure 3.8 is compared to a control proportional to the deviation of the frequency to its nominal value –*droop control*– given by Eq. 3.8.

$$T_{dr}^* = k_{dr}(\omega_0 - \omega_s) \quad (3.8)$$

Similarly, [83, 84] utilize a power set point P_{ir} to tapping the kinetic energy of the wind turbine rotor. This control law is illustrated in Figure 3.9, where $\Delta\omega_s$ is a *delta* variable that represents $\dot{\omega}_s$. The limits to the inertial response power set point P_{ir} are P_{ir}^{\min} , P_{ir}^{\max} . The limits to the rate of change of P_{ir} are $\frac{d}{dt}(P_{ir})^{\min}$, and $\frac{d}{dt}(P_{ir})^{\max}$. P_{ref}^* is the optimal power set point, and P_{ref} the set point to the generator power control loop.

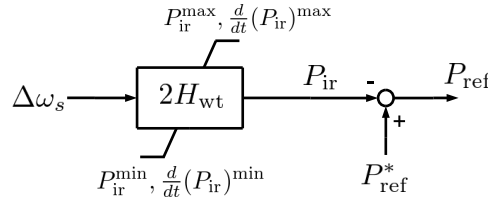


Figure 3.9: Inertia response control -based on power set point.

3.2.3.6 Damping controllers

Providing a smooth performance of the plant is one of the basic objectives of a control algorithm. Therefore, a controller may be intrinsically designed to damp specific oscillations, or it may include a dedicated loop that functions as a damper. For example, the work in [50, 52, 53] demonstrated damping of drive train oscillations during a voltage fault by controlling the set point of the generator power control loop (P_{ref} in Figure 3.7a), with a PI control of generator rotor speed error as illustrated in Figure 3.10. The speed set point ω_{ref} was calculated from a look up table of optimal speed ω_{op} versus wind speed W_y . In this Ph.D. study this concept is applied to implement (1) proportional damping control for balanced fault cases –Section 5.2, and (2) for investigations of load reduction in cases of unbalanced faults –Section 5.3.

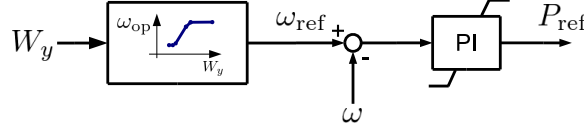


Figure 3.10: Damping control for balanced fault operation.

Proportional set point damper. This control is a simplified version of the damping control shown in Figure 3.10. The concept is to change the set point P_{ref} in the power control loop of the generator control, according to changes in generator speed ω . This control is shown in Figure 3.11, a second order filter on the measured generator speed takes out drive train oscillations, the filtered speed is used to look-up an optimal power table.

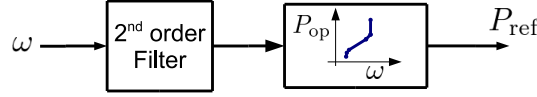


Figure 3.11: Proportional set point damper for balanced fault operation.

Basic damper. This basic damping control scheme is implemented as a first step to explore the load reduction potential during unbalanced faults, in terms of equivalent loads [88]. It builds on the concept of using a speed set point, instead of a power set point to calculate the set point of the current control loop [89]. Both q - and d - loops are shown in Figure 3.12.

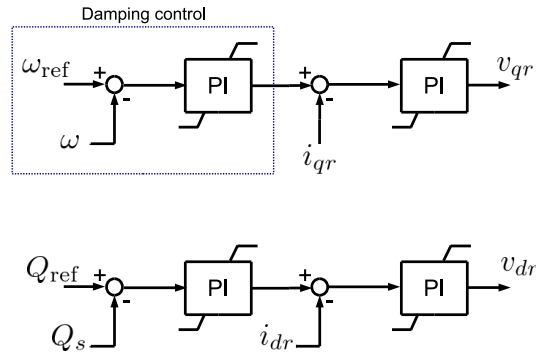


Figure 3.12: Damping control for unbalanced supply voltage operation.

Resonant damping control. Resonant damping control (RDC) techniques are used in many applications, formulations of resonant filters, and their location within the control structure can vary in different literature but the fundamental concept remains, to use a resonant filter that damps

oscillations of the plant at specific frequencies. Figure 3.13 illustrates the concept, in that case that the output Y of the plant has an unwanted frequency at ω_R , the resonant filter $\frac{K_R s}{s^2 + 2\zeta\omega_R s + \omega_R^2}$, will amplify that frequency without any lead or lag phase, therefore adding the output of the resonant filter B to the negative feedback of the plant output will damp oscillations at ω_R .

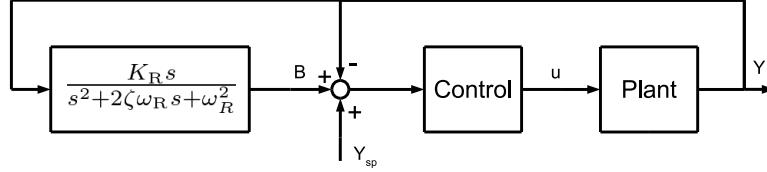


Figure 3.13: Illustration of a resonant filter used for resonant damping control (RDC).

RDCs developed in this study have the principal objective of reducing electromagnetic torque fluctuations due to an unbalanced fault, thereby minimizing wind turbine structural loads.

RD-Comp control. The resonant damping control plus phase compensation (RD-Comp control), takes the approach in [89]. Using a resonant filter, and a phase compensator, plus the basic damping control that uses the generator speed to calculate the set point to the current control loop. This control is illustrated in Figure 3.14, the resonant filters plus phase compensators H_q and H_d , consist of a second order resonant filter set to resonate at 100 Hz and a phase compensator to increase the gain margin. The reason for aiming to a 100 Hz frequency is described further in the following description of RDC developed.

RD-SW control. The resonant damping control with switching functions (RD-SW control) developed here consists of the normal operation control shown in Fig. 3.7, plus resonant filters for damping at specific frequencies, and switches to keep the set points for current control loops practically constant during and shortly after an unbalanced fault. The q -axis cascade loop of the RDC is shown in Fig. 3.15. The d -axis cascade loop (not shown) has the same structure as that in Fig. 3.15 with Q_{ref} , Q_s , i_{dr} , $F_d(s)$, $C_d(s)$, v_{dr} , v_d^{c*} , and Q_s^o instead of P_{ref} , P_{tot} , i_{qr} , $F_q(s)$, $C_q(s)$, v_{qr} , v_q^{c*} , and $P(\omega_m)$. The objective of resonant filters $C_q(s)$, $C_d(s)$ is to damp T_{em} , Q_s oscillations at 100 Hz during, and partly after an unbalanced fault; while $F_q(s)$, $F_d(s)$ damp oscillations at 50 Hz of i_{qr} , i_{dr} after the fault once the control of the outer loop is back to normal.

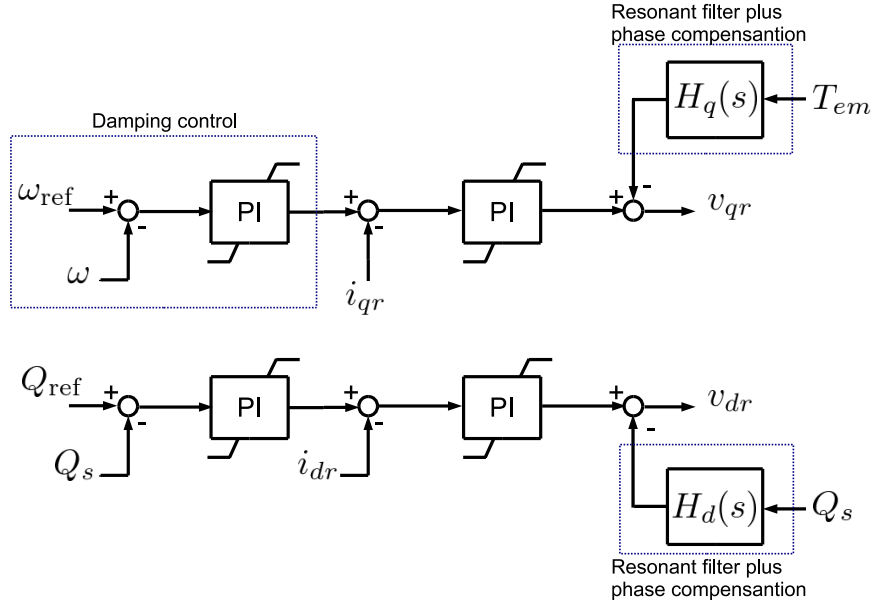


Figure 3.14: Damping control plus compensators resonant filters with phase compensation (RD-Comp control).

Switches are implemented as indicated in Fig. 3.15, both switches use the same signals to change state. One of them is used to switch the process variable (i.e. P_{tot} to $P(\omega_m)$) that is fed back to the outer control loop, in order to avoid that oscillations induced by the unbalanced fault are fed back into the outer loop and passed on to the set point for current control loop. This is because active, and reactive power will show 100 Hz oscillations that are generally hard to control or minimize without decomposition of positive, and negative sequences. Namely, in Fig. 3.15 the process variable is switched from P_{tot} to $P(\omega_m)$ when the voltage unbalance factor VUF is different than one. It is switched back to P_{tot} when $\text{VUF} = 1$, and when the sampled damping term v_q^{c*} is within the values $\pm V_{\text{lim}}^c$. P_{tot} is the total active power calculated from current and voltage measurements, while $P(\omega_m)$ is the total active power calculated from the design table of power vs. speed. Analogously, in the d -axis loop (not shown) the process variable is switched from Q_s to Q_s^o , where Q_s is the stator reactive power calculated from current and voltage measurements, and Q_s^o is the value of Q_s before the fault. Therefore, the set points for current control loops are kept nearly constant during an unbalanced fault and until the damping terms v_q^{c*}, v_d^{c*} are relatively small. Moreover, the other switch in Fig. 3.15 indicates that once the control is back to normal the input to $F_q(s)$ is switched to i_{qr} , thereby adding a term to the error of q -axis current control loop that effectively damps 50 Hz oscillations. The same is done in the d -axis current control loop with the input to $F_d(s)$ switched from 0 to i_{dr} .

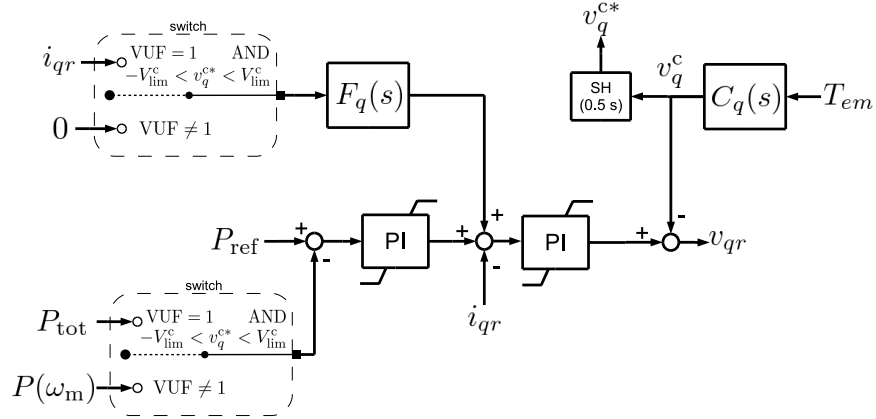


Figure 3.15: Resonant damping control with switching functions (RD-SW): q -axis loop (d -axis has the same structure with the variables corresponding to those of d -axis of normal operation control)

Again, the objective of the resonant filters is to damp electromagnetic torque, reactive power, and current fluctuations. The resonant filters $C_q(s)$, and $C_d(s)$ in Eq. 3.9 are aimed at damping electromagnetic torque T_{em} and reactive power Q_s oscillations respectively. The filters $F_q(s)$, and $F_d(s)$ in Eq. 3.10 are aimed at reducing current oscillations. The formulation of the damper $C_{da}(s)$ is that of a second order filter with a high quality factor Q as in [89]. However, in order to avoid introducing other phases to the system no further phase compensation is added in this case, the only implication is that the gain margin is reduced. The natural frequency of dampers ω_{da} is equal to twice the supply voltage frequency (i.e. 100 Hz). The resonant filter $F_R(s)$ in Eq. 3.10 is formulated as a second order system with low damping ratio ζ_R , and natural frequency ω_R equal to the supply voltage frequency (i.e. 50 Hz).

$$C_q(s) = H_1 \cdot C_{da}(s) \quad \text{and} \quad C_d(s) = H_2 \cdot C_{da}(s) \quad (3.9)$$

$$C_{da}(s) = \frac{s}{s^2 + \frac{\omega_{da}}{Q}s + \omega_{da}^2}$$

$$F_q(s) = K_{Rq} \cdot F_R(s) \quad \text{and} \quad F_d(s) = K_{Rd} \cdot F_R(s) \quad (3.10)$$

$$F_R(s) = \frac{s}{s^2 + 2\zeta_R\omega_R s + \omega_R^2}$$

3.2.4 Blade angle control

This section describes the blade control algorithms for fixed-speed active stall and variable-speed wind turbines.

3.2.4.1 Fixed-speed active stall wind turbine

The pitch control implemented is described in Figure 3.16, it consists of a moving average of the wind speed with a 60 seconds window, a sample hold of the moving average every 10 seconds, a look up table for the optimal pitch as a function of the wind speed, and a pitch servo that is modeled as a first order filter.

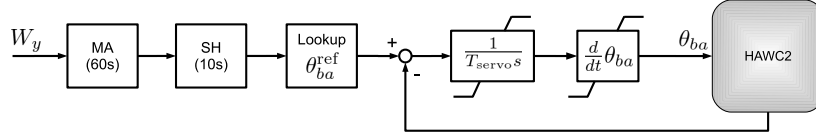


Figure 3.16: Blade angle control for fixed-speed wind turbine

3.2.4.2 Variable-speed wind turbine

For the variable-speed wind turbine model, the angles of the blades in HAWC2 model, are controlled by a deterministic adaptive control, implemented according to [51, 52]. A block diagram of such control with the objective of regulating speed is shown in Figure 3.17. It consists of a PI regulator with a scheduled gain. The schedule of the gain is designed to compensate nonlinear aerodynamic characteristics. The servo motors that rotate the blades are represented as a first order system with limits to minimum-maximum blade angle, and blade angle rate of change. Maximum blade angle rate is shown to be important to prevent over-speeding during a supply voltage fault [52]. Blade angle control with the objective of regulating

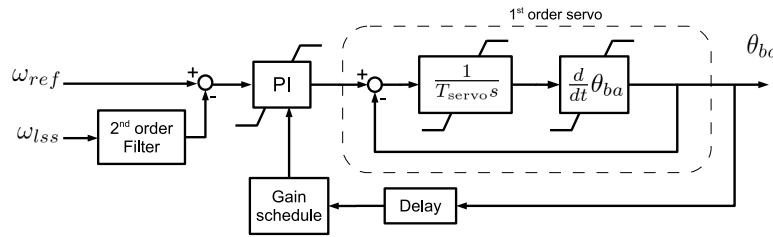


Figure 3.17: Blade angle control for variable-speed wind turbine.

power instead of speed was demonstrated in [79], with the purpose of achieving a faster rate of change of blade angle thereby improving the response of FSIG wind turbine to faults. In [51] a power limitation controller with the same structure as Figure 3.17 but regulating the error between a power reference, and the total active power measured, was used as part of an overall strategy to control DFAG wind turbines aimed at maximizing efficiency.

In the power limitation region, the power limitation controller changes the blade angle to keep rated power, while the generator controls loosely the speed letting it fluctuate a bit but avoiding over speeding. However, such control is not very fast, so fast changes of wind speed are reflected as rotor speed, and power variations. In this work, blade angle control to limit power is used in one case to study unbalanced voltage faults in Section 5.3.

3.3 Power system models

The objective of the power system models developed in the integrated analysis environment during this Ph.D. project is to study the impact of some power system conditions on wind turbine loads. The power system models are developed in Matlab/Simulink for interfacing with HAWC2. Even though Matlab/Simulink is not the ideal tool for simulation of large power systems in time-domain, under the conditions described in Section 3.3.2 it works well and has the advantage that adding controls is essentially straight forward. Precisely, the power system model for frequency control developed in Section 3.3.3 is native to Simulink environment given its formulation as transfer functions.

3.3.1 Background for power system model development

Modeling and simulation of power systems is a discipline itself. There are already many specialized tools available with a wide range of models depending on the specific purpose. Some of these tools used in wind power related applications are described in Tab. 2.1. A common drawback of power system simulation tools such as PSCAD, and PowerFactory is that complex control algorithms are considerably harder to design and develop than in Simulink. Thereby the interest on interfacing these tools with Matlab/Simulink. For example, [16] demonstrates an integrated analysis approach of a wind turbine model in Matlab/Simulink, and an equivalent grid model in PowerFactory. Part of the vision of integrated design of wind power systems is to take advantage of the capabilities and models available in different specialized software. However, it is not possible at this stage because the available interface between Matlab/Simulink and PowerFactory works in a master-slave frame [16], where a given Simulink model is run through a matlab engine (i.e. slave) that in turn runs the Simulink model restarting it every time PowerFactory (i.e. master) steps in time. Initial values of states, and relevant signal are send every time time step while global variables are set at the beginning of the simulation.

Moreover, there are many toolboxes for power systems analysis in Matlab.

The most relevant for the application sought in this study, and with significant user communities are considered to be PSAT, PLECS, and SimPowerSystems (described in Tab. 2.1). However, these toolboxes do not lend themselves to the main objective of this study. Mainly because the models in the blocks of these toolboxes are closed, and are not *normal* Simulink blocks so they need *measurements* blocks to interface. Therefore, it is not straight forward to integrate the models of those toolboxes in the integrated dynamic analysis environment.

3.3.2 Grid equivalent model

A simplified power system in the time-domain is modeled as a double circuit transmission line supplied by a voltage source \mathbf{v}_g . A line diagram of this grid equivalent model is shown in Figure 3.18, where a wind farm is connected on one side of the transmission line, and a voltage source on the other side of the line. The transmission line is modeled as a (lumped-parameter) symmetrical

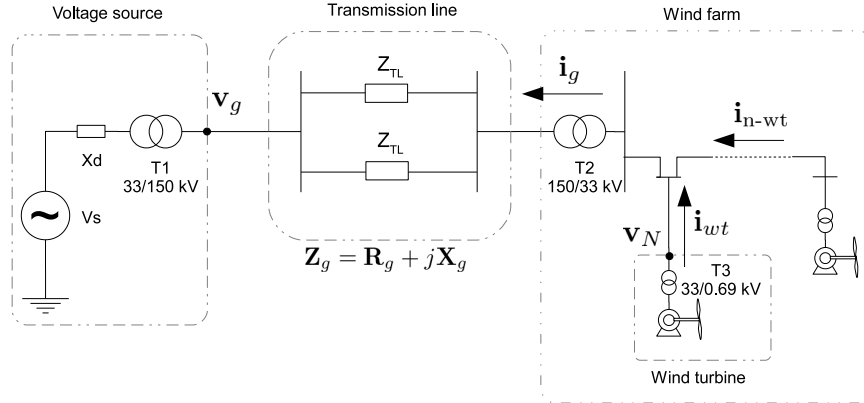


Figure 3.18: Line diagram of grid equivalent model.

RL-branch in dq-frame [90]. The corresponding voltage equations are those of a 3-phase RL stationary-circuit in an arbitrary reference frame. Namely, the same equations as those of the stator of an asynchronous machine, with a different reference frame in this case. The reference frame chosen is a synchronously rotating reference frame aligned to \mathbf{v}_g (i.e. system reference frame). Once the voltage source \mathbf{v}_g , transmission line equivalent impedance \mathbf{Z}_g , and wind farm current \mathbf{i}_g , are referred to the same voltage level, the voltage equations in matrix form are given by Eq. 3.11. When this model is connected to a wind turbine model, Eq. 3.11 is solved for the voltage at the stator terminal \mathbf{v}_N (in the system reference frame), where the wind farm current \mathbf{i}_g is an input.

$$\mathbf{v}_g - \mathbf{v}_N = \mathbf{R}_g \mathbf{i}_g + \omega_g \mathbf{L}_g \mathbf{i}_g + \mathbf{L}_g (\dot{\mathbf{i}}_g) \quad (3.11)$$

3.3.3 Model for frequency control

A model to study the dynamic response of wind turbines providing inertial response is developed in this Ph.D. project, it is based on the premise that active and reactive power flows are practically independent in transmission systems [76]. Under this consideration, active power balance influences the power system voltage frequency –that is the speed of synchronous generators in the power system, here it will be referred to as *system frequency*– and not the voltage. The model considers only the lumped response of generation and load, and *speed governing* control.

Generation and load. The response in frequency (i.e. $\Delta\omega_s$) of generation and loads in a power system, to changes in the power balance ΔP_{eq} can be represented as a first-order system [76]. The time constant of such equivalent system is a *lumped* inertia constant M_{gl} , that is the sum of the inertia constants of the generating units in the power system in question. The damping provided by the loads in the system is lumped in a damping constant D_{gl} . The transfer function of this representation of generation and load in a power system is given in Eq. 3.12.

$$H_{gl}(s) = \frac{1}{M_{gl}s + D_{gl}} \quad (3.12)$$

Speed governing. The control of the generation units is modeled as a typical speed governor and turbine. The *speed governor* consists of a PI control of speed, the set point is calculated with the linear relation of changes in load to speed deviation –*droop* of speed-to-load, or speed regulation characteristic– the output is a command to the turbine to increase or reduce production accordingly. Eq. 3.13 is the transfer function of the PI control of speed, where K_{p-g} is the proportional gain and K_{i-g} the integral gain.

$$H_g(s) = \frac{K_{pg}s + K_{ig}}{s} \quad (3.13)$$

The turbine is represented as a first order system with a time constant τ_t , has shown in Eq. 3.14.

$$H_t(s) = \frac{1}{\tau_t s + 1} \quad (3.14)$$

The implementation of the frequency control power system model is done in delta variables as shown in Figure 3.19, where $\Delta\omega_s$ is the deviation of the system frequency from the synchronous value. ΔP_{eq} is the active power balance between generation and load, ΔP_L changes in load, and ΔP_{wf} the changes in power from wind power plants.

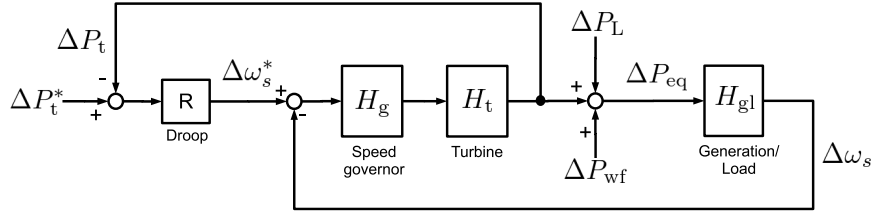


Figure 3.19: Power system model for frequency control.

3.4 Summary

This chapter presented models of wind turbines, and power systems to be used with the simulation environment described in Chapter 2 for integrated dynamic analysis. The wind turbine models are fixed-speed active stall, and variable-speed (DFAG) wind turbine. Aeroelastic and standard drive train models are implemented in HAWC2. Generator system, blade angle control, and power system models are implemented in Matlab/Simulink.

The aeroelastic models in HAWC2 comprehend wind field, aerodynamic and aeroelastic phenomena, and multibody formulation of the structure and standard drive train. Different drive train models were considered, however the standard drive train model with ideal gearbox is sufficient for studying structural loads at lower frequencies. For example the standard drive train model that includes gearbox torsional stiffness, only adds dynamics at very high frequencies.

Generator system model consists of electrical generator and control. The electrical generator modeled is an asynchronous generator, a reduced order model and a full order model were implemented. A detailed derivation of these models was done. The derivation of the full order model is straight forward, however the reduced order model involves some algebraic operations that were not very clear in the literature reviewed. Furthermore, it was considered important that the dynamic models output the right steady state value. Therefore, the models derived were compared to a steady state circuit equivalent model, finding good agreement.

For DFAG the generic cascade PI control, inertial response control, and damping controls were implemented. The inertial response control was implemented to suit the power system model for frequency control. The concept of resonant damping control (RDC) was introduced, and it is applied to develop controls to damp torque oscillations due to unbalanced supply voltage. The new RDC strategy is used in Chapter 5 to demonstrate reduction of structural loads.

Basic principles of power systems modeling and simulation were applied to

implement two power system models: a grid equivalent model of a transmission line, and model for frequency control.

These models can be used for integrated dynamic analysis for different objectives. For example to improve the design of wind turbine components, or to study the impact of power system conditions on wind turbine structural loads, as it is described in Chapters 4 and 5.

Application examples

In previous chapters the integrated dynamic analysis environment and its models were described. This chapter introduces two application examples, Section 4.1 presents an integrated dynamic analysis of a fixed-speed wind turbine, while Section 4.2 analyses the response of a variable-speed wind turbine providing frequency control support to a power system.

4.1 Dynamic analysis of fixed-speed wind turbine

In the following, a fixed-speed wind turbine is analyzed using the HAWC2-Matlab simulation environment described in Section 2.3. The wind turbine under analysis is a 2 MW, fixed-speed active stalled wind turbine directly connected to the grid. The focus of this analysis is to observe the structural signals in the frequency range of the natural frequency of the generator speed.

4.1.1 Analysis of asynchronous generator

The full order asynchronous generator model, combined with the equation of conservation of motion is analyzed in Section A.3.4 (page 104, Appendix A). The analysis follows transient response to change in torque load, linearization of state space model, and eigen value analysis. The eigen values of the system matrix (Equation A.55) versus slip in the generator operation range, is shown in Figure 4.1. On the left vertical axis (blue) the real part

of eigen values, on the right axis (red) the positive imaginary part. Observe that eigen values are essentially constant around the operation range of the generator. The real part of stator flux linkages is around 2 Hz (blue dashed line), and the imaginary part is around 50 Hz (red dashed line). Similarly, the real part of the rotor flux linkages eigen values (blue solid line) is around 1 Hz, and the imaginary part (red solid line) is around 4 Hz. The eigen value corresponding to the generator speed, is a real value around 2 Hz for slip less than 5%.

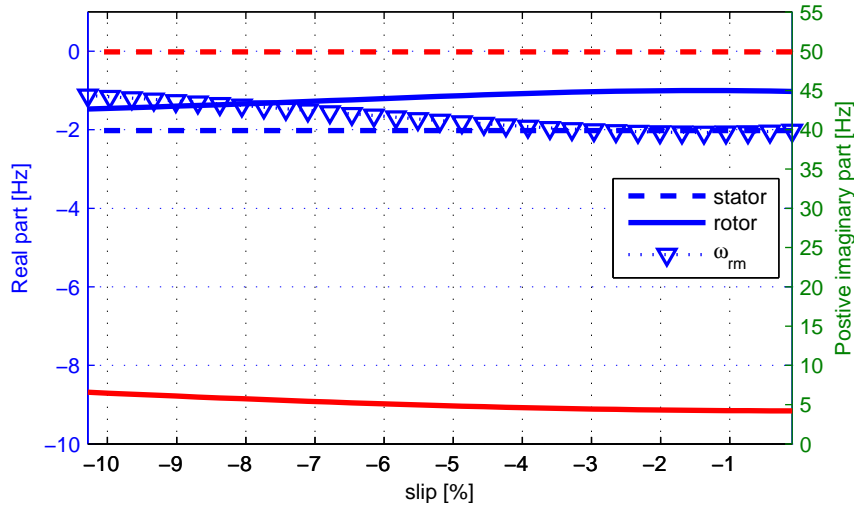


Figure 4.1: Eigen values of asynchronous machine with short circuited rotor, over different operating points of generator mode -blue lines are read with the vertical axis on the left, read lines are red with the vertical axis on the right.

Table 4.1 shows eigen values, damping ratio, and natural frequency of the corresponding modes of the asynchronous generator at rated operation, 0.4% slip. The purely electrical mode is given by the stator flux linkage eigen values, it has very low damping, and higher natural frequency than the mode corresponding to the rotor flux linkage eigen values. The electromechanical modes are given by the rotor flux linkages, and generator speed eigen values. The rotor flux linkage eigen values depend on machine parameters, and on generator speed. The generator speed eigen value depends also on machine parameters. Furthermore, it depends on number of magnetic poles, generator rotor inertia, and rotor flux linkages. This mode is a decaying mode that is critically damped. The electromechanical mode that stems from these eigen values, is more damped the purely electrical mode, and its frequency is much lower, actually in the range of structural modes and P-frequencies.

Table 4.1: Eigen values of asynchronous generator at 0.4% slip.

State	Eigen value $\sigma \pm j\omega$	Damping $\frac{-\sigma}{\sqrt{\sigma^2 + \omega^2}}$	Frequency f
stator ($\Delta\lambda_{ds}, \Delta\lambda_{qs}$)	$-2.02 \pm j49.92$	0.04	49.92
rotor ($\Delta\lambda'_{dr}, \Delta\lambda'_{qr}$)	$-1.01 \pm j4.21$	0.23	4.21
speed ($\Delta\omega_{re}$)	-2.04	1	0

4.1.2 Numerical simulation of fixed-speed wind turbine

This section presents numerical simulations results with the integrated simulation environment. Generator model and blade angle control in Matlab/Simulink, while the dynamics simulated in HAWC2 are stochastic wind field (turbulence, logarithmic shear profile), aerodynamic phenomena (tower shadow, dynamic and yawed inflow), and structural phenomena (large deflections, gyroscopic and centrifugal effects). The following Section 4.1.2.1 presents time domain simulation results, and Section 4.1.2.2 presents spectra of loads, and electromagnetic torque.

4.1.2.1 Time domain simulation results

This section presents time domain simulation results under normal operating conditions. Namely, operation during 600 s, under rated wind speed operation 12 m/s, with turbulence intensity of 10%. Figure 4.2 shows the wind speed perpendicular to the rotor at hub height (80 meters) on the top, the blade angle of the blades in the middle plot, and the power produced by the wind turbine. Observe the discrete kind of response of the blade angle, the control turns the blades towards stall (negative blade angle values) at high wind speeds to limit power, and turns the blades into the wind (positive blade angle values) when the wind speed is lower. However, the blade angle control is not fast enough to keep up with wind speed fluctuations, therefore the large power fluctuations typical of fixed-speed wind turbines.

Figure 4.3 shows the tower top, and tower bottom bending moments. On the top plot tilt moments, in the middle plot side-to-side moments, and on the bottom plot yaw moments. Obviously, the tilt and side-to-side moments on the tower bottom are larger than on the tower top, while the yaw moments in the same magnitude range. Figure 4.4 shows flapwise (M_x), and edgewise (M_y) blade root moments. The flapwise bending moment is clearly the most influenced by wind field turbulence, and has a larger absolute mean value than the edge wise bending moment.

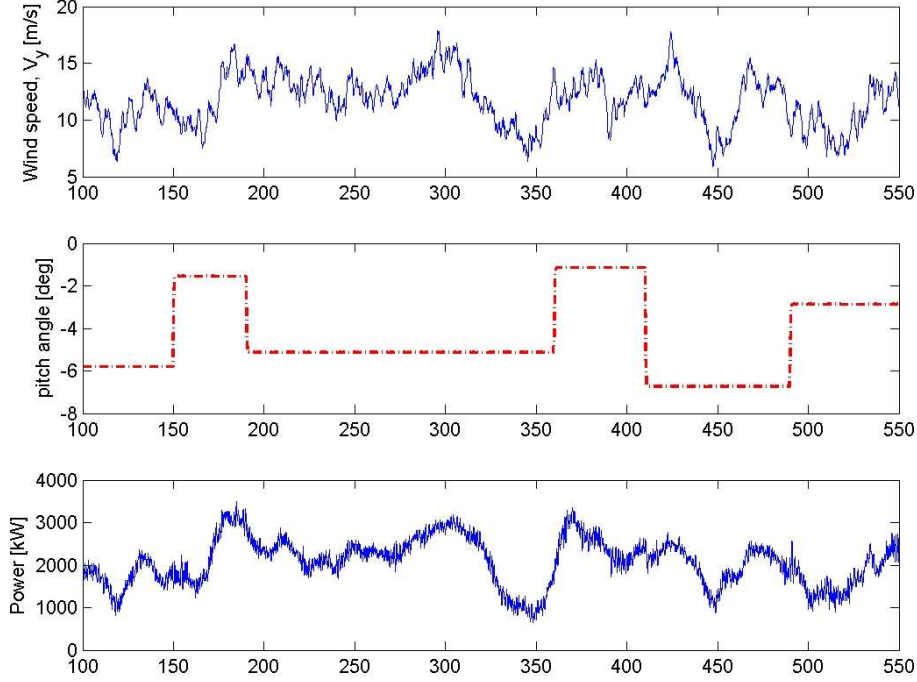


Figure 4.2: Wind speed, blade angle and power

4.1.2.2 Spectra of loads and electromagnetic torque

Analyzing spectral qualities of wind turbine loads, and electrical signals can provide information about some of the important dynamics of a wind turbine. It is however not simple to identify modes from time series, because wind turbines are very complex systems that have in practice many modes. Those modes also may change depending on the operating conditions. For example, P-frequencies naturally change with the rotational speed. Also blade modes change to some extent due to stiffening caused by inertial loads. For example, in [71] a Campbell diagram computed with HAWCModal for a similar wind turbine, shows the P-frequencies and wind turbine modes. The modes relevant for this study are (1) 3rd asymmetrical rotor flap/yaw + 1st tower yaw at 3.97 Hz, (2) 2nd rotor edge at 4.08 Hz, and (3) 3rd asymmetrical rotor flap/yaw + 2nd tower bending at 4.43 Hz. P-frequencies are straight forward to calculate, they are shown in Table 4.2 for rated speed.

The following Figures 4.5-4.7 (page 52) present the spectrum of structural loads (light colors), and electromagnetic torque (blue), calculated from a similar time simulation as the one presented in the previous section. In this

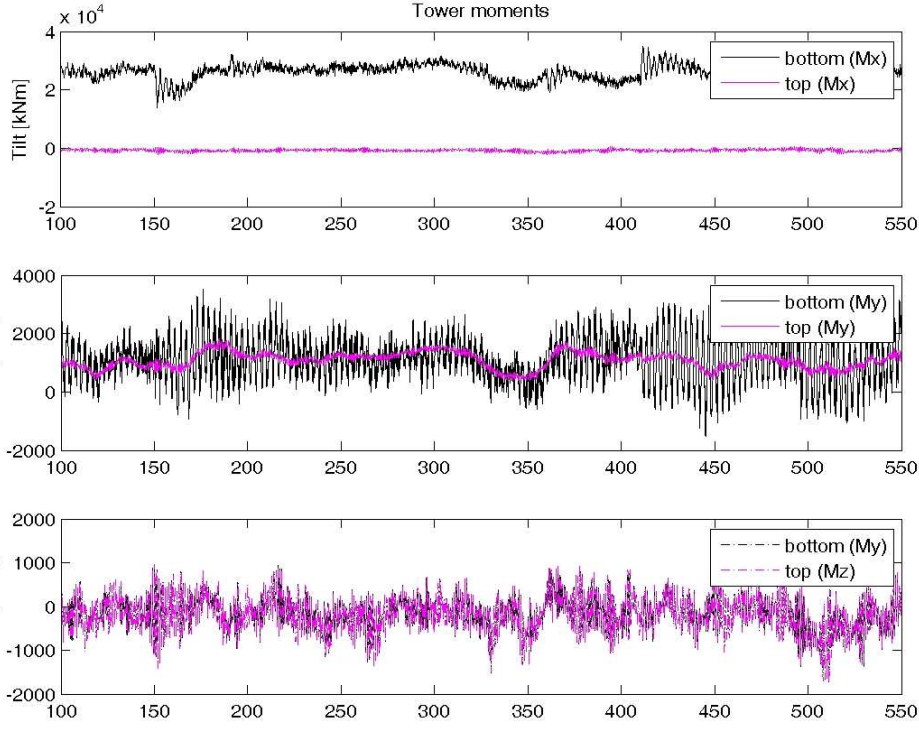


Figure 4.3: Top and bottom tower bending moments, from top to bottom: tilt, side-to-side, and yaw.

Table 4.2: P-frequencies at $\omega_h = 1.9713$ rad/s

1P	2P	3P	6P	9P
0.32	0.63	0.94	1.88	2.51

case however keeping the blade angle constant. These spectra have been normalized with the minimum value of each signal, therefore the spectral magnitude is not to be compared across signals, the reason is to make it simpler to compare frequencies of peak values. In every figure, one can observe the main P-frequencies very clearly in most of the signals. On the other hand, structural modes are seen in their corresponding signals, and in some cases across the structure. P-frequencies, and modes can be close to each other and therefore it can be hard to tell them apart.

The spectra of blade root bending moments, and electromagnetic torque are shown in Figure 4.5, the values of the main peaks in the spectra are indicated, they are P-frequencies and/or wind turbine modes.

Similarly, in Figure 4.6, the spectra of tower bottom bending moments and electromagnetic torque are shown, it can be observed that side-to-side tower

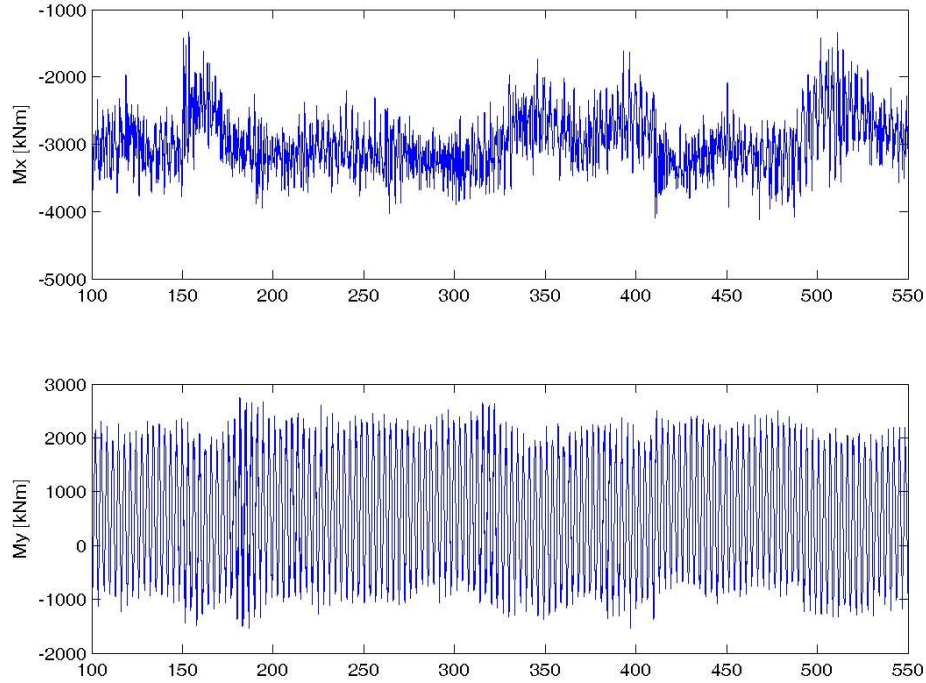


Figure 4.4: Blade root moments

moment, and yaw moment spectra show a peak at around 4 Hz. Notice also that electromagnetic torque shows a peak at around 4 Hz, as expected from the eigen value analysis, this should be the electromechanical mode from generator rotor flux linkages. It can also be an electromechanical mode combining the mode from rotor flux linkages and the mode from generator speed. Finally, Figure 4.7 shows spectra of shaft bending moments and electromagnetic torque. Modes above 3 Hz are very well damped in shaft bending moments spectra. Therefore, blades loads will not be significantly affected by modes from tower and generator at frequencies higher than 3 Hz.

4.1.2.3 Tower load spectra with different generator models

In the former spectra of loads, and electromagnetic torque presented in the previous section it can be observed that the spectrum of the side-to-side tower bottom moment has a mode that is close to that of the generator electromechanical mode. In this section to illustrate this case better, a comparison of spectra with different generator models is presented in Figure 4.8

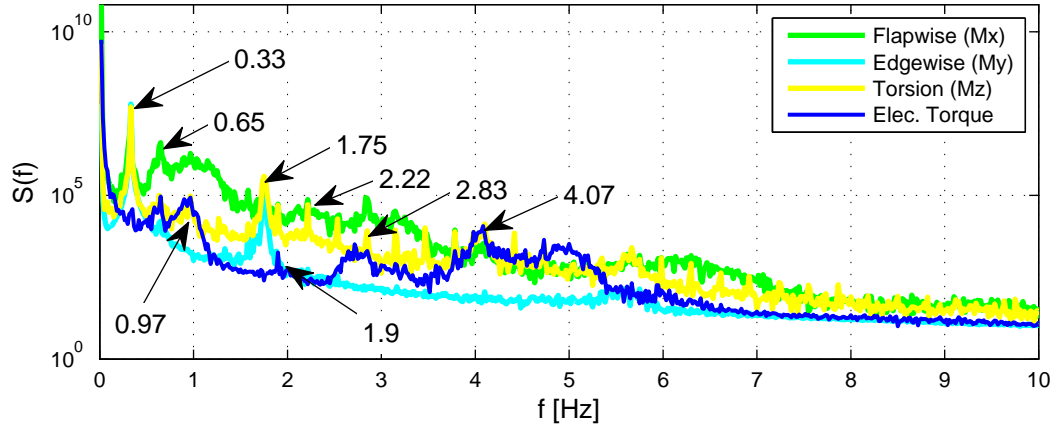


Figure 4.5: Spectrum of blade root bending moments and electromagnetic torque

(page 54). Namely, Figure 4.8a shows the spectra of tower bottom side-to-side bending moment with a full order model as in the previous simulations, and with a slip model. Observe that at around 4 Hz the spectrum from simulations with a full order generator model has higher energy than the spectrum from a slip model generator. Naturally, the same behavior is observed in the generator electromagnetic torque spectra, shown in Figure 4.8b.

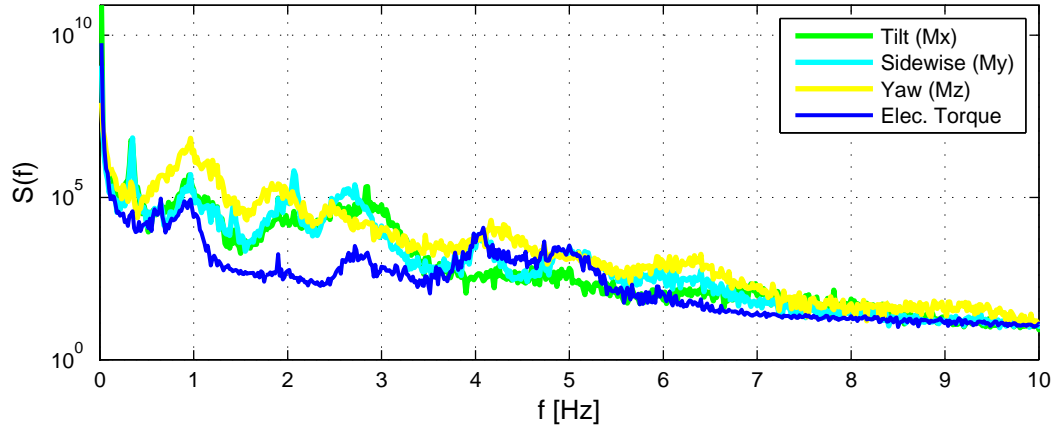


Figure 4.6: Spectra of tower bottom bending moments and electromagnetic torque

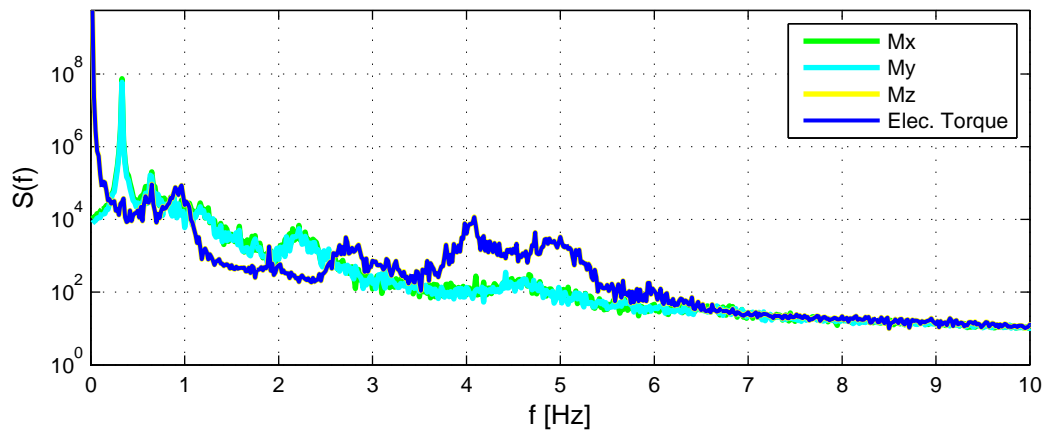
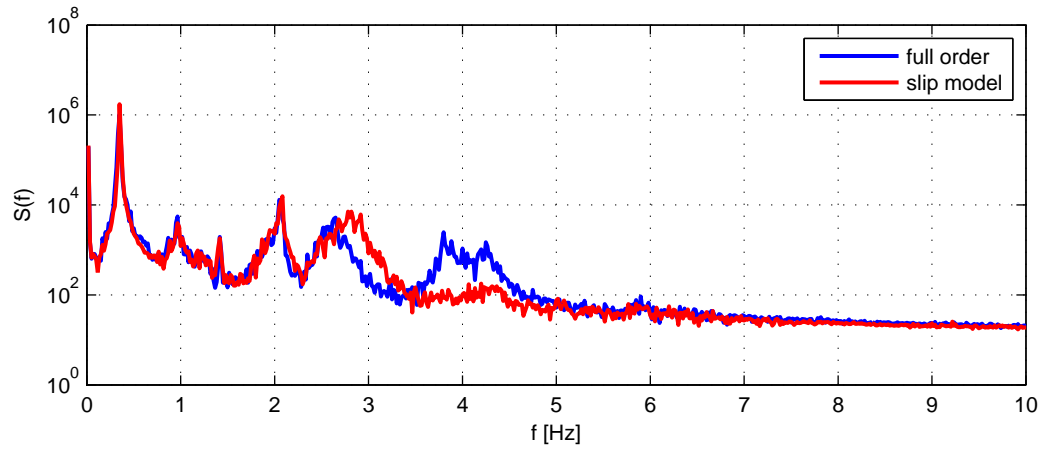
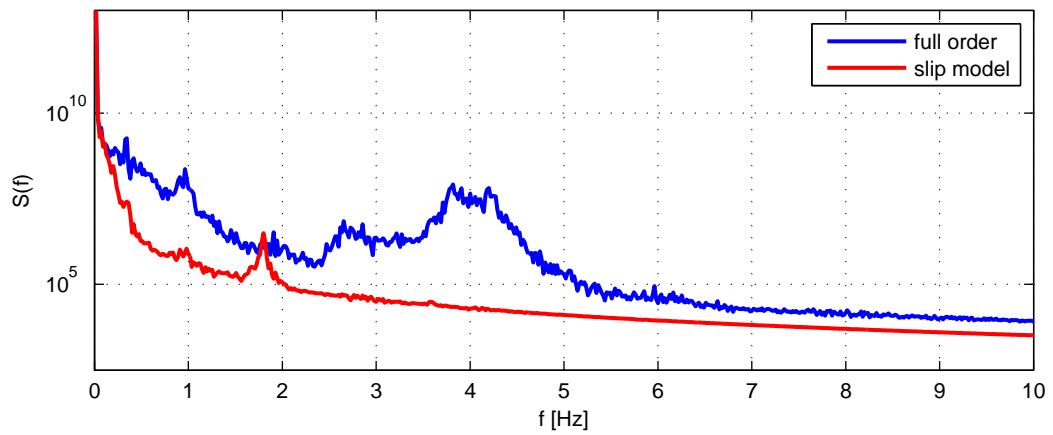


Figure 4.7: Spectra of shaft bending moments and electromagnetic torque



(a) Spectrum of tower bottom side-to-side bending moment with different generator models



(b) Spectrum of electrical torque with different generator models

Figure 4.8: Comparison of spectra with full-order, and slip generator model.

4.2 Dynamic analysis of wind turbines providing frequency support

Nowadays, wind power plants are conceptually able to provide any kind of ancillary services that modern power systems require. In the technical literature, it is widely proposed that given a sudden, and large unbalance of the power system active power, wind turbines can respond to help controlling the frequency within the system operator limits in order to avoid load shedding or system collapse. Such response may be intrinsic (i.e. fixed-speed), or controlled (i.e. variable-speed wind turbines).

Regarding the time frame of the response, and purpose of the control the simplest categorization of frequency response may be:

- instantaneous to within a few seconds (i.e. inertial response, primary response), or
- more than a few seconds after the event once the frequency is again stable, but not at its nominal value (i.e. secondary response)

This section presents numerical simulations of a variable-speed wind turbine (DFAG) proving frequency support, the focus is on inertial response. The objective is to demonstrate the integrated dynamic analysis of the impact on the structural loads of a wind turbine. Because, although it is intuitive that the more abruptly the inertial response control acts, the more stress the wind turbine subsystems will experience, there are no formal assessments of loads on wind turbines operating in this condition. Moreover, there are no models proposed to have a sensible estimation. For this purpose the power system model for frequency support, presented in Section 3.3.3 (page 3.3.3), is coupled to a wind farm. This system is shown in Figure 4.9, the power system composite response to changes in power balance is represented with a speed governor with droop, a prime mover (turbine), and the lump response of generation and load as described in Section 3.3.3. The wind farm is represented by an aggregation of a single wind turbine model.

Wind turbine aggregation. Simulation of the power production of a wind farm, from simulation of the power from a single wind turbine is not trivial. Most of the literature addressing inertial response of wind turbines ([78–85]) use constant wind input, except for [86] that compares two control concepts, and wind turbine technologies in terms of a so-called *wind disturbance margin*. In [82] the contribution of a single wind turbine is linearly aggregated to represent the total response of a wind farm. A linear aggregation makes sense when simulations are performed with a constant wind

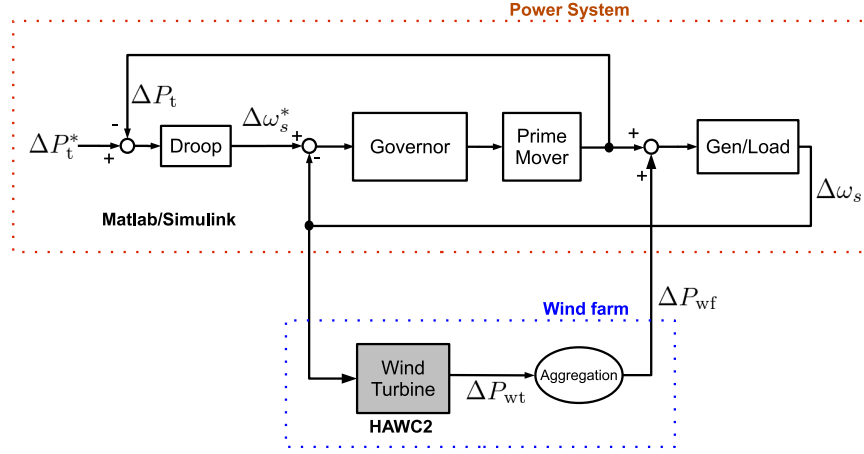


Figure 4.9: Integrated dynamic analysis model for power system frequency control.

speed field or velocity, Eq. 4.1 expresses a linear aggregation of the power from a single wind turbine to the power of a wind farm. P_{wf} is the wind farm power output, N_{wt} is the number of wind turbines, and $P_{wt,i}$ the power output of a single wind turbine.

$$P_{wf} = \sum_{i=1}^{N_{wt}} P_{wt,i} \quad (4.1)$$

A simple way of aggregating the power calculated with a single wind turbine model under turbulent wind field, is to assume that the power fluctuations from wind turbines are identical stochastic processes, normally distributed and uncorrelated. Furthermore, it can be assumed that the response of the wind turbines to the inertial response control is instantaneous and synchronized. Eq. 4.2 represents this simplified aggregation concept, $\delta P_{wt,i}^{tu}$ is the power fluctuations due to turbulence from a single wind turbine, and $\delta P_{wt,i}^{ir}$ the power exchanged between the wind turbine and the power system during the inertial response.

$$P_{wf} = \sum_{i=1}^{N_{wt}} (P_{wt,i}^o + \delta P_{wt,i}^{ir}) \sqrt{\sum_{i=1}^{N_{wt}} (\delta P_{wt,i}^{tu})^2} \quad (4.2)$$

Coupling to wind turbine model. The partial coupling of DFAG wind turbines to power system frequency was analyzed in [81], showing that DFAG is completely decoupled when the rotor current controller has a large bandwidth (i.e. is a fast controller, which is the case normally). This coupling is also considered marginal in [78–82, 84–86]. Therefore, the in this study

the power system frequency variation $\Delta\omega_s$ from the power system frequency control model is only an input to the inertial control response previously described.

Simulation results. The simulation case presented in this application example is that of a wind farm inertial response in case of loss of load. The simulations are done with a constant wind field at rated wind speed (12 m/s), the wind farm is composed of 6 DFAG wind turbines of 2 MW. The power system has total capacity of 60 MW, with standard speed governor-turbine settings, and lumped inertia and damping values.

Figure 4.10 shows the response of the power system frequency to an 8% loss of generation, two scenarios are simulated one with the wind farm operating and providing inertial response, and the other without the wind farm. As it is expected the frequency drop due to the sudden loss of generation is alleviated by the wind farm providing inertial response compared to the case where the wind farm is not active.

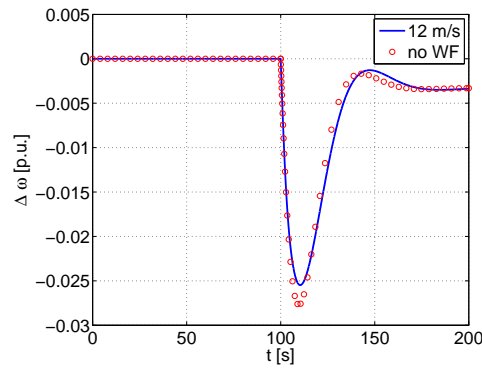


Figure 4.10: Power system response to loss of generation

The response of the wind turbine with inertial control during the sudden loss of generation is shown in Figure 4.11. The generator torque increases rapidly, as shown on the top plot in Figure 4.11a, from the instant that the generation loss occurs due to the inertial response control, this leads the speed in the low-speed shaft to drop, and consequently the blade angle control reacts turning the blades to catch more power from the wind. Figure 4.11b shows the structural loads that are most affected during this inertial response event, from top to bottom: the torsion on low-speed shaft, the tilt moment at the tower bottom, and the yaw moment at the tower top. Naturally, the tilt moment at the top of the tower and the yaw moment at the bottom of the tower are also affected during this operation. However, in a lower scale since in the case of the yaw the load is taken by the whole tower structure beginning at the top, the moment transferred to the bottom

4.2 Dynamic analysis of wind turbines providing frequency support 58

is largely damped. The increase in tilt moment is produced by the change in thrust, therefore much lower at the top than at the bottom of the tower.

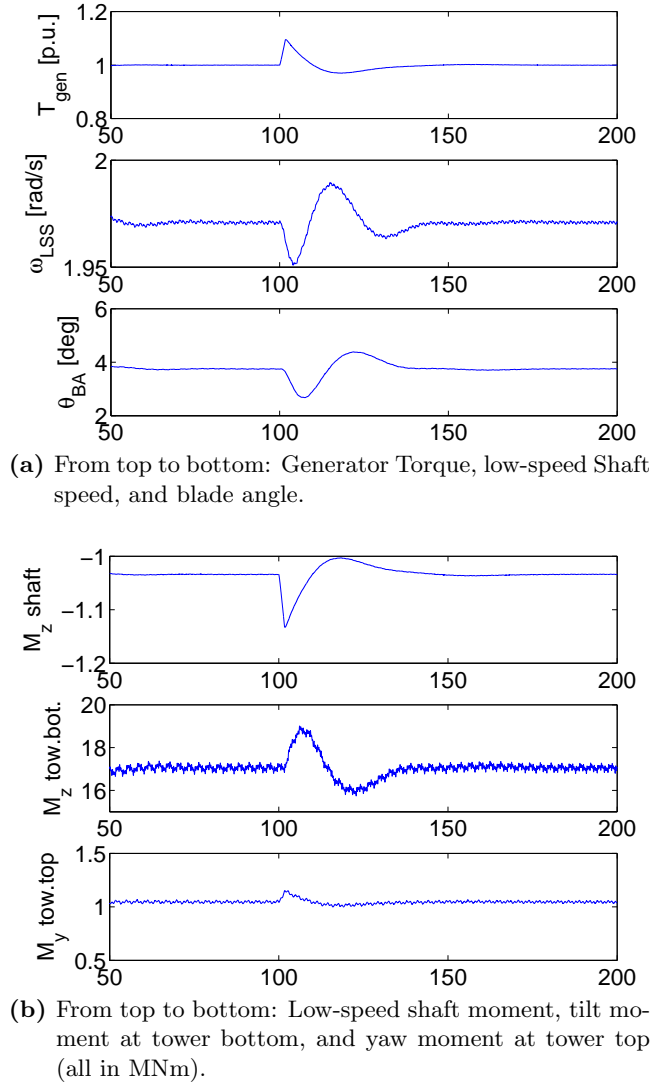


Figure 4.11: Wind turbine loads while emulating inertia.

4.3 Summary

This chapter presented application examples of the models, and the integrated design dynamic analysis environment previously developed. Namely, an analysis of the dynamics of an asynchronous generator was presented, the eigen of generator flux linkages, and rotor speed were mapped for different operation points. Numerical simulations of a fixed-speed wind turbine showed that a side wise tower mode is very close to the electromechanical modes of the generator. These modes therefore couple, as can be seen in the spectra by an increased energy at around 4 Hz, when the generator model includes the rotor fluxes dynamics. Despite this coupling the system was stable under the conditions simulated.

Furthermore, a integrated analysis of a wind farm providing inertial response to contribute the control of the power system frequency during a loss of generation was presented. This integrated analysis allows to simulate the impact on the power system frequency of inertial response from wind turbines, while also the dynamic response of generator system, blade angle control, and structural loads can be studied. It was observed that torsion at the shaft, tower bottom tilt moment, and tower tow yaw moment are the structural loads affected on wind turbines providing inertial response with the controls described.

The application examples presented in this section give confidence in the integrated simulation approach and models developed in this Ph.D. project. These examples also show that there are advantages from an integrated simulation approach.

Impact of voltage faults on wind turbine structural loads

This chapter presents the application of the simulation environment described in Section 2.3, and models described in Chapter 3 to study the dynamic response of a wind turbine due to a fault of the supply voltage. The case of a balanced voltage fault is addressed in Section 5.2, while the case of unbalanced voltage fault is treated in Section 5.3.

5.1 Introduction

This is a general introduction to the issues related to faults of the supply voltage of wind turbines. A fault is a short-circuit somewhere in the power system, for example in one or more phases of a transmission line. In the context of this work a *fault of the supply voltage*, is essentially a sudden reduction of the voltage magnitude at the terminals of the generator of a wind turbine. A detailed definition, and classification of voltage magnitude events according to international standards can be found in [91]. The case simulated in Section 5.2 falls in the category of instantaneous interruptions: a complete voltage drop that lasts less than 0.5 seconds.

When a fault occurs the current increases rapidly, the protections then activate to isolate the fault, and the voltage comes back to normal. During the fault, the wind turbine generator loses (completely in the case of a balanced fault, and partially in the unbalanced case) its capacity to produce electromagnetic torque to counteract aerodynamic torque. Therefore, wind

turbines used to be disconnected from the power system, and shut down to avoid an uncontrollable situation that could potentially damage them. However, with a high share of wind power in a power system, disconnecting many wind turbines suddenly would compromise the stability of the power system. Therefore requirements for wind turbines to stay connected during low voltage have been adopted by power system operators in many countries already since the end of the nineties. Such requirements are referred to as *fault ride-through* (FRT) or *low voltage ride-through* (LVRT). A review the requirements in place at the distribution, and the transmission level in Denmark, Ireland, Germany, UK, Spain, Italy, USA, and two provinces of Canada is presented in [91]. Emerging markets of wind power like the Chinese have introduced LVRT requirements as of 2009 [92]. The requirements of different countries differ mainly in (a) the duration and magnitude of a fault that a wind turbine must ride-through, (b) the behavior of the wind turbine current injection current during and after the fault. Discussion of the different requirements, and the implications to wind turbine FRT capability is outside the scope of this work.

Naturally, studies of FRT have been undertaken mainly with simple models oriented to power system stability. Such models include simple representation of aerodynamics and drive train, e.g. by a C_p curve, and either the swing equation or a two mass model to represent the torsion of the low speed shaft [5, 50, 52, 74, 75, 77, 93–100]. The question of whether taking into consideration the dynamics of the wind turbine rotor structure has an impact on the transient performance of wind turbines has been addressed in [10]. The conclusion is that a two mass model may not be enough for transient stability studies, because some torque oscillations that could with the electrical system are not considered. An *effective* two mass model was proposed that takes into consideration the dominant low frequency dynamics of blades, and shaft. However, such models are not enough when the objective is to verify that a given wind turbine design can FRT according to grid operator requirements, and at the same time verify the structural loads are not prohibitive, and that components are not exposed to dynamic loads outside their design specifications. Therefore, this Ph.D. project by means of combining simulation tools in an integrated simulation environment, contributes to these investigations.

Regarding FRT wind turbine control, it has been shown that for DFAG wind turbines adding a damping control loop can reduce drive train oscillations that otherwise are only slightly damped 10 seconds after the fault [52, 53]. The influence of control parameters on the behavior of the wind turbine protection system after the fault is studied in [94], the selection of the protection system (i.e. the value of the crowbar resistance) is treated in [96]. In [94] it is shown that the proportional gain (K_{p2}) of current control loops have an impact on the performance of the generator after the fault,

to the extent that the protection system can be activated again, when the fault is cleared. A *lower* K_{p2} will allow a higher stator (and rotor) current, whereas a higher K_{p2} will reduce the maximum value of current. Furthermore single-cage, and double-cage operation of rotor circuit yields a different rotor current and therefore different rotor speed response to sudden voltage changes with a *low* K_{p2} , of the current control loops [94]. However with the more aggressive controller (i.e. higher K_{p2}) the rotor speed response is essentially the same. It is important to notice, that even if the speed response was similar in the case with high K_{p2} , the electromagnetic torque and stator current were not. Consider that double cage is principally changing the rotor resistance, and so does the crowbar, the ratio of crowbar resistance to rotor resistance plays also a role in the response to the fault [96]. In general, a higher crowbar resistance reduces the slope of the torque-speed, and reactive power-speed curves [52]. Therefore, a higher crowbar resistance makes the electromagnetic torque less sensitive to changes in speed, and reduces the reactive power consumption of the generator at a given speed.

5.2 Balanced voltage fault

The general objective of this section is to analyze the impact that a balanced supply voltage fault, and wind disturbances have on the structural, and the electrical systems of a DFAG wind turbine. The focus is on dynamics below 50 Hz, disregarding very high frequencies (gearbox dynamics, and converter switching). Figure 5.1 illustrates the interaction of the subsystems modeled, where the power system model is the grid equivalent model described in Section 3.3.2, the asynchronous machine is the full order model, the generic generator and blade angle controls are used with the proportional set point damper described in Section 3.2.3.6.

The impact of wind disturbances, and a fault without reconnection of the rotor side converter are qualitatively analyzed in Section 5.2.1, while Section 5.2.2 studies the dynamic response to a fault, with activation and deactivation of the protection system.

5.2.1 Wind disturbances and fault

Analysis of a variable-speed wind turbine under a fault –which does not trip the protection system–, using models that consider aerodynamics and a modal representation of the structure, can be found in [9]. In general, the tower lateral acceleration, and the low-speed shaft twist angle/moment of fixed- and variable-speed wind turbine, are known to be sensitive to voltage faults [9, 19, 21].

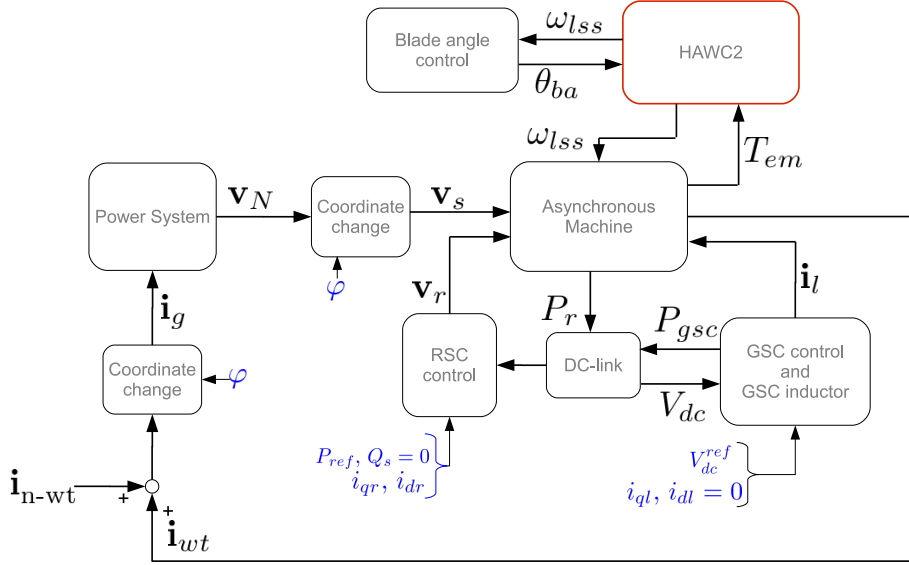


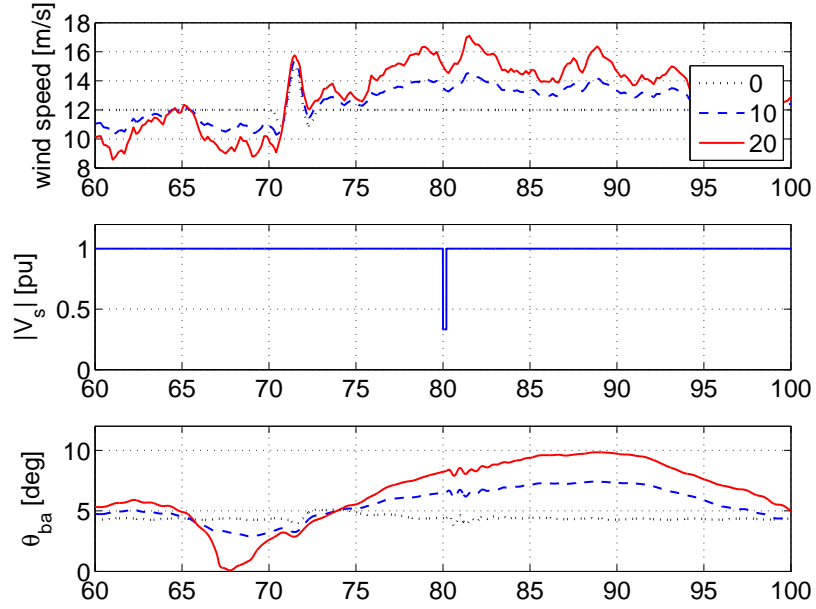
Figure 5.1: Block diagram illustrating the subsystems modeled with the main variables they exchange, (blue quantities are references or measurements).

The first simulation case is shown in Figure 5.2, it consists of simulations with 0%, 10%, and 20% turbulence. The events simulated in this case are a wind gust and a voltage fault. The wind gust is 3 m/s simulated at $t = 70$ s, Figure 5.2a shows wind speeds in the top plot.

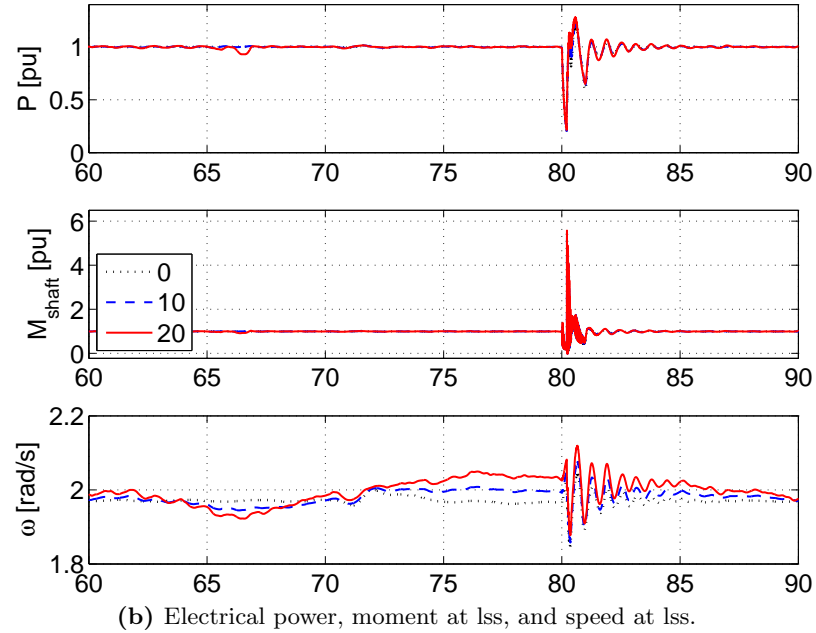
A balanced AC fault at one of the lines of the double circuit is simulated at $t = 80$ s, the voltage drops to about 0.3 p.u., the fault is cleared after 200 ms, and the voltage comes back to normal. Figure 5.2a shows the voltage at the wind turbine terminals in the middle plot. When the fault occurs the protection switch disconnects the RSC, the RSC stays disconnected.

Figure 5.2b shows electrical power in the top, in the middle plot the torque at the low-speed shaft, and the rotational speed of the low-speed shaft is shown in the bottom plot. Observe that the torque on the low speed shaft is significantly high at the moment the voltage comes back to normal, it reaches nearly six times the value during normal operation. Moreover, it can be observed in Figure 5.2b that the wind gust induces variations of the speed ω (i.e. speed at low-speed shaft). These variations induce fluctuations in the power that are reflected in the DC-link voltage (Figure 5.2c), however not dramatically.

Furthermore, from Figure 5.2b it can be seen that as ω is generally fluctuating more with higher turbulence, also during the fault the fluctuations of ω are larger with higher turbulence. Evidently, the same behavior is expected from other structural and electrical variables. This can be observed from



(a) Wind speed, stator voltage, and blade angle.



(b) Electrical power, moment at lss, and speed at lss.

Figure 5.2: Case 1. Response to wind gust, turbulent wind, and AC fault.

Figure 5.2d in the tower side-to-side moments. However, in the electrical variables the influence of the turbulence is not so noticeable, for example in the rotor current, DC-link voltage and electromagnetic torque shown in Figure 5.2c.

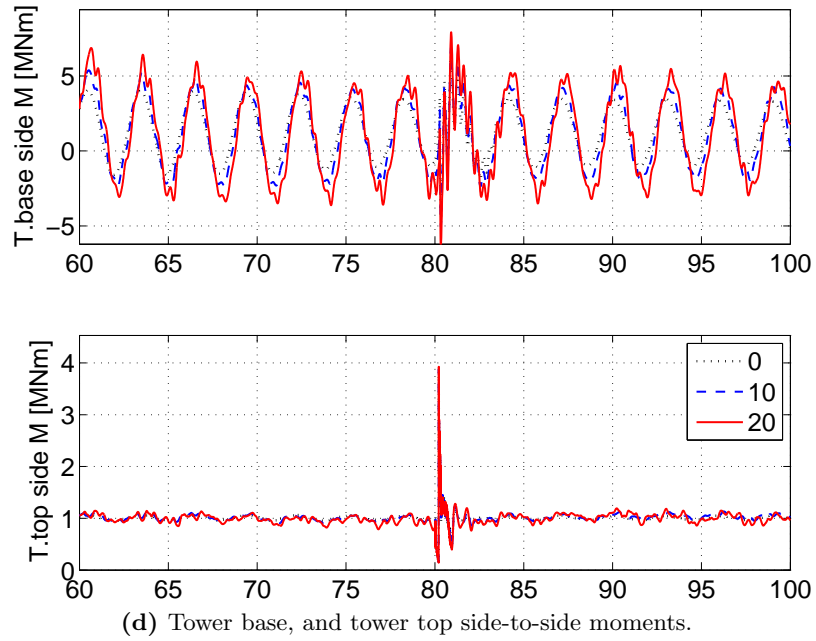
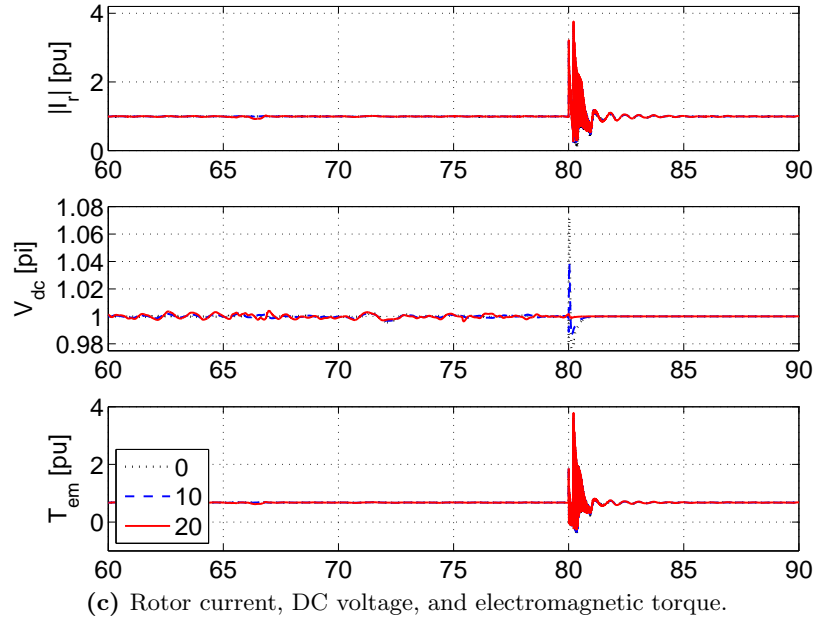


Figure 5.2 continued: Case 1. Response to wind gust, turbulent wind, and AC fault.

5.2.2 Fault and reconnection

In the second simulation case Figure 5.3, a balanced fault in one of the lines of the double circuit is simulated at $t = 60$ s with the same characteristics as in the previous case, while the wind is kept constant, as shown in Figure 5.3a. The over-current protection of the RSC activates itself when the rotor current exceeds the threshold, and deactivates when the duty cycle is met and the current and voltage are back to normal.

Figure 5.3b shows on the top plot the electrical, and the aerodynamic power, observe that the electrical power falls abruptly during the fault, while the aerodynamic power does not drop because the wind turbine blade angle control is working in normal operation. The aerodynamic power however, does fluctuate after the fault, due to the changes of electromagnetic torque that impose fluctuating loads on the shaft (M_{fx} and M_{mid} in middle plot) that in turn produce changes of speed ω_{lss} , and ultimately oscillations of the hub speed ω_{hub} (bottom plot). Figure 5.3c, illustrates the effect of the fault and the role of the over-current protection on the rotor current $|I_r|$, dc-link voltage V_{dc} , and electromagnetic torque T_{em} . Namely, it can be observed how V_{dc} responds after the fault, once the protection is removed. Figure 5.3d shows that the loads on tower top side-to-side moment during the fault, and the removal of the protection can reach relatively high peak values.

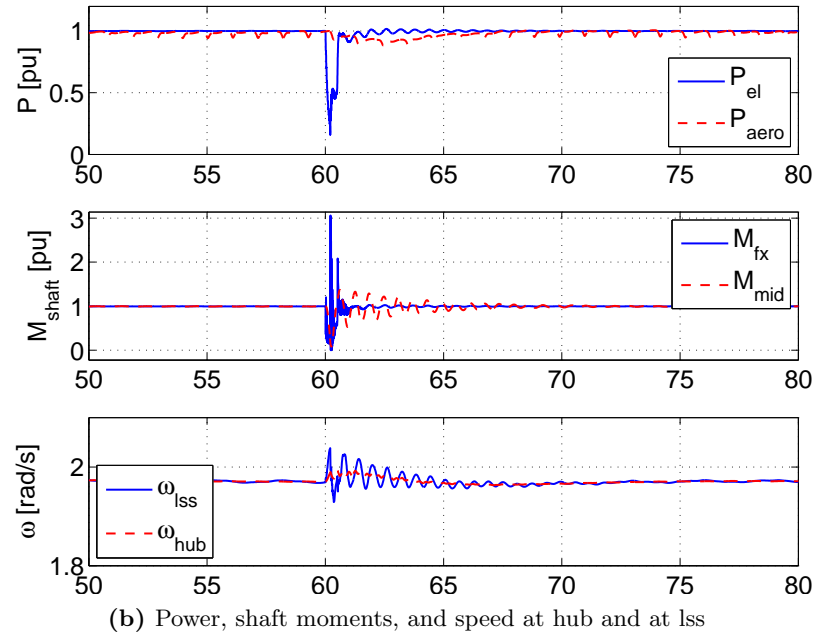
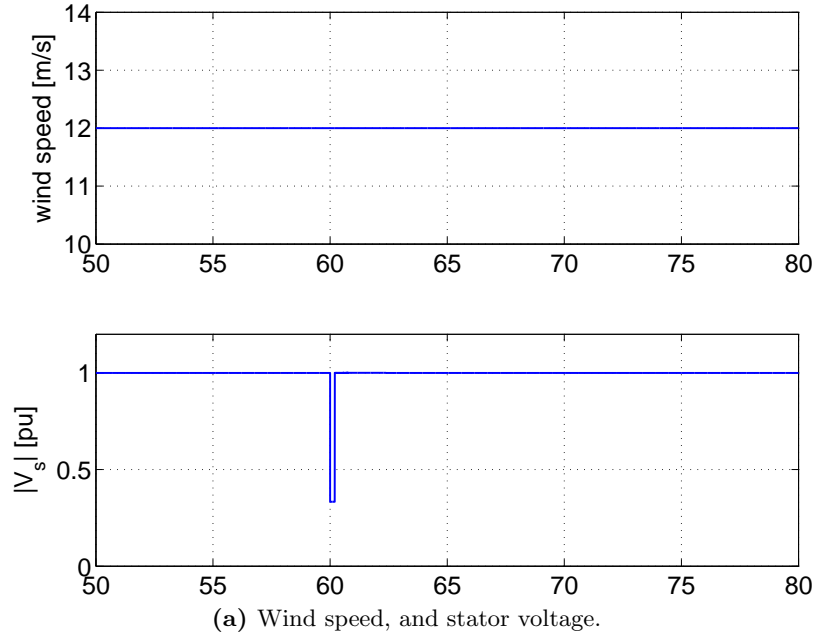


Figure 5.3: Case 2. Response to AC fault with over-current protection

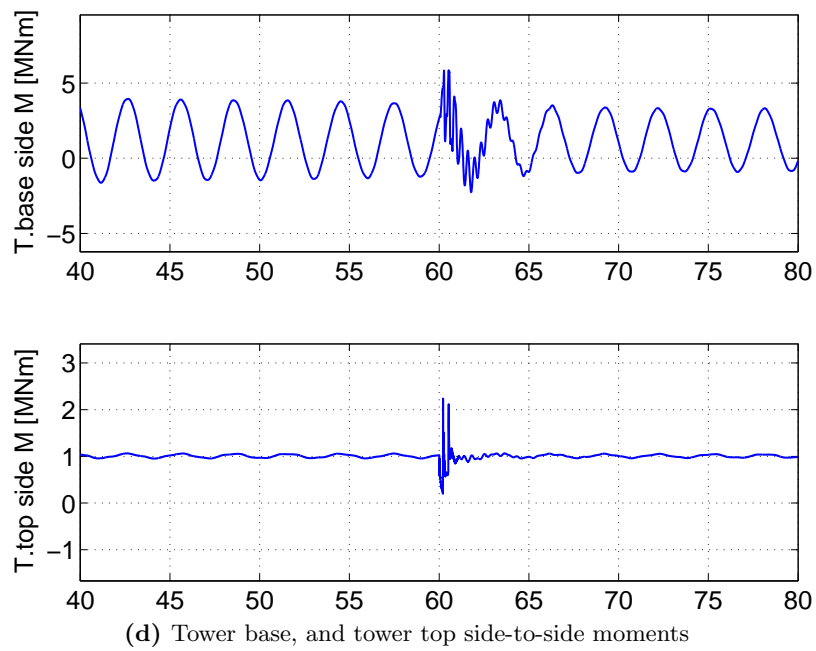
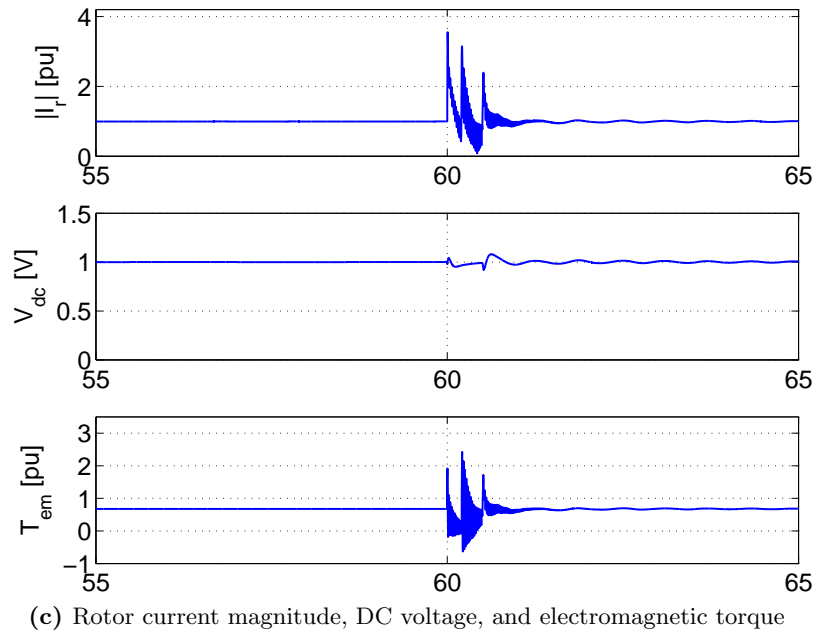


Figure 5.3 continued: Case 2. Response to AC fault with over-current protection

5.3 Unbalanced voltage fault

This section presents an integrated dynamic analysis of a wind turbine during an unbalanced voltage fault. Unbalanced faults are more common than balanced faults, and according to [89, 101–105] electromagnetic torque oscillations produced by unbalanced supply voltage may *damage* wind turbines.

The purpose here is to study the potential for load reduction. The impact on loads is measured in terms of 1-Hz equivalent loads, and maximum-minimum values relative to those during normal operation. The most important aeroelastic, structural, electrical, and control dynamics are considered in the integrated simulation environment described previously.

The particularities of an unbalanced fault, a review of controls for DFAG generators under unbalanced voltage supply, and a description of equivalent loads can be found in the following Sections 5.3.1, 5.3.2, and 5.3.3 respectively.

The dynamic response of control variables, structural loads, and electrical variables is discussed on the basis of the simulation results in Section 5.3.4. Quantification of load reduction potential using resonant damping control is addressed in Section 5.3.5.

5.3.1 Torque oscillations due to unbalanced voltage

The assumption of balanced voltages, and symmetric circuit parameters makes it possible to analyze multi-phase circuits by means of single-phase equivalent circuits. For example, voltages in a balanced 3-phase circuit can be represented by a set of 3 phasors of equal magnitude, displaced 120 degrees from each other (i.e. a balanced set of phasors); when the voltages are unbalanced it is possible to transform the unbalanced set of phasors, to three sets of balanced phasors (i.e. positive, negative, and zero sequence) using Fortescue's theory of symmetrical components [76]. Therefore, in general the analysis of 3-phase circuits under unbalanced conditions should include positive, negative, and zero sequences. However, when an unbalance voltage fault occurs somewhere in the power system, the voltage at the terminals of a typical DFIG wind turbine will not include a zero sequence due to the connection (D-Y) of the step-up transformer. Furthermore generator stator circuit [101], and power converter normally do not have a neutral conductor, and so zero sequence will disappear [97]. Negative sequence supply voltage will induce oscillations of fluxes, DC-link voltage, and grid-filter current at twice the supply voltage frequency [97]. Flux oscillations give rise to electromagnetic torque oscillations, it is intuitive that such torque oscillations will increase mechanical stress, or even damage wind turbine components

according to [89, 101–105].

5.3.2 Review of control techniques

In [102] torque, and reactive power oscillations induced by unbalance voltage supply are reduced adding feedback compensation terms of rotor and stator currents to RSC current control references. Control of RSC using vector control and flux-linkage observers during an unbalanced voltage fault is demonstrated with simulations in [106]. In [89], torque and reactive power measurements are compensated and fed back to RSC voltage references. The compensation is done with a resonant filter and lead compensation (i.e. resonant damping control -RDC). Reduction of torque, and reactive power oscillations is shown with experiments and simulations. A RSC current control based on negative and positive sequence decomposition is shown in [107]. Based on analytical results, [107] states that the voltage rating of RSC has to be increased in order to control the negative sequence current. The worst condition is at high rotor speed, and large unbalance [107]. Different techniques for coordinated control of RSC and GSC during unbalanced supply voltage are presented in [103, 104, 108–116], where also unbalanced faults are addressed in [103, 108, 110, 111, 115, 116]. Proportional resonant (PR) control is used in [113], proportional integral plus resonant (PI-R) control is used in [112], both rely on resonant filters that are formulated as second order systems with low damping ratio ζ (i.e. Eq. 3.10). This formulation is common in control of inverters, for example PR control in [117] is used for current/voltage control of grid connected inverters with advantages over conventional PI control such as reduced computational effort, and selective harmonic compensation. Other example of resonant filters is [89], where filters are formulated as second order filters with a high quality factor Q (i.e. Eq. 3.9). Either formulation results in a system that resonates at a given frequency when Q is high, or ζ is low (i.e. $2\zeta = 1/Q$).

In this Ph.D. project, damping controls were developed as described in Section 3.2.3.6 (page 35). The control concepts developed for unbalanced operation have been applied in studies conducted during this Ph.D. project, to investigate the reduction of structural loads under different wind conditions. For example, the basic damper (Figure 3.11, 36) and the RD-Comp control (Figure 3.14, 38) have been shown to reduce structural loads. However, when these controls are used under normal operation, wind turbulence will have a large impact on the power output. RD-SW control was developed to address normal operation under turbulent wind, results are presented in [118] and in the following sections.

5.3.3 1-Hz equivalent loads

In order to compare the impact on fatigue loads between normal operation and the operation under a fault, a 1-Hz equivalent load is calculated for each case, and normalized with respect to a based case. The concepts of equivalent damage, and equivalent load applied to wind turbine fatigue loads are addressed in [119–123]. The equivalent load S_o given by Eq. 5.1, used in this work is that defined in [121]. S_o represents a constant load amplitude that for a choosen equivalent number of cycles N_{eq} (i.e. 1 cycle per second means a one-hertz equivalent load), would produce the same damage as a load spectrum with n_i cycles for F_i load amplitudes. n_i and F_i are calculated using a rainflow counting algorithm [124]. m is the slope of the material cyclic stress to cycles-to-failure (SN curve), representative values for materials that would mainly constitute shaft, blades, tower top, and tower bottom were used according to [125].

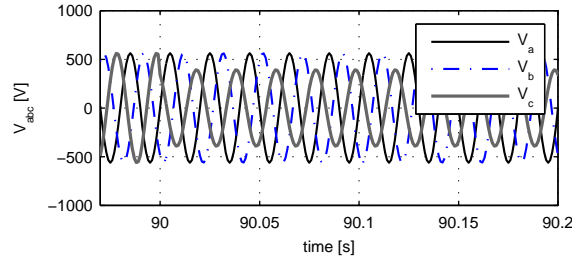
$$S_o = \left(\frac{1}{N_{eq}} \sum_{i=n} n_i F_i^m \right)^{\frac{1}{m}} \quad (5.1)$$

5.3.4 Simulation results

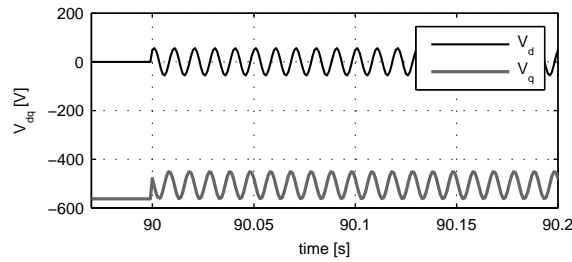
Three simulation cases are considered in order to estimate the relative impact of an unbalance fault on structural loads. The operation under normal conditions without any fault of the supply voltage is the base case, referred to as: **normal**. The second case is when an unbalanced fault occurs and the resonant damping control (RD-SW) is applied, this case is labeled as **damper**. The third case is when an unbalanced fault occurs, and no special control to damp the oscillations is used, in the figures this is labeled as: **unctrl.fault**.

An unbalanced fault in the power system, seen at the terminals of the wind turbine generator as a single-line-to-ground fault was emulated by dropping the voltage magnitude of one phase to 70% of its nominal value during 600 ms. 3-phase and dq voltages are shown in Figure 5.4, 100 Hz oscillations due the unbalanced is of 3-phase voltages are seen in dq voltages.

Electrical loads are shown in Figure 5.5, on the top plots the response of the RSC control variables (v_{dr} , and v_{qr}) to the fault is shown in terms of the magnitude of rotor voltage $|V_r|$, and magnitude of rotor current $|I_r|$; total active power P_{tot} , and stator reactive power Q_s are shown in the bottom plots. Figure 5.5b is a zoom of Figure 5.5a at the instant that the fault is cleared, voltage goes back to normal, and control switches back to P_{tot} , Q_s , i_{qr} , i_{dr} . From Figure 5.5a it can be seen that as the fault occurs at 90 s, the damper is activated to reduce torque, and reactive power oscillations



(a) 3-phase stator voltage



(b) dq stator voltage

Figure 5.4: Voltage at stator terminals at start of unbalanced fault.

(i.e. **damp**er), the rotor voltage fluctuates more compared to the case when there is no special control during the fault (i.e. **unctrl.fault**). After the fault the RD-SW helps to reduce the oscillations induced by the sudden restoration of the stator voltage.

Structural loads in Figure 5.6 show the response of the wind turbine to an unbalanced fault, only the structural loads that are most influenced are presented: shaft torsion, tower bottom and tower top side-to-side moment.

5.3.5 Quantification of load reduction

This section compares structural loads amongst different simulation cases, with different wind conditions and control settings in order to quantify the possible reduction of structural loads and the impact on electrical variables. Comparison of loads for different wind speed turbulence intensities is done in Section 5.3.5.1 to ponder the influence of turbulence intensity, also to measure the load reduction potential using RD-SW.

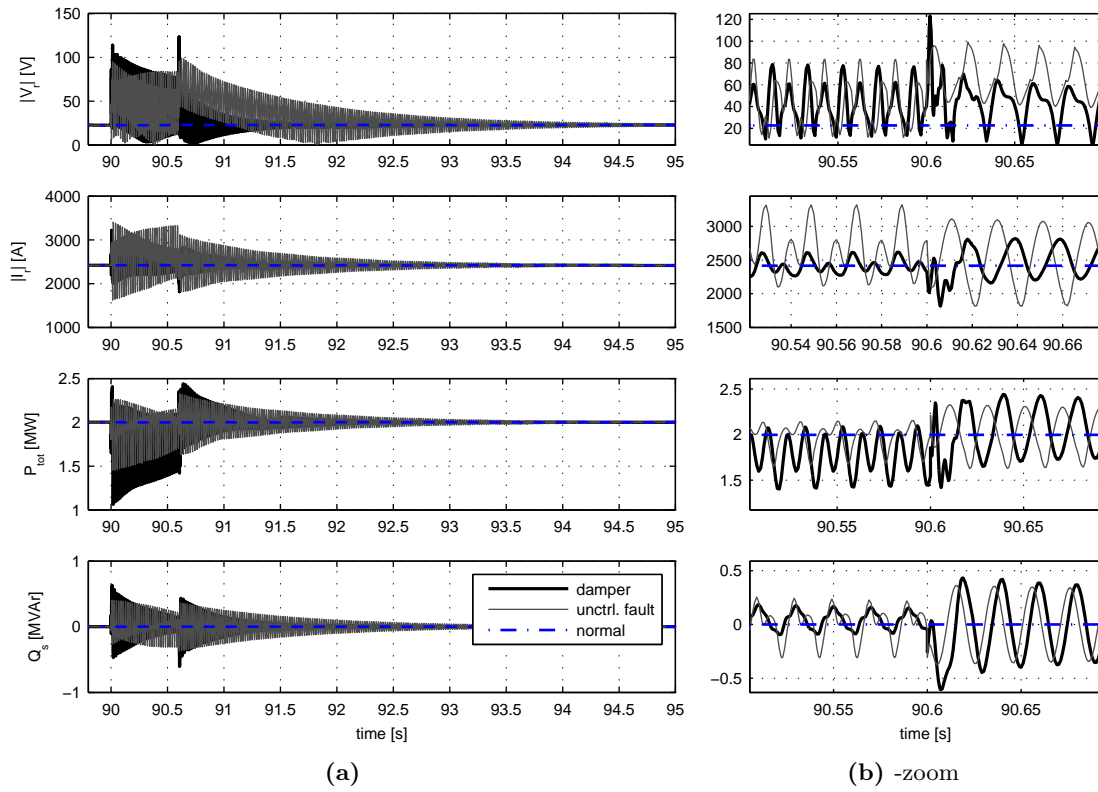


Figure 5.5: Electrical loads from top to bottom: rotor voltage and current, total active power and stator active power. In each plot, normal operation with dash-dot (**normal**), unbalanced fault with RD-SW in solid thick (**damp**), and unbalanced fault with normal control in solid thin line (**unctrl. fault**).

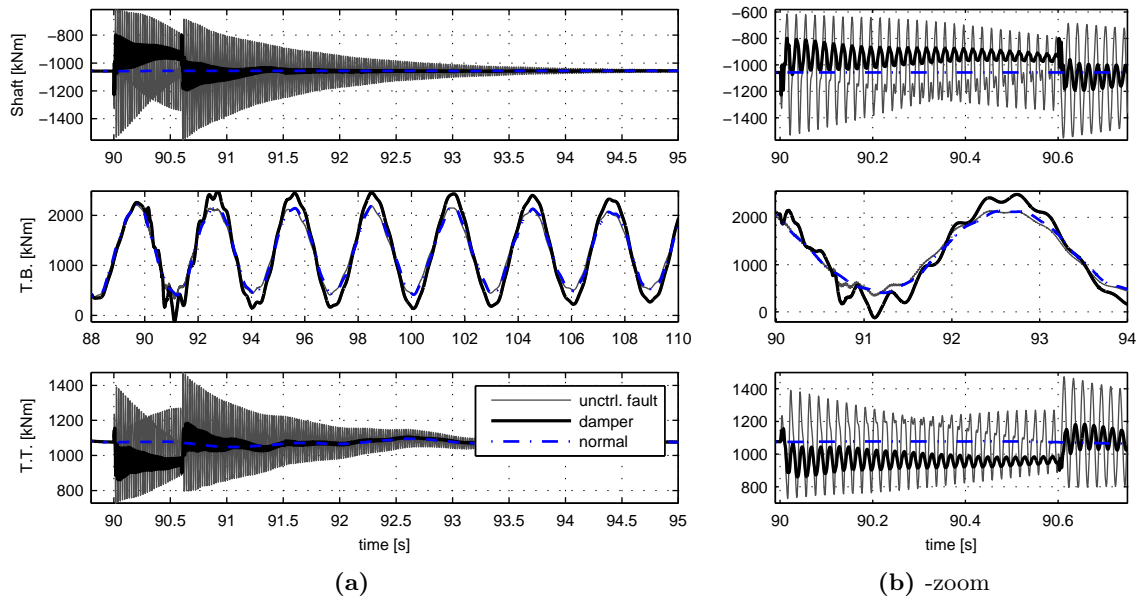


Figure 5.6: Structural loads from top to bottom: shaft torsion, tower bottom (T.B.) and tower top (T.T.) side-to-side moment. In each plot, normal operation with dash-dot (**normal**), unbalanced fault with RD-SW in solid thick (**damp**), and unbalanced fault with normal control in solid thin line (**unctrl.fault**).

5.3.5.1 Comparison of loads at different turbulence intensities

Relative fatigue loads. The concept of 1-Hz equivalent load S_o was described in Section 5.3.3, rainflow calculations on time series of loads (i.e. Figure 5.6) yield 1-Hz equivalent loads S_o according to Eq. 5.1. Normalized S_o of structural loads at different wind speed turbulence intensities are presented in Figure 5.7. It is intuitive that increased turbulence intensity will yield more load cycles, therefore larger S_o . Figure 5.7 illustrates the influence of turbulence intensity on S_o of shaft torsion, tower bottom (T.B.) and tower top (T.T.) side-to-side moments, by comparing the **damper** to the **normal**, and to the **unctrl.fault** case.

Bare in mind that the stochastic nature of S_o is not represented here, namely that each data point is actually one sample (at one wind turbine operating point) of an stochastic variable whose probability distribution function depends on many parameters, mainly on wind speed distribution and coherence [121]. A comprehensive statistical analysis is outside the scope of this work, it is however interesting when considering to evaluate the actual cost of reducing loads over life-time.

The general conclusions from Figure 5.7 are (1) an unbalance fault imposes very large shaft and tower top loads, (2) RD-SW can reduce shaft and tower top at the expense of increasing slightly tower bottom loads, (3) even with RD-SW loads due to unbalance fault are extremely large. These conclusions are further explained, for example regarding shaft normalized S_o , Figure 5.7b shows that **damper** is less than 40% of **unctrl.fault**, this means that RD-SW control is achieving a 60% load reduction of shaft S_o . However, the comparison of shaft S_o between **damper**, and **unctrl.fault** in Figure 5.7a shows that the shaft S_o in **damper** are about 70 times those in **normal** at very low turbulence intensities; while at higher turbulence intensities this difference is reduced to about 45 times. Similar conclusions can be drawn regarding the tower top side-to-side loads, where at low turbulence intensity **damper** S_o are about 4.5 times **normal** S_o . This demonstrates that using a control strategy to reduced shaft and T.T. loads imposed by an unbalanced fault is important.

Furthermore, from Figure 5.7b the reduction of shaft torsion and T.T. moment is very significant in **damper** compared to **normal**, however T.B. moment is increased in **damper** compared to **normal**, particularly at lower turbulence intensity values (i.e. below 0.1). Moreover, comparing the trends of plots in Figure 5.7b to those of Figure 5.7a it can be said that given an unbalanced fault the influence of turbulence intensity on S_o of shaft and T.T. is not as large as during normal operation, whereas for T.B. turbulence intensity has similar impact with and without an unbalanced fault. This supports the information from time series with 0 turbulence intensity shown in

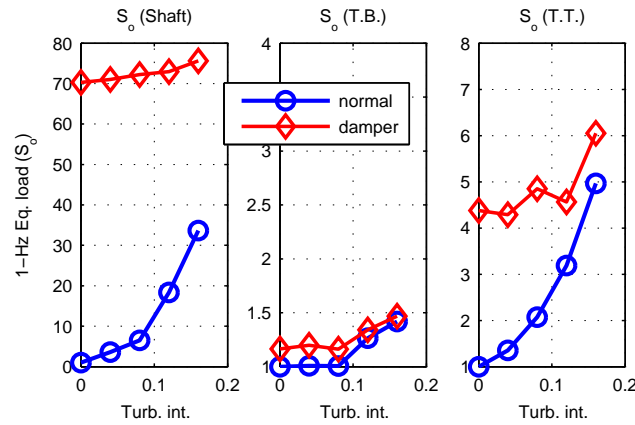
Figure 5.6, and suggests that the potential for reducing loads at the shaft and T.T. is the same regardless of the turbulence intensity, whereas the negative impact of reducing such loads seen on T.B. is mostly relevant at lower turbulence intensities.

Extreme loads. Similar analysis as those for relative fatigue loads are now presented for extreme loads. Maximum and minimum values of structural loads are shown in Figure 5.8. Similarly as with 1-Hz S_o shown previously, RD-SW reduces extreme loads on shaft and tower top significantly compared to `unctrl.fault`. However, at lower wind turbulence intensity the loads in `damp`er are still considerably higher than `normal`, while at higher turbulence intensities such difference is much lower.

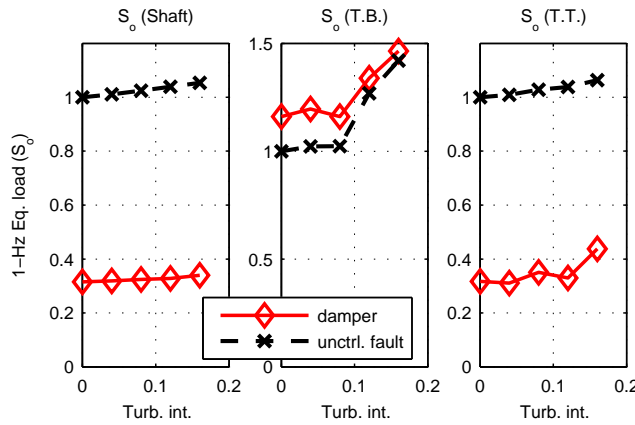
Maximum values of rotor and current voltages are shown in Figure 5.9, observe that in order to damp oscillations induced by the unbalanced fault the maximum magnitude of rotor voltage increases about 20% compared to that of `unctrl.fault` at very low turbulence intensities, and to about 10% at high turbulence intensities. On the other hand to maximum values of rotor current are decreased about 5% in `damp`er compared to `unctrl.fault`.

5.3.5.2 Load reduction with different control parameters

This section demonstrates the impact of increasing the gain H_1 of $C_q(s)$ on 1-Hz S_o , and on rotor voltage $|V_r|$, in order to ponder to what extent can loads be reduced within RSC voltage limits. Figure C.1 (C, 113) shows the DFAG design data, and the corresponding values of the control variable over the operational range, it can be seen that at rated power the voltage of the RSC is on the lower end of its magnitude, therefore there is margin to increase it in order to damp oscillations. Figure 5.10 shows rotor voltage magnitude $|V_r|$ versus 1-Hz S_o of shaft, tower bottom (T.B.) and tower top (T.T.) side-to-side moment for different values of the gain H_1 in RD-SW shown in Figure 3.15. Simulations are performed at rated wind speed with 10% turbulence intensity. It can be observed that is possible to reduce the loading on the shaft, and on T.T. while $|V_r|$ is further increased but yet within the values expected over the operating range as shown in Figure C.1. Furthermore loads on T.B. are slightly increased with increased control gain. Data shown in Figure 5.10 corresponds to $40 < H_1 < 200$.



(a) Comparison of **normal** and **damper**, values are normalized to **normal** at 0 turbulence intensity. From left to right shaft torsion, tower bottom (T.B.) and tower top (T.T.) side-to-side moment.



(b) Comparison of **damper** and **unctrl. fault**, values are normalized to **unctrl. fault** at 0 turbulence intensity. From left to right shaft torsion, tower bottom (T.B.) and tower top (T.T.) side-to-side moment.

Figure 5.7: Normalized 1-Hz equivalent loads vs. turbulence intensity.

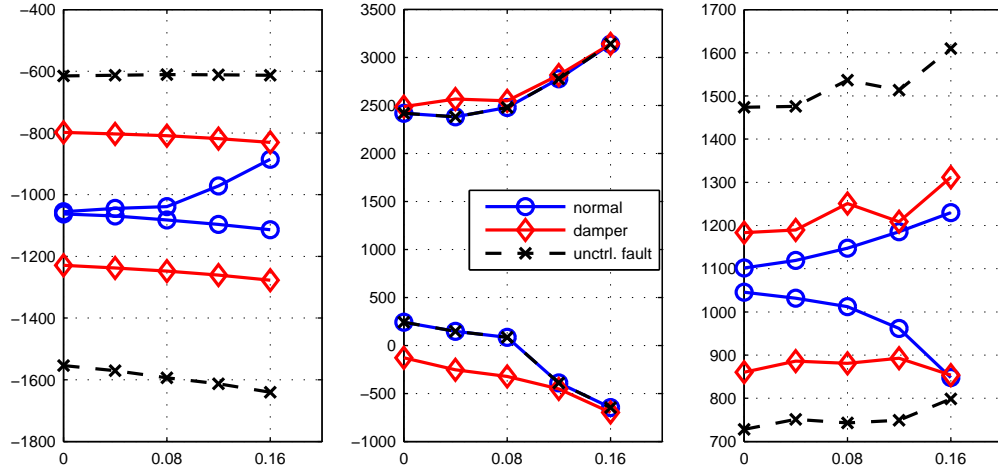


Figure 5.8: Comparison of extreme loads given different levels of turbulence intensity, from left to right shaft torsion, tower bottom (T.B.), and tower top (TP).

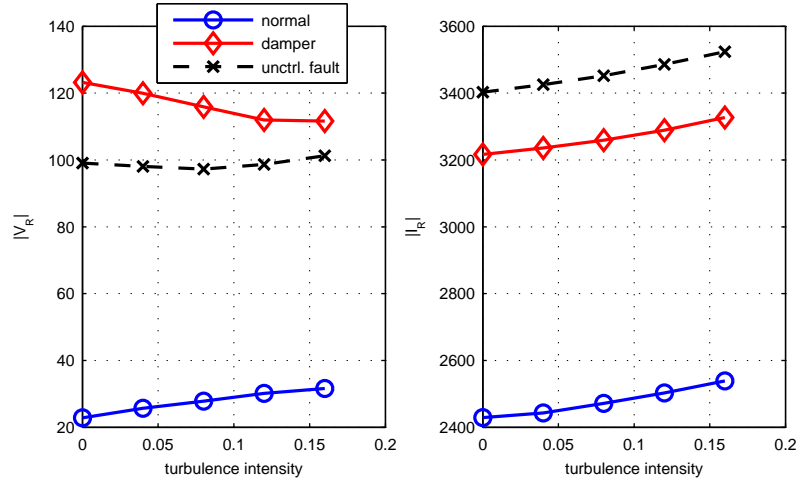


Figure 5.9: Comparison maximum values of rotor voltage (left), and current (right) magnitude given different levels of turbulence intensity

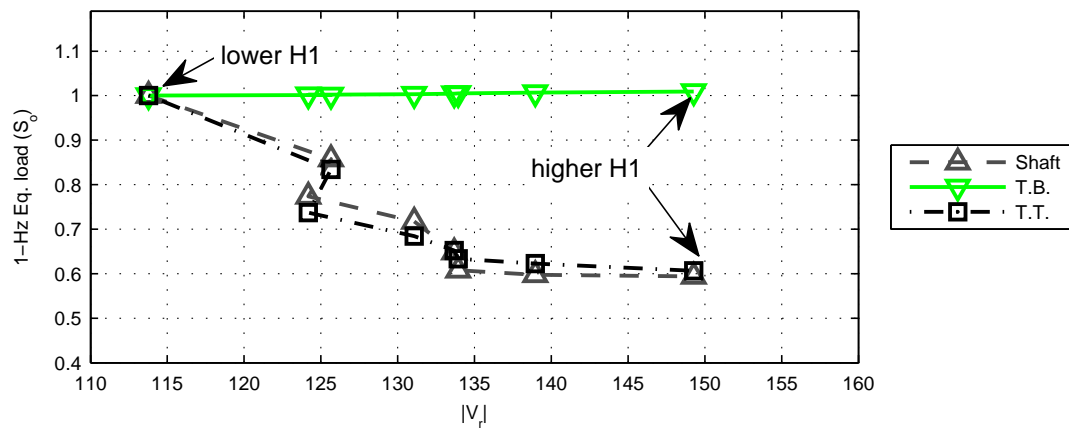


Figure 5.10: Rotor voltage magnitude vs. 1-Hz equivalent loads for different values of control gain H_1

5.4 Summary

Studies of the dynamic response of a DFAG wind turbine during balanced, and unbalanced voltage faults have been presented in this Chapter.

The studies of a balanced voltage fault showed that there is significant impact on some structural loads due to the sudden changes in the stator voltage imposed at the time the fault occurs, and the time the voltage is restored. The reconnection of the rotor side converter after the fault was also shown to have a significant impact on structural loads. The impact of wind gusts, wind turbulence, and voltage fault was qualitatively compared in electrical and structural variables.

The case of unbalanced voltage faults was also studied. A resonant damping control developed in Chapter 3 was applied to damp the torque oscillations induced by the unbalanced of stator voltages. These torque oscillations occur at twice the frequency of the supply voltage, and they are severe because the electrical mode of asynchronous machines is not very well damped as it was shown in Chapter 4. 1-Hz equivalent load were used to measure the impact of the fault and the reduction of structural loads.

Simulations with the integrated design environment showed that an unbalance voltage fault can have a severe impact, in terms of 1-Hz equivalent, loads on shaft torsion and tower top side-to-side moment. The resonant damping control was proven to reduce significantly shaft and tower top side-to-side loads during an unbalanced fault, while keeping reasonable voltage limits on the rotor side converter. However, even with a large load reduction, the loading imposed on structural loads is still many times larger than in normal operation. Therefore, it is relevant to consider whether this type of loading scenario has an impact on wind turbine components, particularly on gearboxes. Such investigations would involve models of the internal dynamics of gearboxes. Furthermore, it is important to consider that in the case of the loads on the tower, the estimations presented here may represent a worst case, since the standard drive train model transfers the generator torque directly onto the shaft and the tower top.

Conclusions

This Ph.D. study has demonstrated an integrated dynamic analysis environment with studies of the response and the control of wind turbines under specific power system conditions.

A simulation environment for integrated dynamic analysis has been developed. Electrical machine models and controls, and power system models have also been developed and coupled to aeroelastic models using this environment. *This integrated simulation tool and the models developed allow dynamic analysis of the impact of some power system conditions on wind turbine structural loads.* In general, this simulation approach is useful in the design and analysis of wind turbines, where is necessary to include electrical and control aspects.

Application examples of this integrated dynamic analysis environment showed some of the analysis possibilities of this approach. For example, to study the stability of a wind turbine design considering structural and electromechanical modes. In a case studied in this project, a fixed-speed wind turbine was analyzed, and it was shown that electromechanical modes and structural modes can couple in the low frequency range. Another application example developed was the analysis of semi variable-speed wind turbines providing inertial response to support the power system, in this case the integrated analysis approach was proven to facilitate the study of the impact on structural loads while also facilitating the evaluation of the contribution of a wind farm to power system frequency support. It was shown that inertial response control of wind turbines can support the power system, and the qualitative impact it has on wind turbine structural loads.

Furthermore, dynamic analyzes of the response of semi variable-speed wind turbines under voltage faults have demonstrated that power system conditions can have a significant impact on structural loads. Balanced and unbalanced voltage faults were studied, the significant impact that these power system disturbances have on structural loads suggest that they should be considered in the design basis of wind turbines.

Control concepts for reduction of the loads imposed by unbalanced voltage were developed, demonstrated, and quantified. The results showed that a large reduction of the loads imposed from an unbalanced voltage fault can be achieved. However these loads are still large and therefore further studies to consider the impact on drive train component are relevant.

Finally, future work in the area of integrated dynamic analysis may involve studies of mechanical and/or electrical aspects that are relevant for wind turbine components design. Such analysis can be undertaking developing of coupling models of gearboxes and bearing for example, or in the electrical side models of the thermal behavior of power converters.

Regarding the wind turbine design process a future step would be to develop the conceptual framework for integrated design that was described in this study. Namely, to test the interface as a work flow, then identify design tasks to prove it as an automated process.

Also wind turbine the design verification process according to standards could be undertaken with this integrated dynamic analysis environment in order to benchmark standard design load cases with load cases derived from power system conditions.

Publication list

Journal publications

- [A1] **B. Barahona**, Nicolaos A. Cutululis, Anca D. Hansen, Poul Sørensen, “Unbalanced voltage faults: the impact on structural loads of DFIG wind turbines,” submitted to *Wind Energy*, January 2012.
- [A2] **B. Barahona**, P. Sørensen, L. Christensen, T. Sørensen, and H. Nielsen, “Validation of the Standard Method for Assessing Flicker From Wind Turbines,” *IEEE Transactions on Energy Conversion*, vol. 26, pp. 373-378, 2010. DOI [10.1109/TEC.2010.2068299](https://doi.org/10.1109/TEC.2010.2068299).

Conference publications

- [B2] **B. Barahona**, C. Wessels, A. D. Hansen, and P. Sørensen, “Loads on DFIG wind turbines due to unbalanced voltage faults,” in *7th PhD Seminar on Wind Energy in Europe*, European Academy of Wind Energy (EAWWE), October 2011.
- [B3] **B. Barahona**, P. Sørensen, O. Anaya-Lara, and J. Tande, “Integrated analysis of DFIG drive-train and power electronics dynamics during electrical AC faults and wind disturbances,” in *EPE Joint Wind Energy and T&D Chapters Seminar*, European Power Electronics and Drives Association, May 2011.
- [B4] **B. Barahona**, “Integrated design and control of wind turbines.” Conference contribution - [Slide show presentation] Presented at *4th Wind Energy Systems Workshop*, 2010, Risø (DK), Status: unpublished, November 2010.
- [B5] **B. Barahona** and P. Sørensen, “Dynamic analysis of wind turbines from an integrated perspective,” in *6th PhD Seminar on Wind Energy*

in *Europe*, pp. 289-294, European Academy of Wind Energy (EAWWE), October 2010.

- [B6] **B. Barahona**, L. C. Henriksen, A. D. Hansen, N. A. Cutululis, and P. Sørensen, “Coupling of HAWC2 and Matlab: Towards an Integrated Simulation Platform,” in *European Wind Energy Conference and Exhibition*, April 2010.
- [B7] A. D. Hansen, N. A. Cutululis, **B. Barahona**, and H. Markou, “Impact of fault ride-through requirements on wind turbine structural loads,” in *European Wind Energy Conference and Exhibition*, April 2010.
- [B8] **B. Barahona**, P. B. Andersen, A. D. Hansen, N. A. Cutululis, and P. Sørensen, “Integrated Design of Wind Power Systems: MATLAB-HAWC2 Interface,” in *50th International Conference of Scandinavian Simulation Society (SIMS 50)*, October 2009.
- [B9] A. D. Hansen, N. A. C. P. Sørensen, and **B. Barahona**, “Integrated Design of Wind Power Systems: - DIGSILENT/MATLAB Dynamic Simulation,” in *50th International Conference of Scandinavian Simulation Society (SIMS 50)*, pp. 97-105, October 2009.
- [B10] A. D. Hansen, N. A. Cutululis, I. Florin, and **B. Barahona**, “Integrated electrical design of DFIG wind turbines for power system studies,” in *5th Nordic Wind Power Conference*, September 2009.

Reports

- [C11] M. Henriksen, R. S. Olsen, **B. Barahona**, I. Arana, J. Holbøll, and P. Sørensen, “Wind Turbine Electrical Components. Electrical and Non-electrical Environment,” Report of PSO-project 010087 EMC Wind, *Technical University of Denmark*, 2011.

Modeling of asynchronous generator

Some basic considerations about the three phase asynchronous machine are done before entering the description of the dynamic model. A detail description of the construction and components of the asynchronous machine, as well as the basic physical laws, are not attempted. For such description the reader may refer to [126–128].

The asynchronous machine can operate as a motor (below synchronous speed) or as a generator (above synchronous speed). It has a stator, and a rotor that house the corresponding stator, and rotor circuits (i.e. distributed windings). The stator is connected to a shaft which will drive a load in the case of a motor, or be driven by a turbine in the case of a generator. Considering the rotor circuit, there are two types of asynchronous machines: *squirrel cage* and *wound-rotor*. Such rotor types have some practical implications, the squirrel cage induction machine (SCIG) is more robust and economic while the wound rotor allows to connect the rotor circuit to a external circuit (i.e. doubly-fed asynchronous machine -DFAG) using brushes, and slips rings.

A.1 Basic concepts.

The basic underlying principle in electrical machines is that a *varying* magnetic field induces voltages, which in turn produce currents that generate an electromotive force (*emf*). The *emf* drives the shaft in the case of a motor.

In the case of a generator, power flows in the opposite direction, therefore the mechanical power input by the turbine to rotate the shaft will induce currents flowing from the generator stator towards the power system. The currents in the stator, and rotor circuit generate rotating magnetic fields in the air gap. The spatially varying magnetic field produced by the currents flowing in the stator circuits (**stator magnetic field**), varies sinusoidally at an *electrical* synchronous frequency ω_{se} (**electrical rad/s**) [127]

$$\omega_{se} = 2\pi f_s$$

where f_s (Hz) is the frequency of the stator voltages and currents, typically 50 Hz (Europe) or 60 Hz (Mexico). The synchronous frequency can be expressed as a *mechanical* synchronous frequency ω_{sm} in **rad/s** by considering the number of magnetic poles p_f (or the number of magnetic pole pairs $\frac{p_f}{2}$) that the machine has

$$\omega_{sm} = 2\pi f_s \left(\frac{2}{p_f} \right)$$

or in revolutions per minute (**rpm**) as

$$n_s = \omega_{sm} \left(\frac{60}{2\pi} \right) = \frac{120f_s}{p_f}$$

Similarly, position θ can also be expressed in terms of mechanical degrees θ_m or electrical degrees θ_e , which are related by Eq. A.1.

$$\theta_e = \frac{p_f}{2} \theta_m \quad (\text{A.1})$$

The **rotor magnetic field**, also rotates at synchronous speed [127]. The rotor itself must however, be rotating slightly faster (generator) or slower (motor) than the synchronous speed in order to produce power. The difference between the synchronous speed and the rotor speed is called slip (Eq. A.2).

$$s = \frac{n_s - n_r}{n_s} \quad (\text{A.2})$$

A.1.1 Symmetry.

The following assumptions about the symmetry of the machine are considered:

- symmetrical three phase circuits, and
- uniform air gap.

A.2 Steady-state model.

The model of the asynchronous machine in steady state can be derived from a line diagram [126], or by phasor analysis of the stator, and rotor voltages and currents [127]. Fig. A.1 is a graphic representation of one phase of rotor, and stator circuit, notice that the *air gap* is represented by an ideal transformer, and that the losses in the core are neglected (i.e. R_c is not considered in the parallel branch, only X_m).

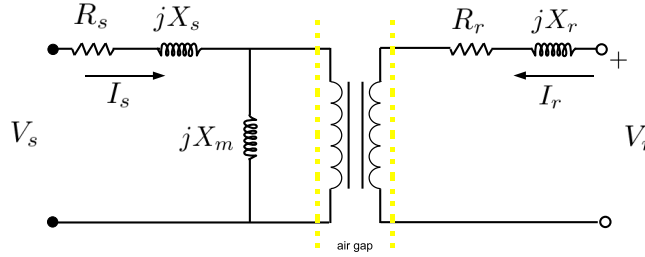


Figure A.1: Simplified diagram of asynchronous machine (the rotor voltage is $V_r = 0$ in an induction machine, and in the case of a doubly-fed machine it is supplied by a power converter).

An equivalent circuit can be derived by referring the rotor variables to the stator side, as shown in Fig. A.2. Applying Kirchhoff's laws the voltage equations for stator, and rotor circuit are derived. In Eq. A.3, the voltage equations of the equivalent circuit are expressed in matrix form, solving them with given voltages V_s , and V_r' yields stator, and rotor current (I_s , I_r') in steady state.¹

$$\begin{bmatrix} V_s \\ \frac{V_r'}{s} \end{bmatrix} = \begin{bmatrix} R_s + j(X_s + X_m) & jX_m \\ jX_m & \frac{R_r'}{s} + j(X_m + X_r') \end{bmatrix} \begin{bmatrix} I_s \\ I_r' \end{bmatrix} \quad (\text{A.3})$$

The apparent power at the stator terminals S_s , is then given by Eq. A.4. The apparent power across the air gap S_{ag} is the sum of winding losses (i.e. copper, and leakage) and mechanical power (i.e. $S_{ml} = S_l + P_{mech}$). The apparent power through the rotor circuit S_{rsc} -controlled by the rotor-side converter (RSC), goes also through the air gap. In the case of the asynchronous machine $S_{rsc} = 0$ in Eq. A.5, because the rotor is short-circuited

¹For steady-state calculations RMS values are used, power is calculated accordingly.

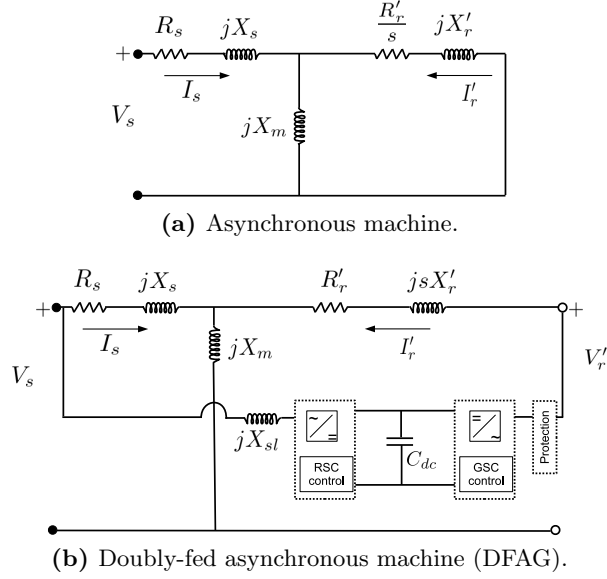


Figure A.2: Per-phase diagram of asynchronous generator (rotor quantities are referred to stator side).

(i.e. $V_r = 0$, Figure A.2a).

$$S_s = 3V_s I_s^* \quad (\text{A.4})$$

$$\begin{aligned} S_{ag} &= 3 \left(-S_{ml} + \frac{S_{rsc}}{s} \right) \\ &= 3 \left(- \left(\frac{R'_r}{s} + jX'_r \right) I'_r I_r'^* + \frac{V'_r I_r'^*}{s} \right) \end{aligned} \quad (\text{A.5})$$

The total apparent power S_{tot} exchanged with the grid by an asynchronous machine, is directly the stator apparent power: $S_{tot} = S_s$. However in the case of the DFAG, S_{tot} is given by Eq. A.6 (neglecting converter losses), where S_{gsc} is the apparent power exchanged by the grid-side power converter (GSC) with the grid. The real power exchanged by the rotor circuit $\text{Re}[S_{rsc}]$ is controlled by the RSC (see power flow diagram), therefore the real power injected by the GSC is $\text{Re}[S_{gsc}] = \text{Re}[S_{rsc}]$. The GSC controls the reactive power exchanged with the grid by the rotor circuit Q_{gsc} , and the voltage in the dc-bus that links RSC, and GSC.

$$\begin{aligned} S_{tot} &= S_s + S_{gsc} \\ &= S_s + \text{Re} [3V'_r I_r'^*] + Q_{gsc} \end{aligned} \quad (\text{A.6})$$

The power flow can be depicted as shown in Figure A.3, where the mechanical power P_{mech} , the power from the rotor circuit P_r , and the power losses due to the resistance of the circuits P_{cu} , are clearly identified.

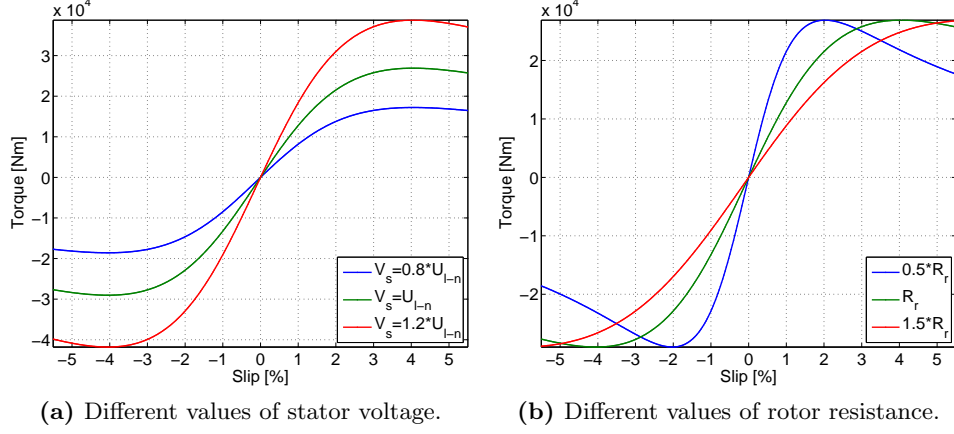


Figure A.4: Asynchronous machine steady-state torque.

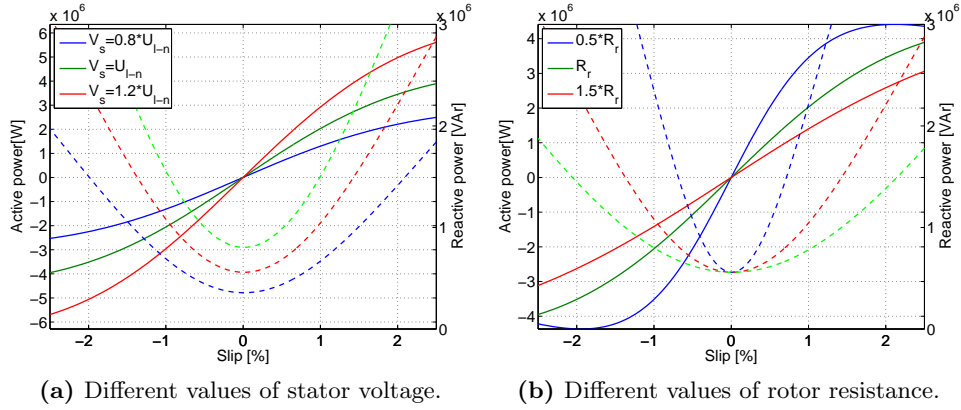


Figure A.5: Asynchronous machine steady-state active, and reactive power.

A.2.1.2 DFAG

The main advantages of using a DFAG in wind turbine is the possibility of operating with variable-speed, and the independent control of active, and reactive power. The torque characteristic of a DFAG depends on the same parameters, and variables as the asynchronous machine, plus it also depends on the control of the back-to-back converter that couples the rotor circuit to the stator circuit. Therefore the DFAG torque characteristic can be thought of as having another two degrees of freedom compared to that of the asynchronous machines (i.e. Figure A.4). Namely the magnitude, and angle of the rotor voltage $V_r = Ae^{j\theta}$, Figure A.6 illustrates the influence θ , and $|V_r|$ in the torque. Note that the limits to the operation of the converter, and the stator current are not considered. The influence of these, and other lim-

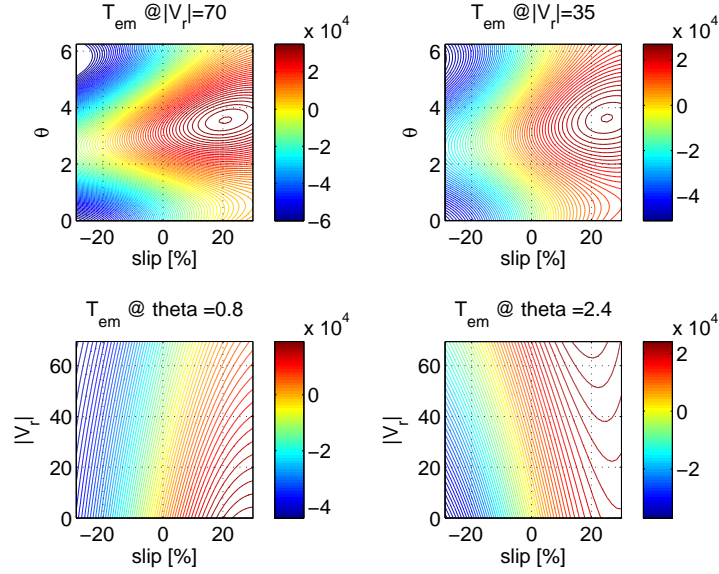


Figure A.6: Contour plots of DFAG torque (top $s-\theta$ for two values of $|V_r|$, bottom $s-|V_r|$ for two values of θ).

itations on the power capability of the machine are addressed in [129, 130].

Figure A.7 illustrates the space of operating points of power, and torque for different values of V_r (shown in the top-left plot) if the machine was running at nominal slip.

Table A.2: DFAG data ($p_f = 4$)

Nominal values			Stator			Rotor	
S_n	U_n	ω_n	R_s	X_s	X_m	R'_r	X'_r
2.21 MVA	0.690 kV	1600 rpm	0.0013	0.0238	1.0199	0.0215	0.0215

*resistances and reactances are in Ω

A.3 Dynamic model.

A dynamic model of an asynchronous generator was implemented in state space form [90, 127, 131]. The procedure followed is based on the vector method [131], and it resumes to expressing the voltage equations in a manner that makes it easier to solve them for the selected state variables (currents or flux linkages). Then the voltage equations are transformed to dq -frame, in order to eliminate the time varying inductances. This results in a system

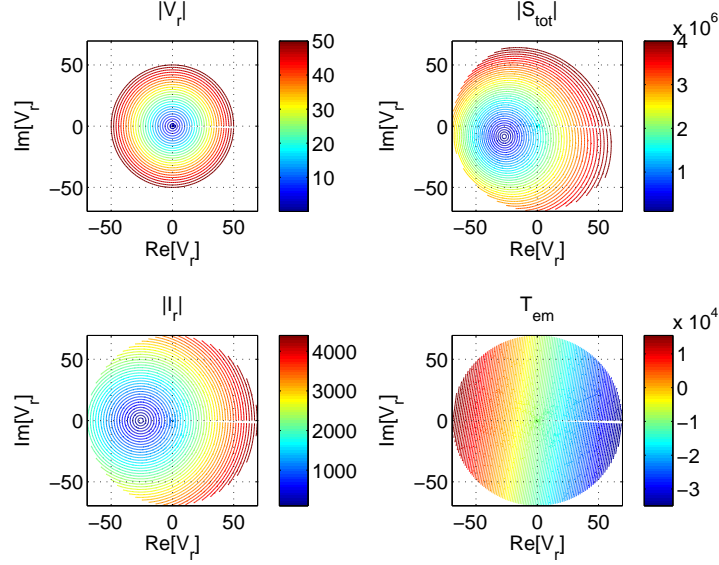


Figure A.7: Contour plots of DFAG $|S_{\text{tot}}|$, $|I_r|$, and T_{em} at nominal slip (top left the control variable V_r).

of first-order ordinary differential equations with constant coefficients.

A.3.1 Voltage equations.

Using the vector method [95, 131, 132], the voltage equations for the stator, and rotor circuit are given by Eq. A.11. The subindex abc indicates that the vectors are in an abc -frame, s indicates stator quantities, and r rotor quantities. Namely \mathbf{v}_{abcs} is a set of space-vectors (Figure A.8) that represents the time functions of the stator voltage in phase- a , $-b$, and $-c$. Similarly \mathbf{v}_{abcr} represents the rotor voltages. \mathbf{i} are space-vector sets of stator, and rotor currents as indicated by sub indexes. $\dot{\lambda}$ are flux linkages per second, again with sub indexes indicating abc -frame of stator, and rotor. \mathbf{r}_s and \mathbf{r}_r are diagonal matrices, with the elements of the diagonal being the resistance of winding in each phase of stator, and rotor (Eq. A.12).

$$\begin{aligned}\mathbf{v}_{abcs} &= \mathbf{r}_s \mathbf{i}_{abcs} + \dot{\lambda}_{abcs} \\ \mathbf{v}_{abcr} &= \mathbf{r}_r \mathbf{i}_{abcr} + \dot{\lambda}_{abcr}\end{aligned}\tag{A.11}$$

$$\begin{aligned}\mathbf{r}_s &= \text{diag} [R_s \quad R_s \quad R_s] \\ \mathbf{r}_r &= \text{diag} [R_r \quad R_r \quad R_r]\end{aligned}\tag{A.12}$$

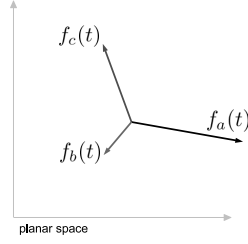


Figure A.8: Representation of functions of time as space-vectors in a planar space. Given a 3-phase balanced system (i.e. $f_a = \text{Re}[Ae^{j\omega t}]$, $f_b = \text{Re}[Ae^{j(\omega t - \frac{2\pi}{3})}]$, and $f_c = \text{Re}[Ae^{j(\omega t + \frac{2\pi}{3})}]$), the resultant of such vector set would be a vector with an amplitude A that rotates in space at an angular speed ω .

A.3.1.1 Referred voltage equations.

In order to derive an equivalent circuit such as figure A.3, that represents the magnetically coupled stator-rotor circuits, the variables of the rotor have to be changed to variables that are referred to the stator. Considering that the power flow should remain constant because the air gap is an ideal transformer, the variable change is done simply by multiplying rotor quantities by a ratio (or its square) of stator to rotor number of turns. Namely, referring rotor quantities to stator is done by multiplying impedance by $(\frac{N_s}{N_r})^2$, whereas voltages and fluxes are multiplied by $\frac{N_s}{N_r}$, and currents by $\frac{N_r}{N_s}$.

$$\begin{aligned} \mathbf{r}'_r &= \left(\frac{N_s}{N_r}\right)^2 \mathbf{r}_r \\ \{\mathbf{v}'_{abcr}, \boldsymbol{\lambda}'_{abcr}\} &= \frac{N_s}{N_r} \{\mathbf{v}_{abcr}, \boldsymbol{\lambda}_{abcr}\} \\ \mathbf{i}'_{abcr} &= \frac{N_r}{N_s} \mathbf{i}_{abcr} \end{aligned} \tag{A.13}$$

Therefore, the voltage equations of the magnetically coupled equivalent circuit are given by Eq. A.14. Note that this is generally the point of departure for modeling a given wind turbine generator, because data available is typically in the form of an equivalent circuit with rotor parameters referred to the stator.

$$\begin{aligned} \mathbf{v}_{abcs} &= \mathbf{r}_s \mathbf{i}_{abcs} + \dot{\boldsymbol{\lambda}}_{abcs} \\ \mathbf{v}'_{abcr} &= \mathbf{r}'_r \mathbf{i}'_{abcr} + \dot{\boldsymbol{\lambda}}'_{abcr} \end{aligned} \tag{A.14}$$

A.3.1.2 Inductance matrix.

Given the construction of the asynchronous generator, the magnetic flux seen by any of the 6 circuits depends on the magnetic flux generated by its own current, and by the currents in the other 5 circuits, this means that voltage equations (Eq. A.14) are coupled.

Considering magnetic linearity, flux linkage λ is equal to inductance L times current i ,

$$\lambda = Li \quad (\text{A.15})$$

therefore the matrix form of Eq. A.15 would yield a 6-by-6 inductance matrix with values outside the diagonal. Such inductance matrix to express flux linkages in terms of currents can be derived considering that

- stator and rotor circuits can be approximated as sinusoidally distributed circuits,
- the air gap is uniform,
- stator circuits are identical with number of turns N_s and resistance R_s ,
- rotor circuits are also identical with N_r and R_r ,
- the flux seen by one circuit is magnetically coupled to the fluxes from the rest of the circuits.

The inductance seen by a given circuit (i.e. phase- n) would then be composed of

1. self-inductance of stator L_s (or rotor L_r) including leakage as described by Eq. A.19,
2. stator-to-stator L_{ss} (or rotor-to-rotor L_{rr}) mutual inductances, and
3. stator-to-rotor (or rotor-to-stator) mutual inductances L_{sr}

The total flux linkage of a given circuit would be given by the sum of self-inductance times current of the circuit, plus mutual inductances times the corresponding currents of the other circuits. For example, the flux linkage λ_{as} of the stator phase- a (Eq. A.16), depends on the current of each circuit of the stator and of the rotor, multiplied by the corresponding inductances

$$\begin{aligned} \lambda_{as} = & L_s i_{as} + L_{ss} i_{bs} + L_{ss} i_{cs} + \dots \\ & \dots + L'_{sr} \cos(\theta_r) i'_{ar} + L'_{sr} \cos(\theta_r + \frac{2\pi}{3}) i'_{br} + L'_{sr} \cos(\theta_r - \frac{2\pi}{3}) i'_{cr} \end{aligned} \quad (\text{A.16})$$

where θ_r is the angle between the magnetic axis of rotor phase- a and stator phase- a . This gives a picture of the magnetic coupling of stator and rotor circuits. The matrix expression for the flux linkages is then given by Eq. A.17

$$\begin{bmatrix} \lambda_{abcs} \\ \lambda'_{abcr} \end{bmatrix} = \mathbf{L} \begin{bmatrix} \mathbf{i}_{abcs} \\ \mathbf{i}'_{abcr} \end{bmatrix} \quad (\text{A.17})$$

$$\begin{bmatrix} \lambda_{as} \\ \lambda_{bs} \\ \lambda_{cs} \\ \lambda'_{ar} \\ \lambda'_{br} \\ \lambda'_{cr} \end{bmatrix} = \begin{bmatrix} \mathbf{L}_s & \mathbf{L}'_{sr} \\ (\mathbf{L}'_{sr})^\top & \mathbf{L}'_r \end{bmatrix} \begin{bmatrix} i_{as} \\ i_{bs} \\ i_{cs} \\ i'_{ar} \\ i'_{br} \\ i'_{cr} \end{bmatrix}$$

where the inductance matrix is composed of the sub-matrices in Eq. A.18.

$$\mathbf{L}_s = \begin{bmatrix} L_s & L_{ss} & L_{ss} \\ L_{ss} & L_s & L_{ss} \\ L_{ss} & L_{ss} & L_s \end{bmatrix} \quad (\text{A.18})$$

$$\mathbf{L}'_r = \begin{bmatrix} L'_r & L'_{rr} & L'_{rr} \\ L'_{rr} & L'_r & L'_{rr} \\ L'_{rr} & L'_{rr} & L'_r \end{bmatrix}$$

$$\mathbf{L}'_{sr} = L'_{sr} \begin{bmatrix} \cos \theta_r & \cos(\theta_r + \frac{2\pi}{3}) & \cos(\theta_r - \frac{2\pi}{3}) \\ \cos(\theta_r - \frac{2\pi}{3}) & \cos \theta_r & \cos(\theta_r + \frac{2\pi}{3}) \\ \cos(\theta_r + \frac{2\pi}{3}) & \cos(\theta_r - \frac{2\pi}{3}) & \cos \theta_r \end{bmatrix}$$

Stator and rotor self-inductances are given by the sum of self-magnetizing inductance (L_{ms} , L'_{mr}), and leakage inductance (L_{ls} , L'_{lr}) as shown in Eq. A.19,

$$\begin{aligned} L_s &= L_{ms} + L_{ls} \\ L'_r &= L'_{mr} + L'_{lr} \end{aligned} \quad (\text{A.19})$$

stator-to-stator, and rotor-to-rotor mutual inductances are given by Eq. A.20.

$$\begin{aligned} L_{ss} &= -\frac{L_{ms}}{2} \\ L'_{rr} &= -\frac{L'_{mr}}{2} \end{aligned} \quad (\text{A.20})$$

A simpler expression of the sub-matrices in Eq. A.18 can be obtained resorting to the definition of inductance as a material property Eq. A.21, and to

the formula for transferring values from rotor to stator side Eq. A.13.

$$L_{ms} = \left(\frac{N_s}{2}\right)^2 \frac{\pi\mu_o r l}{g} \quad (\text{A.21})$$

$$L_{mr} = \left(\frac{N_r}{2}\right)^2 \frac{\pi\mu_o r l}{g}$$

$$L_{sr} = \left(\frac{N_s}{2}\right) \left(\frac{N_r}{2}\right) \left(\frac{\pi\mu_o r l}{g}\right) \quad (\text{A.22})$$

Referring the rotor self-magnetizing inductance L_{mr} , and the stator-rotor mutual inductance L_{sr} to the stator side yields Eq. A.23,

$$L'_{mr} = \left(\frac{N_s}{N_r}\right)^2 L_{mr} = L_{ms} \quad (\text{A.23})$$

$$L'_{sr} = \left(\frac{N_s}{N_r}\right)^2 L_{sr} = \frac{N_s}{N_r} L_{ms}$$

the inductance matrix can then be expressed as shown in Eq. A.24.

$$\mathbf{L} = \begin{bmatrix} L_{ms} + L_{ls} & -\frac{L_{ms}}{2} & -\frac{L_{ms}}{2} & & & \\ -\frac{L_{ms}}{2} & L_{ms} + L_{ls} & -\frac{L_{ms}}{2} & & & \\ -\frac{L_{ms}}{2} & -\frac{L_{ms}}{2} & L_{ms} + L_{ls} & & & \\ & & & \mathbf{L}'_{sr} & & \\ & & & & L_{ms} + L'_{lr} & -\frac{L_{ms}}{2} & -\frac{L_{ms}}{2} \\ & & & & -\frac{L_{ms}}{2} & L_{ms} + L'_{lr} & -\frac{L_{ms}}{2} \\ & & & & -\frac{L_{ms}}{2} & -\frac{L_{ms}}{2} & L_{ms} + L'_{lr} \\ & & & & & & & (\mathbf{L}'_{sr})^\top & & & \\ & & & & & & & & & & & \end{bmatrix} \quad (\text{A.24})$$

A.3.2 Selection of reference frame.

Given Eq. A.14, another change of variable is convenient in order to cancel time-varying inductances due to the relative motion of the circuits. The variables in abc circuits (i.e. voltages, currents, fluxes) can be transformed to variables in an arbitrary-fictitious set of circuits, normally called dq -reference frame. The transformation from abc to dq , is a case of poly-phase to orthogonal two-phase transformation, it is well described in the literature [76, 90, 127], and widely used for modeling of synchronous (i.e. Park's transform), and asynchronous machines.

The dq -transformation is given by Eq. A.25, where matrix \mathbf{K}_T maps a 3-phase system of vectors in a planar space \mathbf{f}_{abc} (i.e. Figure A.8), to a 2-phase system of vectors in the same plane \mathbf{f}_{dq} . The variables represented by these space-vectors are explicit functions of time such as voltage, current, flux or charge. Therefore when evaluating Eq. A.25 numerically, the quantities f_a ,

f_b , and f_c are instantaneous values of the corresponding functions. However, it is possible to formulate Eq. A.25 in terms of time-varying phasors.

$$\mathbf{f}_{dq} = \mathbf{K}_T \mathbf{f}_{abc} \quad (\text{A.25})$$

$$\begin{bmatrix} f_d \\ f_q \\ f_0 \end{bmatrix} = \mathbf{K}_T \begin{bmatrix} f_a \\ f_b \\ f_c \end{bmatrix}$$

Notice that a third component f_0 is added to the dq -system, this is simply to represent the transformation in symmetric matrix form. The value of this component is zero as long as the system is balanced.² Consider also the transformation matrix \mathbf{K}_T may be a function of time, depending on the circuit under analysis (i.e. static or rotating), and the reference frame selected (i.e. the angular speed of the frame). Given the appropriate choice of the transformation matrix \mathbf{K}_T , a stationary or a rotating circuit can be transformed to an arbitrary reference frame. The arbitrary reference frame may also be fixed or rotating. Eq. A.26-A.27 describe a general transformation matrix [90, 127] where θ_{ar} is the angular displacement of the arbitrary reference frame relative to some *fixed reference*, and θ_c is the angular displacement of the circuit frame relative to the same fixed reference [90].

$$\mathbf{K}_T = k \begin{bmatrix} \cos(\beta) & \cos(\beta - \frac{2\pi}{3}) & \cos(\beta + \frac{2\pi}{3}) \\ \sin \beta & \sin(\beta - \frac{2\pi}{3}) & \sin(\beta + \frac{2\pi}{3}) \\ \frac{1}{2} & \frac{1}{2} & \frac{1}{2} \end{bmatrix} \quad (\text{A.26})$$

$$\beta = \theta_{ar} - \theta_c \quad (\text{A.27})$$

In the case of a stationary circuit the angular speed is zero, namely $\dot{\theta}_c = 0$. Analogously, the speed $\dot{\theta}_{ar}$ defines the speed of the arbitrary reference frame. A static reference frame would yield $\dot{\theta}_{ar} = 0$, and a synchronously rotating frame $\dot{\theta}_{ar} = \omega_{se}$. Typically, the constant k is selected as $\frac{2}{3}$.

A.3.2.1 Voltage equations in arbitrary reference frame.

The voltage equations Eq. A.14 can be transformed to a dq -reference frame using Eq. A.25. Currents and flux linkages are the functions \mathbf{f}_{abc} , to be transformed. For stationary circuits, the transformation matrix may be denoted as $\mathbf{K}_s(\beta_s)$. An expression of the stator voltages in dq -reference frame, can be obtained as shown in Eq. A.28

$$\mathbf{K}_s^{-1} \mathbf{v}_{dqs} = \mathbf{r}_s \mathbf{K}_s^{-1} \mathbf{i}_{dqs} + \mathbf{K}_s^{-1} \dot{\lambda}_{dqs} + (\dot{\mathbf{K}}_s^{-1}) \lambda_{dqs} \quad (\text{A.28})$$

$$\mathbf{v}_{dqs} = \mathbf{K}_s \mathbf{r}_s \mathbf{K}_s^{-1} \mathbf{i}_{dqs} + \mathbf{K}_s \mathbf{K}_s^{-1} \dot{\lambda}_{dqs} + \mathbf{K}_s (\dot{\mathbf{K}}_s^{-1}) \lambda_{dqs}$$

²In the case of an 3-phase unbalanced system, it is necessary first to find the symmetrical components, and then transform them to 2-phase systems of positive, negative, and zero sequence.

where the resistance matrix \mathbf{r}_s is diagonal (Eq. A.12). Using matrix algebra and the algorithm described in B.1, Eq. A.28 can be simplified to Eq. A.29

$$\mathbf{v}_{dqs} = \mathbf{r}_s \mathbf{i}_{dqs} + \dot{\lambda}_{dqs} + \dot{\beta}_s \begin{bmatrix} 0 & 1 & 0 \\ -1 & 0 & 0 \\ 0 & 0 & 0 \end{bmatrix} \lambda_{dqs} \quad (\text{A.29})$$

where $\dot{\beta}_s$ is the time derivative of the relative angle between an arbitrary reference frame, and the stator circuit reference frame. From Eq. A.27 with θ_c constant, the relative angle speed is simply the speed of the arbitrary reference frame

$$\dot{\beta}_s = \dot{\theta}_{ar} \quad (\text{A.30})$$

Similarly, using $\mathbf{K}_r(\beta_r)$ the rotor voltages may be expressed by Eq. A.31

$$\mathbf{v}_{dqr} = \mathbf{r}_r \mathbf{i}_{dqr} + \dot{\lambda}_{dqr} + \dot{\beta}_r \begin{bmatrix} 0 & 1 & 0 \\ -1 & 0 & 0 \\ 0 & 0 & 0 \end{bmatrix} \lambda_{dqr} \quad (\text{A.31})$$

where

$$\dot{\beta}_r = \dot{\theta}_{ar} - \dot{\theta}_{re} \quad (\text{A.32})$$

Eq. A.29-A.31 are equivalent to the voltage equations Eq. A.14, in dq -reference frame. In order to solve these equations the relation between currents, and flux linkages Eq. A.17, should be taken into consideration. Using Eq. A.25 to transform currents, and fluxes linkages from abc - to dq -reference frame yields Eq. A.33,

$$\begin{bmatrix} \mathbf{K}_s^{-1} & \mathbf{0} \\ \mathbf{0} & \mathbf{K}_r^{-1} \end{bmatrix} \begin{bmatrix} \lambda_{dqs} \\ \lambda_{dqr} \end{bmatrix} = \mathbf{L} \begin{bmatrix} \mathbf{K}_s^{-1} & \mathbf{0} \\ \mathbf{0} & \mathbf{K}_r^{-1} \end{bmatrix} \begin{bmatrix} \mathbf{i}_{dqs} \\ \mathbf{i}_{dqr} \end{bmatrix} \quad (\text{A.33})$$

where the inductance matrix is that from Eq. A.24. Given Eq. A.33 fluxes may be expressed in terms of currents or vice versa, however the inductance matrix in abc -frame is time-dependent, and computationally expensive to invert. Therefore, let us express fluxes in terms of currents (Eq. A.34), thereby simplifying the inductance matrix that relates the two dependent variables [90],

$$\begin{aligned} \begin{bmatrix} \lambda_{dqs} \\ \lambda_{dqr} \end{bmatrix} &= \begin{bmatrix} \mathbf{K}_s & \mathbf{0} \\ \mathbf{0} & \mathbf{K}_r \end{bmatrix} \mathbf{L} \begin{bmatrix} \mathbf{K}_s^{-1} & \mathbf{0} \\ \mathbf{0} & \mathbf{K}_r^{-1} \end{bmatrix} \begin{bmatrix} \mathbf{i}_{dqs} \\ \mathbf{i}_{dqr} \end{bmatrix} \\ &= \begin{bmatrix} \mathbf{K}_s \mathbf{L}_s (\mathbf{K}_s)^{-1} & \mathbf{K}_s \mathbf{L}'_{sr} (\mathbf{K}_r)^{-1} \\ \mathbf{K}_r (\mathbf{L}'_{sr})^\top (\mathbf{K}_s)^{-1} & \mathbf{K}_r \mathbf{L}_r (\mathbf{K}_r)^{-1} \end{bmatrix} \begin{bmatrix} \mathbf{i}_{dqs} \\ \mathbf{i}_{dqr} \end{bmatrix} \\ &= \mathbf{L}_{dq} \begin{bmatrix} \mathbf{i}_{dqs} \\ \mathbf{i}_{dqr} \end{bmatrix} \end{aligned} \quad (\text{A.34})$$

where the inductance matrix in arbitrary dq -frame is given by Eq. A.35.

$$\mathbf{L}_{dq} = \begin{bmatrix} \frac{3}{2}L_{ms} + L_{ls} & 0 & 0 & \frac{3}{2}L_{ms} & 0 & 0 \\ 0 & \frac{3}{2}L_{ms} + L_{ls} & 0 & 0 & \frac{3}{2}L_{ms} & 0 \\ 0 & 0 & L_{ls} & 0 & 0 & 0 \\ \frac{3}{2}L_{ms} & 0 & 0 & \frac{3}{2}L_{ms} + L'_{lr} & 0 & 0 \\ 0 & \frac{3}{2}L_{ms} & 0 & 0 & \frac{3}{2}L_{ms} + L'_{lr} & 0 \\ 0 & 0 & 0 & 0 & 0 & L'_{lr} \end{bmatrix} \quad (\text{A.35})$$

Note that the inductance matrix becomes time-independent, and that there is only coupling between stator and rotor circuits in the same axis. The inductance matrix in arbitrary dq -frame can be further simplified [127], by defining the magnetizing inductance \mathcal{L}_m , and self-inductances (\mathcal{L}_r , \mathcal{L}_s), on the stator side in dq -frame as indicated by Eq. A.36, the inductance matrix in arbitrary dq -frame becomes Eq. A.37.

$$\begin{aligned} \mathcal{L}_m &= \frac{3}{2}L_{ms} \\ \mathcal{L}_s &= \mathcal{L}_m + L_{ls} \\ \mathcal{L}_r &= \mathcal{L}_m + L'_{lr} \end{aligned} \quad (\text{A.36})$$

$$\mathbf{L}_{dq} = \begin{bmatrix} \mathcal{L}_s & 0 & 0 & \mathcal{L}_m & 0 & 0 \\ 0 & \mathcal{L}_s & 0 & 0 & \mathcal{L}_m & 0 \\ 0 & 0 & L_{ls} & 0 & 0 & 0 \\ \mathcal{L}_m & 0 & 0 & \mathcal{L}_r & 0 & 0 \\ 0 & \mathcal{L}_m & 0 & 0 & \mathcal{L}_r & 0 \\ 0 & 0 & 0 & 0 & 0 & L'_{lr} \end{bmatrix} \quad (\text{A.37})$$

The inverse of the dq -inductance matrix yields Eq. A.38.

$$\mathbf{L}_{dq}^{-1} = \frac{1}{\mathcal{L}_s\mathcal{L}_r - \mathcal{L}_m^2} \begin{bmatrix} \mathcal{L}_r & 0 & 0 & -\mathcal{L}_m & 0 & 0 \\ 0 & \mathcal{L}_r & 0 & 0 & -\mathcal{L}_m & 0 \\ 0 & 0 & \frac{\mathcal{L}_s\mathcal{L}_r - \mathcal{L}_m^2}{L_{ls}} & 0 & 0 & 0 \\ -\mathcal{L}_m & 0 & 0 & \mathcal{L}_s & 0 & 0 \\ 0 & -\mathcal{L}_m & 0 & 0 & \mathcal{L}_s & 0 \\ 0 & 0 & 0 & 0 & 0 & \frac{\mathcal{L}_s\mathcal{L}_r - \mathcal{L}_m^2}{L'_{lr}} \end{bmatrix} \quad (\text{A.38})$$

The voltage equations in terms of flux linkages can be written as Eq. A.39,

$$\begin{aligned} \begin{bmatrix} \mathbf{v}_{dqs} \\ \mathbf{v}_{dqr} \end{bmatrix} &= \begin{bmatrix} \mathbf{r}_s & \mathbf{0} \\ \mathbf{0} & \mathbf{r}_r \end{bmatrix} \mathbf{L}_{dq}^{-1} \begin{bmatrix} \boldsymbol{\lambda}_{dqs} \\ \boldsymbol{\lambda}_{dqr} \end{bmatrix} + \begin{bmatrix} \dot{\boldsymbol{\lambda}}_{dqs} \\ \dot{\boldsymbol{\lambda}}_{dqr} \end{bmatrix} + \left(\begin{bmatrix} 0 & \dot{\beta}_s & 0 \\ -\dot{\beta}_s & 0 & 0 \\ 0 & 0 & 0 \end{bmatrix} \oplus \begin{bmatrix} 0 & \dot{\beta}_r & 0 \\ -\dot{\beta}_r & 0 & 0 \\ 0 & 0 & 0 \end{bmatrix} \right) \begin{bmatrix} \boldsymbol{\lambda}_{dqs} \\ \boldsymbol{\lambda}_{dqr} \end{bmatrix} \\ &= \mathbf{R}\mathbf{L}_{dq}^{-1} \begin{bmatrix} \boldsymbol{\lambda}_{dqs} \\ \boldsymbol{\lambda}_{dqr} \end{bmatrix} + \begin{bmatrix} \dot{\boldsymbol{\lambda}}_{dqs} \\ \dot{\boldsymbol{\lambda}}_{dqr} \end{bmatrix} + \boldsymbol{\Omega} \begin{bmatrix} \boldsymbol{\lambda}_{dqs} \\ \boldsymbol{\lambda}_{dqr} \end{bmatrix} \end{aligned} \quad (\text{A.39})$$

and in terms of currents as Eq. A.40

$$\begin{bmatrix} \mathbf{v}_{dqs} \\ \mathbf{v}_{dqr} \end{bmatrix} = \mathbf{R} \begin{bmatrix} \mathbf{i}_{dqs} \\ \mathbf{i}_{dqr} \end{bmatrix} + \mathbf{L}_{dq} \begin{bmatrix} \dot{\mathbf{i}}_{dqs} \\ \dot{\mathbf{i}}_{dqr} \end{bmatrix} + \boldsymbol{\Omega} \mathbf{L}_{dq} \begin{bmatrix} \mathbf{i}_{dqs} \\ \mathbf{i}_{dqr} \end{bmatrix} \quad (\text{A.40})$$

with matrices \mathbf{L}_{dq} (Eq. A.37) and $\boldsymbol{\Omega} \mathbf{L}_{dq}$ (Eq. A.41) cross-coupling stator-rotor d - q quantities.

$$\boldsymbol{\Omega} \mathbf{L}_{dq} = \begin{bmatrix} 0 & \dot{\beta}_s \mathcal{L}_s & 0 & 0 & \dot{\beta}_s \mathcal{L}_m & 0 \\ -\dot{\beta}_s \mathcal{L}_s & 0 & 0 & -\dot{\beta}_s \mathcal{L}_m & 0 & 0 \\ 0 & 0 & 0 & 0 & 0 & 0 \\ 0 & \dot{\beta}_r \mathcal{L}_m & 0 & 0 & \dot{\beta}_r \mathcal{L}_r & 0 \\ -\dot{\beta}_r \mathcal{L}_m & 0 & 0 & -\dot{\beta}_r \mathcal{L}_r & 0 & 0 \\ 0 & 0 & 0 & 0 & 0 & 0 \end{bmatrix} \quad (\text{A.41})$$

A.3.3 state space model.

Given the voltage equations in terms of flux linkages Eq. A.39, or in terms of currents Eq. A.40, a state space model of the asynchronous machine can be formulated relatively straight forward [90, 127]. A variable that represents energy storage should be chosen as the state variable, fluxes or currents are normally chosen. Using the voltage equations in terms of flux linkages, and selecting flux linkages as state variables, yields the following state space description of the generator dynamics Eq. A.42

$$\begin{bmatrix} \dot{\lambda}_{dqs} \\ \dot{\lambda}_{dqr} \end{bmatrix} = \mathcal{M} \begin{bmatrix} \lambda_{dqs} \\ \lambda_{dqr} \end{bmatrix} + \begin{bmatrix} \mathbf{v}_{dqs} \\ \mathbf{v}_{dqr} \end{bmatrix} \quad (\text{A.42})$$

where

$$\begin{aligned} \mathcal{M} &= - \left(\mathbf{R} \mathbf{L}_{dq}^{-1} + \boldsymbol{\Omega} \right) \\ &= \begin{bmatrix} \frac{R_s \mathcal{L}_r}{\mathcal{D}} & -\dot{\beta}_s & 0 & \frac{-R_s \mathcal{L}_m}{\mathcal{D}} & 0 & 0 \\ \dot{\beta}_s & \frac{R_s \mathcal{L}_r}{\mathcal{D}} & 0 & 0 & \frac{-R_s \mathcal{L}_m}{\mathcal{D}} & 0 \\ 0 & 0 & -\frac{R_s}{L_{ls}} & 0 & 0 & 0 \\ \frac{-R_r \mathcal{L}_m}{\mathcal{D}} & 0 & 0 & \frac{R_r \mathcal{L}_s}{\mathcal{D}} & -\dot{\beta}_r & 0 \\ 0 & \frac{-R_r \mathcal{L}_m}{\mathcal{D}} & 0 & \dot{\beta}_r & \frac{R_r \mathcal{L}_s}{\mathcal{D}} & 0 \\ 0 & 0 & 0 & 0 & 0 & -\frac{R_r}{L_{lr}} \end{bmatrix} \end{aligned} \quad (\text{A.43})$$

with

$$\mathcal{D} = \mathcal{L}_m^2 - \mathcal{L}_s \mathcal{L}_r \quad (\text{A.44})$$

A.3.3.1 Reduced order dynamic model.

The reduced order model consists in neglecting the stator fluxes transients. Therefore it includes only the states corresponding to the rotor fluxes in dq -frame, and the stator fluxes are solved with algebraic equations. In order to reduce the full order model in Eq. A.42, the derivatives of the stator flux linkages are set to zero as in Eq. A.45,

$$\begin{aligned} \begin{bmatrix} \mathbf{0} \\ \dot{\lambda}_{dqr} \end{bmatrix} &= \mathcal{M} \begin{bmatrix} \lambda_{dqs} \\ \lambda_{dqr} \end{bmatrix} + \begin{bmatrix} \mathbf{v}_{dqs} \\ \mathbf{v}_{dqr} \end{bmatrix} \\ &= \begin{bmatrix} \mathcal{M}_{ss} & \mathcal{M}_{sr} \\ \mathcal{M}_{rs} & \mathcal{M}_{rr} \end{bmatrix} \begin{bmatrix} \lambda_{dqs} \\ \lambda_{dqr} \end{bmatrix} + \begin{bmatrix} \mathbf{v}_{dqs} \\ \mathbf{v}_{dqr} \end{bmatrix} \end{aligned} \quad (\text{A.45})$$

the algebraic equations for the flux linkages of stator are then expressed by Eq. A.46,

$$\begin{aligned} \lambda_{dqs} &= -\mathcal{M}_{ss}^{-1} (\mathcal{M}_{sr} \lambda_{dqr} + \mathbf{v}_{dqs}) \\ &= \frac{1}{a^2 + 1} \left(\frac{\mathcal{L}_m}{\mathcal{L}_r} \begin{bmatrix} 1 & a & 0 \\ -a & 1 & 0 \\ 0 & 0 & 0 \end{bmatrix} \begin{bmatrix} \lambda_{dr} \\ \lambda_{qr} \\ \lambda_{0r} \end{bmatrix} + b \begin{bmatrix} -1 & -a & 0 \\ a & -1 & 0 \\ 0 & 0 & \frac{(a^2+1)}{b} \frac{L_{ls}}{R_s} \end{bmatrix} \begin{bmatrix} v_{ds} \\ v_{qs} \\ v_{0s} \end{bmatrix} \right) \end{aligned} \quad (\text{A.46})$$

where

$$\begin{aligned} a &= \dot{\beta}_s b \\ b &= \frac{\mathcal{D}}{R_s \mathcal{L}_r} \end{aligned} \quad (\text{A.47})$$

The reduced order state space model that represents the dynamics of the rotor fluxes is given in Eq. A.48,

$$\begin{aligned} \dot{\lambda}_{dqr} &= \mathcal{M}_{rs} \lambda_{dqs} + \mathcal{M}_{rr} \lambda_{dqr} + \mathbf{v}_{dqr} \\ &= -\mathcal{M}_{rs} (\mathcal{M}_{ss}^{-1} (\mathcal{M}_{sr} \lambda_{dqr} + \mathbf{v}_{dqs})) + \mathcal{M}_{rr} \lambda_{dqr} + \mathbf{v}_{dqr} \\ &= (\mathcal{M}_{rr} - \mathcal{M}_{rs} \mathcal{M}_{ss}^{-1} \mathcal{M}_{sr}) \lambda_{dqr} + \mathbf{v}_{dqr} - \mathcal{M}_{rs} \mathcal{M}_{ss}^{-1} \mathbf{v}_{dqs} \\ &= (\mathcal{M}_{rr} - \mathcal{M}_{rs} \mathcal{M}_{ss}^{-1} \mathcal{M}_{sr}) \lambda_{dqr} + [\mathbf{I}_{3 \times 3} \quad -\mathcal{M}_{rs} \mathcal{M}_{ss}^{-1}] \begin{bmatrix} \mathbf{v}_{dqr} \\ \mathbf{v}_{dqs} \end{bmatrix} \\ &= \begin{bmatrix} c & -d & 0 \\ d & c & 0 \\ 0 & 0 & \frac{-R_s}{L'_{lr}} \end{bmatrix} \lambda_{dqr} + \begin{bmatrix} 1 & 0 & 0 & \frac{bg}{a^2+1} & \frac{abg}{a^2+1} & 0 \\ 0 & 1 & 0 & -\frac{abg}{a^2+1} & \frac{bg}{a^2+1} & 0 \\ 0 & 0 & 1 & 0 & 0 & 0 \end{bmatrix} \begin{bmatrix} \mathbf{v}_{dqr} \\ \mathbf{v}_{dqs} \end{bmatrix} \end{aligned} \quad (\text{A.48})$$

where

$$\begin{aligned} c &= \frac{R_r \mathcal{L}_s}{\mathcal{D}} - g \frac{\mathcal{L}_m}{\mathcal{L}_r} \frac{1}{a^2 + 1} \\ d &= \dot{\beta}_r + g \frac{\mathcal{L}_m}{\mathcal{L}_r} \frac{a}{a^2 + 1} \\ g &= \frac{R_r \mathcal{L}_m}{\mathcal{D}} \end{aligned} \quad (\text{A.49})$$

A.3.3.2 Comparison of steady-state values.

For the sake of verification the steady-state values of the torque calculated with the steady-state model, and those calculated with the dynamic model were compared. The expression for the electromagnetic torque from the dynamic model is derived using the basic relationship of power to torque Eq. A.10, and the definition of electrical power as voltage time current [90, 127]. Using the voltage equations of the dynamic model the electromagnetic torque can be expressed solely in terms of flux linkages as Eq. A.50.

$$T_{em} = \frac{3}{2} \frac{p_f}{2} \frac{\mathcal{L}_m}{\mathcal{D}} (\lambda_{qs} \lambda'_{dr} - \lambda_{ds} \lambda'_{qr}) \quad (\text{A.50})$$

Figure A.9 shows the comparison of electromagnetic torque steady-state values calculated with the steady-state model, and those calculated with the full order (Eq. A.42), and the reduced order dynamic model (Eq. A.48). As expected the results of the different models are identical to each other.

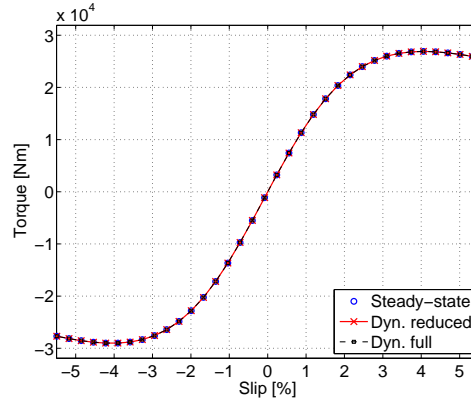


Figure A.9: Torque characteristic

A.3.4 Dynamic response of asynchronous machine.

In this section, the state space model of the magnetic fluxes is coupled to the equation of conservation of motion to observe the dynamic response of the system. The state space model Eq. A.42 can be simplified for the case of balanced input voltages. Because the zero components of state variables and inputs are always zero for the balanced case. Therefore, the full order

state space model can be expressed as in Eq. A.51.

$$\begin{bmatrix} \dot{\lambda}_{ds} \\ \dot{\lambda}_{qs} \\ \dot{\lambda}'_{dr} \\ \dot{\lambda}'_{qr} \end{bmatrix} = \begin{bmatrix} \frac{R_s \mathcal{L}_r}{\mathcal{D}} & -\dot{\beta}_s & \frac{-R_s \mathcal{L}_m}{\mathcal{D}} & 0 \\ \frac{R_s \mathcal{L}_r}{\mathcal{D}} & \dot{\beta}_s & 0 & \frac{-R_s \mathcal{L}_m}{\mathcal{D}} \\ \frac{-R_r \mathcal{L}_m}{\mathcal{D}} & 0 & \frac{R_r \mathcal{L}_s}{\mathcal{D}} & -\dot{\beta}_r \\ 0 & \frac{-R_r \mathcal{L}_m}{\mathcal{D}} & \frac{R_r \mathcal{L}_s}{\mathcal{D}} & \dot{\beta}_r \end{bmatrix} \begin{bmatrix} \lambda_{ds} \\ \lambda_{qs} \\ \lambda'_{dr} \\ \lambda'_{qr} \end{bmatrix} + \begin{bmatrix} v_{ds} \\ v_{qs} \\ v'_{dr} \\ v'_{qr} \end{bmatrix} \quad (\text{A.51})$$

Using the definition of electromagnetic torque Eq. A.50, and the equation of conservation of angular motion Eq. A.52

$$T_{em} - T_L = J \dot{\omega}_{rm} \quad (\text{A.52})$$

the change in generator rotor speed $\dot{\omega}_{rm}$ in terms of the states variables of Eq. A.51 yields Eq. A.53.

$$\dot{\omega}_{rm} = \frac{1}{J} \frac{3}{2} \frac{p_f}{2} \frac{\mathcal{L}_m}{\mathcal{D}} (\lambda_{qs} \lambda'_{dr} - \lambda_{ds} \lambda'_{qr}) - \frac{1}{J} T_L \quad (\text{A.53})$$

The linear system in Eq. A.51, and Eq. A.53 couple the fluxes with the rotor speed. The rotor speed ω_{rm} (rad/s) depends (non-linearly) on the fluxes, and the load torque (Eq. A.53), while the rotor speed ω_{re} (elec. rad/s) drives the cross coupling between λ'_{qr} (λ'_{dr}), and λ_{ds} (λ_{qs}) in Eq. A.51. Recall that the speed of the rotor reference frame is $\dot{\beta}_r = \omega_{ar} - \omega_{re}$ (Eq. A.32), and that the speed of the rotor field is related to the mechanical speed of the generator rotor by the number of magnetic pole pairs $\omega_{re} = \frac{p_f}{2} \omega_{rm}$ (Eq. A.1). The resulting nonlinear system takes the general form $\dot{\mathbf{x}} = \mathbf{f}(t, \mathbf{x}(t), \mathbf{u}(t))$, where the state derivatives $\dot{\mathbf{x}}$ are functions of states $\mathbf{x}(t)$, and inputs $\mathbf{u}(t)$. Arranging this system in matrix form as shown in Eq. A.3.4, where the vector of states and vector of inputs are kept in the same order, gives a clear picture of the nonlinearities. The entries in the *system* matrix of Eq. A.3.4 that are marked in black are those that are functions of time, namely the states corresponding to rotor flux linkages and rotor speed in this case.

$$\begin{bmatrix} \dot{\lambda}_{ds} \\ \dot{\lambda}_{qs} \\ \dot{\lambda}'_{dr} \\ \dot{\lambda}'_{qr} \\ \dot{\omega}_{re} \end{bmatrix} = \begin{bmatrix} \frac{R_s \mathcal{L}_r}{\mathcal{D}} & -\dot{\theta}_{ar} & \frac{-R_s \mathcal{L}_m}{\mathcal{D}} & 0 & 0 \\ \frac{R_s \mathcal{L}_r}{\mathcal{D}} & \dot{\theta}_{ar} & 0 & \frac{-R_s \mathcal{L}_m}{\mathcal{D}} & 0 \\ \frac{-R_r \mathcal{L}_m}{\mathcal{D}} & 0 & \frac{R_r \mathcal{L}_s}{\mathcal{D}} & \omega_{re} - \dot{\theta}_{ar} & 0 \\ 0 & \frac{-R_r \mathcal{L}_m}{\mathcal{D}} & \dot{\theta}_{ar} - \omega_{re} & \frac{R_r \mathcal{L}_s}{\mathcal{D}} & 0 \\ -A \lambda'_{qr} & A \lambda'_{dr} & 0 & 0 & 0 \end{bmatrix} \begin{bmatrix} \lambda_{ds} \\ \lambda_{qs} \\ \lambda'_{dr} \\ \lambda'_{qr} \\ \omega_{re} \end{bmatrix} + \begin{bmatrix} v_{ds} \\ v_{qs} \\ v'_{dr} \\ v'_{qr} \\ -\frac{p_f}{2J} T_L \end{bmatrix} \quad (\text{A.54})$$

with $A = \frac{3p_f^2 \mathcal{L}_m}{8J\mathcal{D}}$

A.3.4.1 Transient response.

The response of the asynchronous machine to a step of the load torque is shown in Figure A.10. Electromagnetic torque and generator rotor speed

are shown in Figure A.10a. Torque-speed phase plane is shown in Figure A.10b, where steady-state operation points are plotted with blue circles and the transient response from one steady-state point to another, and back is plotted with dashed line. These responses are similar to those found in the literature.

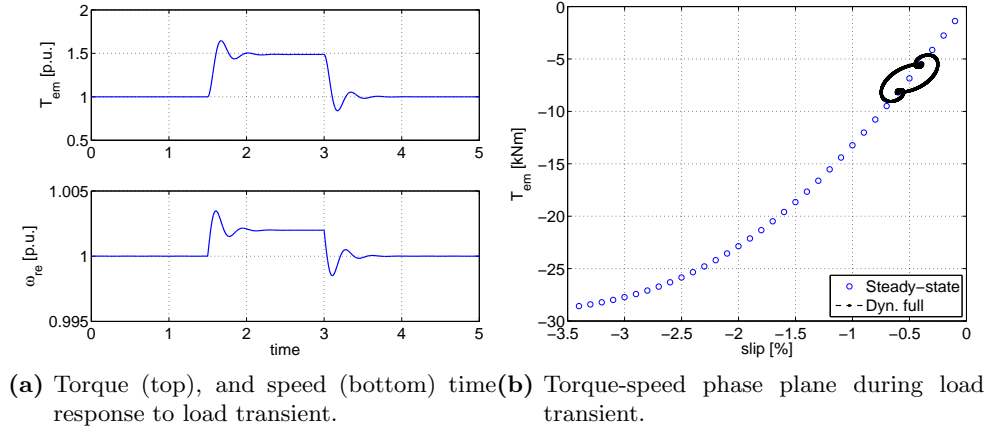


Figure A.10: Transient response of asynchronous machine

A.3.4.2 Linearized model.

Linear models are commonly used to design controls, or to study the stability around specific operating states. For example, the dynamic response of asynchronous machines to low frequency perturbations with different models shows that the performance of a model in comparison to measurements depends on the type of induction machine [133]. Namely, high slip machines, and machines with low stator resistance-to-leakage reactance ratio are well represented by reduced-order models. Furthermore, according to [133] a first-order model can reproduce machine response to perturbation up to 1 Hz, second-order models can predict the response to perturbation up to 3 Hz, and full order models to perturbations up to 10 Hz. Regarding aeroelastic simulations of wind turbines, [71] stated that an electrical generator mode at around 4.45 Hz, may couple to a combination of third flapwise bending mode of blades and second lateral bending mode of tower. In [134] a DFAG model is linearized with Matlab Control toolbox to show that the deep bar effect influences the damping of rotor fluxes in large DAFGs. Namely, the real part of the rotor flux eigen value is smaller when the deep-bar effect is not considered. In [90], an asynchronous machine model where currents are state variables is linearized, typical eigen values of induction motors are shown.

In this case linearization of the system in Eq. A.3.4 around a given operation point (ω_{re}^o), yields the linear system in Eq. A.55. The eigen values of the system matrix in Eq. A.55 at different operating points (i.e. given by λ_{ds}^o , λ_{qs}^o , λ_{dr}^o , λ_{qr}^o , and ω_{re}^o) are the natural frequencies corresponding to the state variables of the system.

$$\begin{bmatrix} \Delta \dot{\lambda}_{ds} \\ \Delta \dot{\lambda}_{qs} \\ \Delta \dot{\lambda}'_{dr} \\ \Delta \dot{\lambda}'_{qr} \\ \Delta \dot{\omega}_{re} \end{bmatrix} = \begin{bmatrix} \frac{R_s \mathcal{L}_r}{\mathcal{D}} & -\dot{\theta}_{ar} & \frac{-R_s \mathcal{L}_m}{\mathcal{D}} & 0 & 0 \\ \dot{\theta}_{ar} & \frac{R_s \mathcal{L}_r}{\mathcal{D}} & 0 & \frac{-R_s \mathcal{L}_m}{\mathcal{D}} & 0 \\ \frac{-R_r \mathcal{L}_m}{\mathcal{D}} & 0 & \frac{R_r \mathcal{L}_s}{\mathcal{D}} & \omega_{re}^o - \dot{\theta}_{ar} & \lambda_{qr}^o \\ 0 & \frac{-R_r \mathcal{L}_m}{\mathcal{D}} & \dot{\theta}_{ar} - \omega_{re}^o & \frac{R_r \mathcal{L}_s}{\mathcal{D}} & \lambda_{dr}^o \\ -A\lambda_{qr}^o & A\lambda_{dr}^o & A\lambda_{qs}^o & -A\lambda_{ds}^o & 0 \end{bmatrix} \begin{bmatrix} \Delta \lambda_{ds} \\ \Delta \lambda_{qs} \\ \Delta \lambda'_{dr} \\ \Delta \lambda'_{qr} \\ \Delta \omega_{re} \end{bmatrix} + \begin{bmatrix} \Delta v_{ds} \\ \Delta v_{qs} \\ \Delta v'_{dr} \\ \Delta v'_{qr} \\ -\frac{p_f}{2J} \Delta T_L \end{bmatrix} \quad (\text{A.55})$$

Figure A.11 shows a map of eigen values of (1) stator flux (dotted lines), (2) rotor flux (dashed lines), and (3) rotor speed (solid line), over different operation points with the rotor circuit short-circuited. The left axis of Figure A.11 reads the real parts or real eigen values (blue lines), and the right axis reads the positive imaginary parts of eigen values (red lines). It can be observed that the machine is stable over the whole operating range, around the synchronous frequency (approximately 314 rad/s) the machine shifts from motor to generator. Notice that the eigen values of flux linkages are complex conjugated pairs. For example, the eigen value of the stator flux in d-axis is the complex conjugate of the eigen value of the stator flux in q-axis. Therefore these eigen values represent oscillatory modes. The mode corresponding to the rotor speed eigen value is a decaying mode since it only has a real part, which is negative. The electromechanical of this system is the combination of rotor flux linkages modes with rotor speed mode, that yields a decaying oscillatory mode.

A.3.4.3 Shaft stiffness and damping.

The simplest way of considering dynamic phenomena in wind turbine drive trains is to add a torsional degree of freedom. The wind turbine rotor (i.e. blades, and hub) is considered a lumped mass, and the drive train (i.e. low-speed shaft, gearbox, high-speed shaft, brake disc, and generator rotor coupling) is represented by torsional stiffness K_s , and damping D_s . Adding this torsional degree of freedom to the nonlinear system represented in Eq. A.3.4 is done by adding two states, one corresponding to the speed of the wind turbine rotor ω_h , and one representing the twisting of the low speed shaft δ_θ . Clearly, the nonlinearities remain the same, as illustrated in

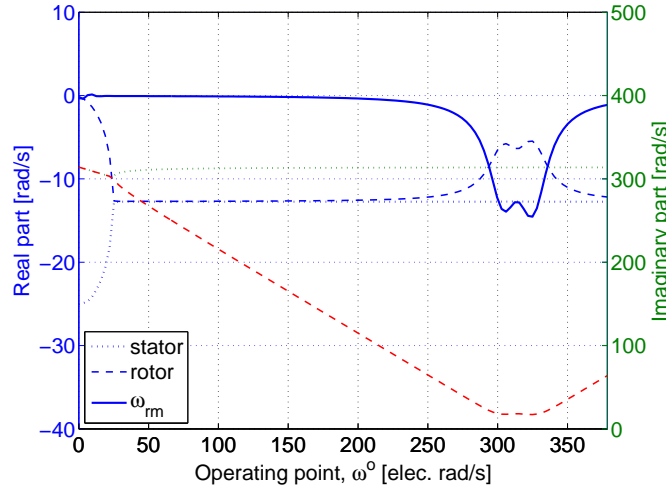


Figure A.11: Eigen values of asynchronous machine with short circuited rotor, over different operating points.

Eq. A.56.

$$\begin{bmatrix} \dot{\lambda}_{ds} \\ \dot{\lambda}_{qs} \\ \dot{\lambda}'_{dr} \\ \dot{\lambda}'_{qr} \\ \dot{\omega}_{re} \\ \dot{\omega}_h \\ \dot{\delta}_\theta \end{bmatrix} = \begin{bmatrix} \frac{R_s \mathcal{L}_r}{\mathcal{D}} & -\dot{\theta}_{ar} & \frac{-R_s \mathcal{L}_m}{\mathcal{D}} & 0 & 0 & 0 & 0 \\ \dot{\theta}_{ar} & \frac{R_s \mathcal{L}_r}{\mathcal{D}} & 0 & \frac{-R_s \mathcal{L}_m}{\mathcal{D}} & 0 & 0 & 0 \\ \frac{-R_r \mathcal{L}_m}{\mathcal{D}} & 0 & \frac{R_r \mathcal{L}_s}{\mathcal{D}} & \omega_{re} - \dot{\theta}_{ar} & 0 & 0 & 0 \\ 0 & \frac{-R_r \mathcal{L}_m}{\mathcal{D}} & \dot{\theta}_{ar} - \omega_{re} & \frac{R_r \mathcal{L}_s}{\mathcal{D}} & 0 & 0 & 0 \\ -A\lambda'_{qr} & A\lambda'_{dr} & 0 & 0 & -\frac{D_s}{N_{gb}^2 J_g} & \frac{p_f}{2} \frac{D_s}{J_g} & \frac{p_f}{2} \frac{K_s}{J_g} \\ 0 & 0 & 0 & 0 & \frac{2}{p_f} \frac{D_s}{J_w} & -\frac{D_s}{J_w} & -\frac{K_s}{J_w} \\ 0 & 0 & 0 & 0 & -\frac{2}{p_f} & 1 & 0 \end{bmatrix} \begin{bmatrix} \lambda_{ds} \\ \lambda_{qs} \\ \lambda'_{dr} \\ \lambda'_{qr} \\ \omega_{re} \\ \omega_h \\ \delta_\theta \end{bmatrix} + \begin{bmatrix} v_{ds} \\ v_{qs} \\ v'_{dr} \\ v'_{qr} \\ 0 \\ -\frac{T_L}{J_w} \\ 0 \end{bmatrix} \quad (\text{A.56})$$

A.3.5 Control of doubly-fed asynchronous generator.

Literature regarding control of electrical machines is extensive. The fundamental concepts, and techniques regarding control of asynchronous machines are presented in [90, 127, 132, 135]. Namely, simple schemes (i.e. volts-per-hertz control, constant-slip current control), as well as vector control (i.e. field-oriented: stator flux-, rotor flux-, stator voltage-, etc.), and direct torque control. Regarding the control of DFAG generators used in wind turbine applications, basic vector control is described in [3, 51, 74, 77, 94, 97, 136, 137]. Low voltage fault ride-through (FRT) control and dynamic performance is studied in [52, 74, 94, 96, 106, 138]. Reactive power control is treated in [139]. Regarding the case when the network voltage is unbalanced, control strategies to reduce torque and reactive power oscillations are shown

in [89, 102, 107, 140]. Coordinated control RSC, and GSC converters using positive, and negative sequences is demonstrated in [109]. Internal mode control (IMC) is applied to permanent magnet, and asynchronous machines in [141]. In this work the classical vector control is used, implemented as a cascade of proportional integral controls, where the cascade in the cascade of q -axis control active power, and the cascade of the d -axis controls reactive power. The cross-coupling between $d - q$ axes is neglected. It is considered that as long as the stator flux is constant, and the slip range is limited, cross-coupling and feed forward terms can be neglected [134].

A.3.5.1 Tuning

Tuning of controllers can be a lengthy task [49]. There are many standard analytical techniques to design control systems, for example: root locus analysis, frequency response analysis, or those based on a state space description of the system (i.e. pole placement, or quadratic optimal regulator) [142, 143]. Regarding back-to-back converters, in [136, 139, 144, 145] a description of tuning for different objectives can be found. The procedure essentially consists on deriving a simplify transfer function of the plant (i.e. electrical machine) to tune inner cascade loops (i.e. current control loops). Similarly, a simplified transfer function of the current control loop plus the machine model is derived to tune the outer control loops.

A.3.5.2 Filters and compensator

In general, a n th-order filter can be described by a transfer function $H(s)$, whose denominator $D(s)$, and numerator $N(s)$ are polynomials [146]. Based on the frequency band that a filter passes or rejects, they can be classified as [146]: band-pass, band-reject, low-pass, high-pass, and all-pass. For example, a typical second-order low-pass filter is Eq. A.58, where ω_c is the center frequency, the quality factor Q_f can be defined in terms of bandwidth (i.e. $\omega_h - \omega_l$), or damping ratio ζ Eq. A.59. A high Q_f would make the amplitude gain very high at ω_c , this concept is applied in resonant damping controllers of various types [89, 112, 113, 115, 117, 147, 148].

$$H(s) = H_0 \frac{s^n + b_{n-1}s^{n-1} + b_{n-2}s^{n-2} \dots b_1s + b_0}{s^n + a_{n-1}s^{n-1} + a_{n-2}s^{n-2} \dots a_1s + a_0} \quad (\text{A.57})$$

$$H_{\text{LP}}(s) = \frac{\omega_c}{s^2 + \frac{\omega_c}{Q_f}s + \omega_c^2} \quad (\text{A.58})$$

$$Q_f = \left\{ \frac{\omega_c}{\omega_h - \omega_l} \quad \text{or} \quad \frac{1}{2\zeta} \right. \quad (\text{A.59})$$

Lead, and lag compensators (i.e. all-pass filters) are used for example in power system stabilizers [76]. A lead compensator Eq. A.60-A.61, gives maximum phase lead ϕ_m at maximum phase frequency ω_m [149].

$$C(s) = \sqrt{\frac{p}{z}} \frac{s + z}{s + p} \quad (\text{A.60})$$

$$\omega_m = \sqrt{pz} \quad \text{and} \quad p > \omega_m > z > 0 \quad (\text{A.61})$$

Linear transformations

A linear transformation was introduced in Section A.3.2 to convert a function from a planar 3 dimensional vector space \mathbf{R}^3 to a planar orthogonal bidimensional vector space \mathbf{R}^2 . This kind of linear transformation is widely used in the simulation of electrical machines. Figure B.1 illustrates a set of functions of time $\mathbf{f}_{abc}(t)$, each one living in one dimension of a \mathbf{R}^3 -vector space, and their components in an orthogonal \mathbf{R}^2 -vector space. If $\mathbf{f}_{abc}(t)$ fullfils Eq. B.1, then the transformation is given by Eq. B.2.

$$f_a(t) + f_b(t) + f_c(t) = 0 \quad (\text{B.1})$$

$$\begin{aligned} \begin{bmatrix} f_d \\ f_q \end{bmatrix} &= \begin{bmatrix} \cos(\beta) & \cos(\beta - \frac{2\pi}{3}) & \cos(\beta + \frac{2\pi}{3}) \\ \sin \beta & \sin(\beta - \frac{2\pi}{3}) & \sin(\beta + \frac{2\pi}{3}) \end{bmatrix} \quad \text{with} \quad (\text{B.2}) \\ -\cos(\alpha) &= \cos(\beta + \frac{2\pi}{3}) & -\cos(\delta) &= \sin(\beta - \frac{2\pi}{3}) \\ \sin(\alpha) &= \sin(\beta + \frac{2\pi}{3}) & -\sin(\delta) &= \cos(\beta - \frac{2\pi}{3}) \end{aligned}$$

B.1 Inversion of transformation matrix

Using linear transformations to model electrical machines allows to reduce the number of equations, and to avoid matrices with time-dependent coefficients that need to be inverted every time step and that are difficult to invert

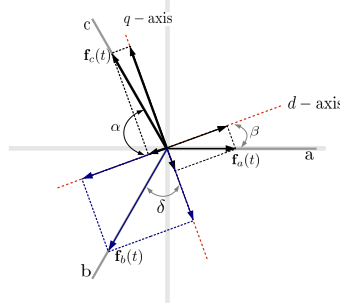


Figure B.1: Illustration of linear transformation.

analytically (i.e. the inductance matrix). However, using the linear transformation also involves at some point inverting the transformation matrix \mathbf{K}_t . In the literature is mentioned that \mathbf{K}_t^{-1} can be obtained by means of matrix algebra, and trigonometric relationships, however such procedure is lengthy and cumbersome. An easier way to obtain an analytical solutions is using a numerical linear algebra package to obtain a complementary matrix that is diagonal, and that can be used to find \mathbf{K}_t^{-1} using its transpose \mathbf{K}_t^\top . The procedure is as follows:

1. Orthogonality condition:

$$\mathbf{A}\mathbf{A}^{-1} = \mathbf{A}\mathbf{A}^\top = \mathbf{I}$$

2. Observe that although \mathbf{K}_t is not orthogonal, there exists a complementary matrix $\mathbf{c} = \text{diag}[c_1 \ c_2 \ c_3]$, such that:

$$\begin{aligned} \mathbf{K}_t \mathbf{K}_t^\top &= \mathbf{I} \mathbf{c} \\ \mathbf{c}^{-1} \mathbf{K}_t \mathbf{K}_t^\top &= \mathbf{I} \end{aligned}$$

3. Taking the transpose of Eq. B.3 yields:

$$(\mathbf{c}^{-1} \mathbf{K}_t)^\top \mathbf{K}_t = \mathbf{I} \quad (\text{B.3})$$

4. By observation:

$$\begin{aligned} \mathbf{K}_t^{-1} &= (\mathbf{c}^{-1} \mathbf{K}_t)^\top \\ &= \mathbf{c}^{-1} \mathbf{K}_t^\top \end{aligned}$$

DFAG initialization

Initialization of the DFAG machine, is important for power system dynamic simulations [74, 150]. It can also be handy to speed up the simulation process. Furthermore, the exercise of initializing the DFAG helps to get a better understanding of the performance of the machine under different control inputs which was illustrated in the phase-plots of Section A.2.1.2.

It is relatively straight forward to calculate the initial values of the control voltage V_r . In [74] the principle of superposition is used to develop a set of algebraic equations that express stator, and rotor power in terms of stator, and rotor voltages. Constraint equations defined by the control conditions complete a system of equations which is solved by iteration. [150] derives algebraic relationships in order to find a direct solution for rotor voltages given an operating point (i.e. apparent power, and voltage at the terminals of the machine from a network load flow calculation). It does so using a simplified equivalent circuit model of DFAG, where the magnetizing branch is moved to the terminal of the stator (i.e. a -more- *approximate equivalent circuit* according to text books), to derive torque and reactive power balance equation. Ultimately, rotor voltages are expressed in terms of machine parameters, stator voltage, and algebraic constants. One of the algebraic constants is the solutions to a quadratic equation, therefore correct solution has to be chosen according to the desired (or allowable) speed range, and rotor voltage limits. The same concept is used in [31], to derive what is referred to as the *steady-state control laws*, the objective is to avoid a nested optimization loop within an optimization routine for DFAG design. Given electromagnetic torque, stator voltage, and power factor, [31] uses a Thevenin equivalent circuit of DFAG to derive stator current, and rotor

voltage. Rotor current is derived from DFAG equivalent circuit.

Here circuit equations (derived straight forward from Eq. A.3 without superposition), plus constraint equations (defined by control conditions and power flow relationships of DFAG) are expressed in their real, and imaginary parts in order to complete a system of algebraic nonlinear equations in real numbers that can be solved using standard Matlab routines in `fsolve`. The system of equation is given by Eq. C.1, where the variables are printed in gray. Machine parameters (R_s , R'_r , X_s , X_m , X'_r), and control conditions (s , P_{ref} , Q_{ref}) are printed in black. Given the design data in Figure C.1a and $Q_{\text{ref}} = 0$, the corresponding values of the control variable V'_r are shown in Figure C.1b.

$$\begin{aligned}
R_s \cdot \text{Re}[I_s] - (X_s + X_m) \cdot \text{Im}[I_s] - X_m \cdot \text{Im}[I'_r] - \text{Re}[V_s] &= 0 \\
(X_s + X_m) \cdot \text{Re}[I_s] + R_s \cdot \text{Imag}[I_s] + X_m \cdot \text{Re}[I'_r] - \text{Imag}[V_s] &= 0 \\
\frac{R'_r}{s} \cdot \text{Re}[I'_r] - (X_m + X'_r) \cdot \text{Imag}[I'_r] - X_m \cdot \text{Imag}[I_s] - \frac{1}{s} \cdot \text{Re}[V'_r] &= 0 \\
(X_m + X'_r) \cdot \text{Re}[I'_r] + \frac{R'_r}{s} \cdot \text{Imag}[I'_r] + X_m \cdot \text{Re}[I_s] - \frac{1}{s} \cdot \text{Imag}[V'_r] &= 0 \\
3(\text{Re}[V_s] \cdot \text{Re}[I_s] + \text{Imag}[V_s] \cdot \text{Imag}[I_s]) - P_s &= 0 \\
3(\text{Imag}[V_s] \cdot \text{Re}[I_s] - \text{Re}[V_s] \cdot \text{Imag}[I_s]) - Q_s &= 0 \\
3(\text{Re}[V'_r] \cdot \text{Re}[I'_r] + \text{Imag}[V'_r] \cdot \text{Imag}[I'_r]) - P_r &= 0 \\
3(\text{Imag}[V'_r] \cdot \text{Re}[I'_r] - \text{Re}[V'_r] \cdot \text{Imag}[I'_r]) - Q_r &= 0 \\
P_s + P_r - P_{\text{ref}} &= 0 \\
Q_s - Q_r - Q_{\text{ref}} &= 0
\end{aligned} \tag{C.1}$$

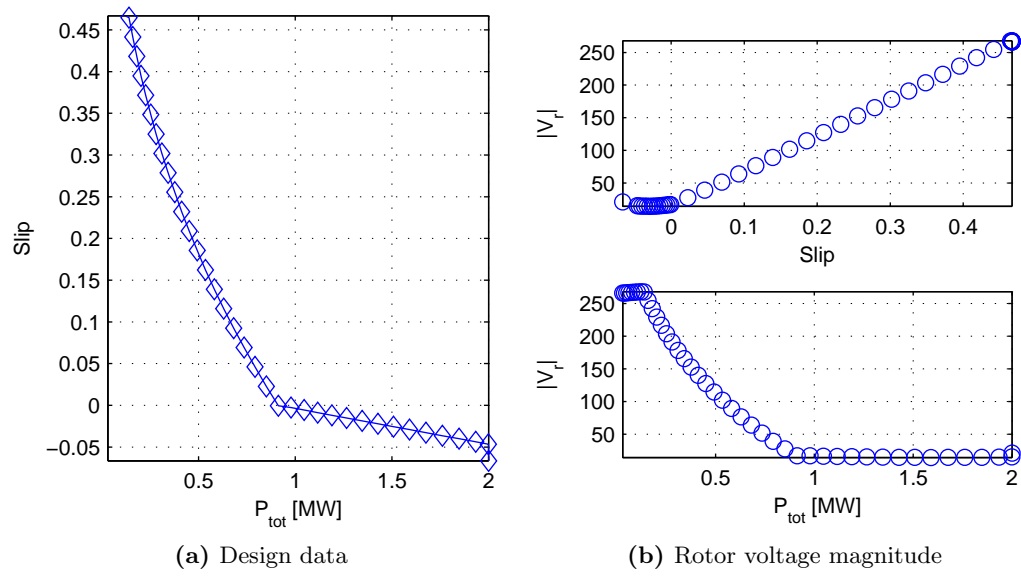


Figure C.1: Initialization of DFAG control variables

Toy example in HAWC2

This section presents a *toy* example of the construction of a simple multibody system in HAWC2. It is an exercise on constructing input files, understanding the structural data required as input, and using some of the interfaces for HAWC2. First, a system consisting of a rod, and a disc is modeled. The natural frequency of the system is calculated and simulated in HAWC2 to demonstrate the meaning of the input parameters of the structural data file. Then a 3-body system resembling a shaft with two discs at the ends is modeled to illustrate the response of a wind turbine drive train to loads.

D.1 Natural frequency of disc-rod system

The disc-rod system is illustrated in Figure D.1. The analytical solution for the natural frequency of the system due to torsional vibration, is quite simple considering that the inertia, and mass of the shaft are negligible. It is analogous to that of a cantilever beam with a concentrated mass in the free end, subject to a vertical force. Therefore, analogously to Hooke's law for the beam, the equation of motion for the system in Figure D.1 is given by Eq. D.1

$$J\ddot{\theta} = -k\theta \tag{D.1}$$

$$\ddot{\theta} + \frac{k}{J}\theta = 0$$

where the moment of inertia J , is the volume integral of the perpendicular distance r from the axis of rotation to the mass differential dm (Eq. D.2).

In the case of a cylinder it comes down to Eq. D.3.

$$J = \int_{\mathcal{V}} r^2 dm \quad (\text{D.2})$$

$$J = \frac{1}{2} m R^2 \quad (\text{D.3})$$

The constant k (Eq. D.4) represents the torque that would make a twist equal to one radian on the shaft, it is therefore a measure of the torsional stiffness of the shaft.

$$k = \frac{\pi d^4}{32} \frac{G}{l} \quad (\text{D.4})$$

The equation of motion D.1, is a ordinary differential equation whose general solution is a sum of periodic functions [151], as expressed by Eq. D.5

$$\theta = \theta_0 \cos pt + \frac{\dot{\theta}_0}{p} \sin pt \quad (\text{D.5})$$

where $p^2 = \frac{k}{J}$, θ_0 and $\dot{\theta}_0$ are the initial position and angular speed respectively. The frequency of the sinusoidal functions, the natural frequency due to torsional vibrations, is then given by Eq. D.6.

$$f = \frac{1}{2\pi} \sqrt{\frac{k}{J}} \quad (\text{D.6})$$

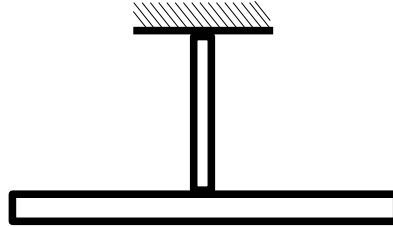


Figure D.1: Disc-rod system

Example: Table D.1 shows the data of a disc-rod system. The natural frequency calculated using Eq. D.6 is 2.88 Hz.

	d [m]	l [m]	$\frac{m}{l}$ [kg/m]	E [N/m ²]	G [N/m ²]
disc	80.0	3.0	2.0238e3	2.100e11	8.100e10
rod	1.0	5.0	1.0000	2.100e11	8.100e10

Table D.1: Data for disc-rod system

In order to compare the former calculation to a simulation in HAWC2, the system of Figure D.1 was built, a time simulation was run with the system excited by a torque impulse, and the frequency characteristics were observed. The process of building the system in HAWC2 is essentially

1. Main input file (containing two bodies, oriented as described by the picture, the shaft constrained with `fix0`, and disc-shaft constrained with `fix1`)
2. Structural input file
3. Matlab interface used to apply forces

Regarding the structural data most of the inputs are straight forward, however one must pay attention to the fact that the inputs to HAWC2 are *per unit length*. For the quantities related to the geometry of the cross sectional area it is not relevant, but for those quantities that relate to the mass (i.e. moments of inertia) it must be considered for a better understanding of the meaning of the inputs. The quantities related to geometry are the area moments of inertia I_x , I_y , and I_z (referred to as *torsional stiffness constant* K in [45]). These correspond in the structural data file to columns number 11, 12, and 13 respectively. In the case of a solid cylinder, they are given by equations D.7.

$$\begin{aligned} I_x &= \frac{\pi R^4}{4} \\ I_y &= I_x \\ I_z &= 2I_x \end{aligned} \tag{D.7}$$

The so-called *radius of inertia*, inputs corresponding to columns 5 and 6 in the structural data file [45], is defined by Eq. D.8 with respect to x - and y -axis

$$\begin{aligned} r_{J_x} &= \sqrt{\frac{J_x}{(m/l)}} \\ r_{J_y} &= \sqrt{\frac{J_y}{(m/l)}} \end{aligned} \tag{D.8}$$

where the moments of inertia *per unit length* with respect to x - and y -axis are

$$\begin{aligned} J_x &= \int_A \rho_l y^2 dx dy \\ J_y &= \int_A \rho_l x^2 dx dy \end{aligned} \tag{D.9}$$

whose for the case of a solid cylinder come to

$$\begin{aligned} J_x &= (m/l) \frac{R^2}{4} \\ J_y &= (m/l) \frac{R^2}{4} \end{aligned} \quad (\text{D.10})$$

The simulation in HAWC2 of disc-rod system with the data from table D.1 yields a frequency of 2.872 Hz, as it can be observe from Figure D.2.

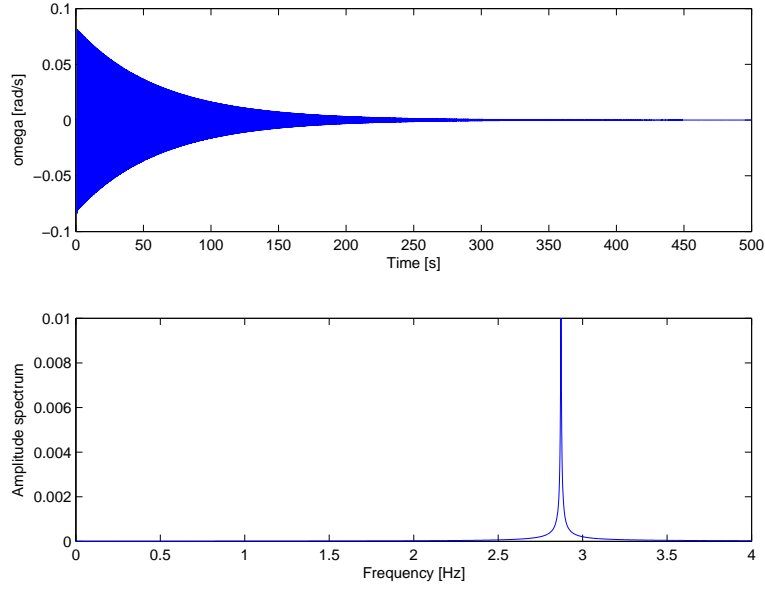


Figure D.2: Natural frequency of disc-rod system

D.2 Simulation of disc-shaft-disc system

In this section a disc-shaft-disc system as that of Figure D.3 is simulated in HAWC2 with the objective of illustrating and testing Matlab interfacing with HAWC2. The derivation of the analytical formula of the free - free torsional vibration for this system is similar to that of the disc-rod system [151], but includes the inertia of both discs attached to the ends of the shaft. The formula is given by Eq. D.11. The data for the discs and shaft is given in table D.2. In this case the analytical solution yields a frequency of 7.226 Hz.

$$f = \frac{1}{2\pi} \sqrt{\frac{k(J_1 + J_2)}{J_1 J_2}} \quad (\text{D.11})$$

	d [m]	l [m]	$\frac{m}{l}$ [kg/m]	E [N/m ²]	G [N/m ²]
disc 1	80.0	3.0	2.0238e3	2.100e11	8.100e10
shaft	1.0	5.0	1.0000	2.100e11	8.100e10
disc 2	2.0	1.0	1.8346e6	2.100e11	8.100e10

Table D.2: Data of disc-shaft-disc system

D.2.1 Free - free torsional vibration

The simulation in HAWC2 yields a frequency of approximately 7.09 Hz, as can be seen from Figure D.4, that shows the time response of the angular speed of the shaft at the bearing and its frequency spectrum.

D.2.2 Numerical damping

HAWC2 uses a Newmark solver scheme, which is commonly use to solve linear and nonlinear structural dynamics problems. The equations of motion of a nonlinear structure can be formulates as Eq. D.12, where \mathbf{M} is the mass matrix, \mathbf{C} viscous damping matrix, \mathbf{g} vector of nonlinear internal forces, \mathbf{F}_t , \mathbf{q} nodal displacements.

$$\mathbf{M}\ddot{\mathbf{q}}_t + \mathbf{C}\dot{\mathbf{q}}_t + \mathbf{g}(\mathbf{q}_t) = \mathbf{f}_t \quad (\text{D.12})$$

The viscous damping matrix \mathbf{C} , is normally set heuristically to fit the expected response of the structure in question. In this simulation exercise, structural damping was set to zero. In order to understand the weight of numerical damping on the dynamic response of a structure modeled with HAWC2.

A standard Newmark integration scheme, that considers acceleration to be

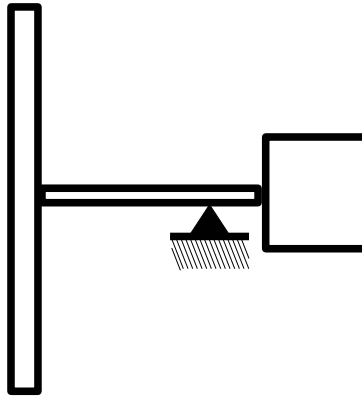


Figure D.3: Disc-shaft-disc system

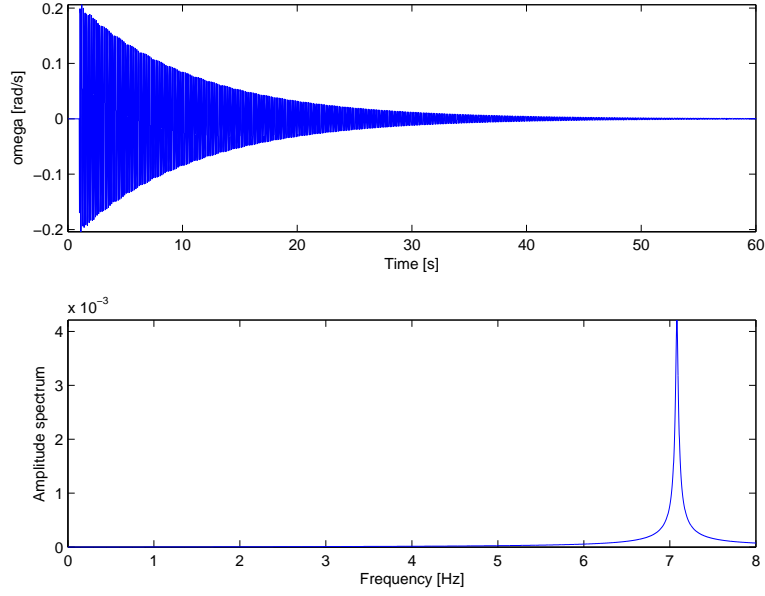


Figure D.4: Natural frequency of disc-shaft-disc system –with $\beta = 0.27$ and $\gamma = 0.51$

linear within a time step, can be expressed as in Eq. D.13. For the integration method to be stable, the right combination of time step size Δt , and parameters β , γ for a given system is required. Figure D.5 shows the response of the disc-shaft-disc system with different β , and γ parameters than those used for the simulation in Figure D.4.

$$\begin{aligned} \mathbf{q}_{t+\Delta t} &= \mathbf{q}_t + \Delta t \dot{\mathbf{q}}_t + \frac{\Delta t^2}{2} [(1 - 2\beta)\ddot{\mathbf{q}}_t + 2\beta\ddot{\mathbf{q}}_{t+\Delta t}] \\ \dot{\mathbf{q}}_{t+\Delta t} &= \dot{\mathbf{q}}_t \Delta t [(1 - \gamma)\ddot{\mathbf{q}}_t + \gamma\ddot{\mathbf{q}}_{t+\Delta t}] \end{aligned} \quad (\text{D.13})$$

D.3 Summary

The multibody formulation in HAWC2 allows in principle to build any kind of multibody problem. An insight into the structural formulation, constraint setting, external interfaces, structural and numerical damping, and solver was gained from building simple models, and analyzing their time and frequency response.

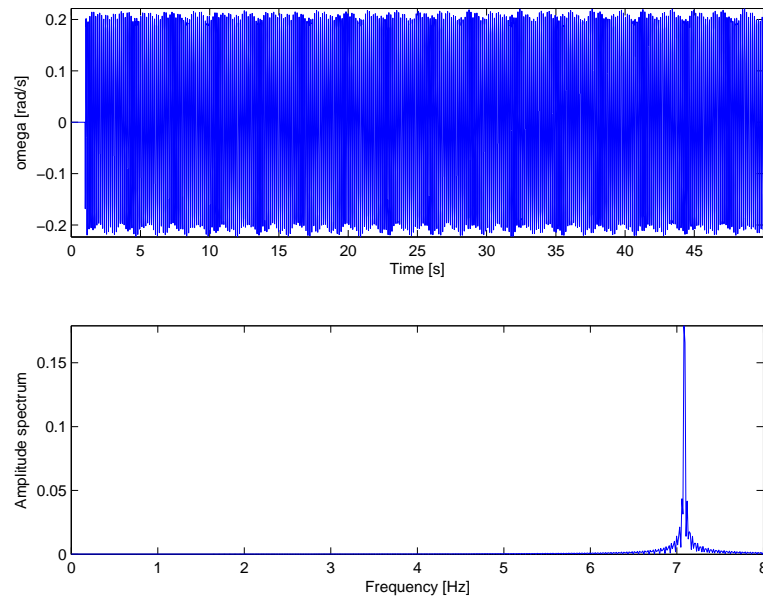


Figure D.5: Natural frequency of disc-shaft-disc system –with –with $\beta = 0.26$ and $\gamma = 0.50$

Bibliography

- [1] F. Iov, F. Blaabjerg, and A. D. Hansen, "A simulation platform to model, optimize and design wind turbines - the matlab/simulink toolbox," *The Annals of "DUNAREA DE JOS" University of Galati*, vol. FASCICLE III, no. ISSN 1221-454X, 2002.
- [2] F. Iov, A. D. Hansen, P. Sørensen, and F. Blaabjerg, "Simulation platform to model, optimize and design wind turbines," Tech. Rep. ISBN 87-89179-45-5, Aalborg University and Risø National Laboratory, 2004.
- [3] F. Iov, A. D. Hansen, P. Sørensen, and F. Blaabjerg, "Wind Turbine Blockset in Matlab/Simulink. General Overview and Description of the Model," tech. rep., Aalborg University, 2004.
- [4] B. Skaare, T. Hanson, F. Nielsen, R. Yttervik, A. M. Hansen, K. Thomsen, and T. J. Larsen, "Integrated dynamic analysis of floating offshore wind turbines," *Proceedings of the International Conference on Offshore Mechanics and Arctic Engineering - OMAE*, no. 9780791837771, 2006.
- [5] E. N. Hinrichsen and P. Nolan, "Dynamics and stability of wind turbine generators," *IEEE Transactions on Power Apparatus and Systems*, vol. PAS-101, pp. 2640–2648, August 1982.
- [6] E. N. Hinrichsen, "Analysis methods for wind turbine control and electrical system dynamics," Tech. Rep. 95N27984, National Aeronautics and Space Administration (NASA), May 1995.
- [7] A. D. Hansen, N. A. Cutululis, and F. Iov, "Grid faults' impact on wind turbine structural loads," in *Nordic Wind Power Conference*, 2007.

- [8] R. Fadaeinedjad, G. Moschopoulos, and M. Moallem, "Voltage Sag Impact on Wind Turbine Tower Vibration," in *IEEE Power Engineer Society General Meeting*, 2007.
- [9] R. Fadaeinedjad, M. Moallem, and G. Moschopoulos, "Simulation of a Wind Turbine with Doubly Fed Induction Generator by FAST and Simulink," *IEEE Transactions on Energy Conversion*, vol. 23, pp. 690–700, 2008.
- [10] G. Ramtharan, N. Jenkins, O. Anaya-Lara, and E. Bossanyi, "Influence of rotor structural dynamics representations on the electrical transient performance of fsig and dfig wind turbines," *Wind Energy*, vol. 10, pp. 293–301, March 2007.
- [11] M. Zaaier, "Review of knowledge development for the design of offshore wind energy technology," *Wind Energy*, vol. 12, no. 5, pp. 411–430, 2009.
- [12] F. M. Huges, O. Anaya-Lara, G. Ramtharan, N. Jenkins, and G. Strbac, "Influence of Tower Shadow and Wind Turbulence on the Performance of Power System Stabilizers for DFIG-Based Wind Farms," *IEEE Transactions on Energy Conversion*, vol. 23, pp. 519–528, 2008.
- [13] R. Fadaeinedjad, G. Moschopoulos, and M. Moallem, "Flicker contribution of a wind turbine in a stand-alone wind diesel system," in *CCECE/CCGEI*, 2008.
- [14] R. Fadaeinedjad, G. Moschopoulos, and M. Moallem, "Investigation of voltage sag impact on wind turbine tower vibrations," *Wind Energy*, 2008.
- [15] N. A. Cutululis, A. D. Hansen, T. J. Larsen, P. Sørensen, and F. Iov, "Wind turbines structural loads during fault ride-through operation," in *European Wind Energy Conference*, 2008.
- [16] A. D. Hansen, N. A. Cutululis, F. Iov, and B. Barahona, "Integrated electrical design of DFIG wind turbines for power system studies," in *Nordic Wind Power Conference*, 2009.
- [17] R. Fadaeinedjad, G. Moschopoulos, and M. Moallem, "The Impact of Tower Shadow, Yaw Error, and Wind Shears on Power Quality in a Wind-Diesel System," *IEEE Transactions on Energy Conversion*, vol. 24, pp. 102 – 111, 2009.
- [18] D. Kaufer, N. Cosack, C. Böker, M. Seidel, and M. Kühn, "Integrated analysis of the dynamics of offshore wind turbines with arbitrary support structures," in *European Wind Energy Conference*, 2009.

- [19] A. D. Hansen, N. A. Cutululis, H. Markou, and P. E. Sørensen, "Impact of fault ride-through requirements on fixed-speed wind turbine structural loads," *Wind Energ.*, vol. 14, no. 1, pp. 1–11, 2011.
- [20] J. Sanz-Corretge, A. García-Barace, and I. Egaña, "Load transient analysis of wind turbine drive train under grid disturbances," in *European Wind Energy Conference*, 2010.
- [21] B. Barahona, L. C. Henriksen, A. D. Hansen, N. A. Cutululis, and P. Sørensen, "Coupling of HAWC2 and Matlab: Towards an Integrated Simulation Platform," in *European Wind Energy Conference*, April 2010.
- [22] B. S. Kallesøe, T. J. Larsen, and U. S. Paulsen, "Aero-Hydro-Elastic Simulation Platform for Wave Energy Systems and floating Wind Turbines," tech. rep., Risø DTU, 2011.
- [23] A. Heege, Y. Radovic, and J. Betran, "Fatigue load computation of wind turbine gearboxes by coupled structural, mechanism and aerodynamic analysis," *DEWI Magazin*, vol. 28, pp. 61 – 68, 2006.
- [24] G. Ramtharan, N. Chris, and B. Ervin, "Importance of advanced simulations of electrical transients in wind turbines," in *European Wind Energy Conference*, April 2010.
- [25] K. F. Hulme, "Development of CASCADE - a test simulator for modeling multidisciplinary design optimization problems in distributed computing environment," Master's thesis, State University of New York, 1996.
- [26] K. F. Hulme and C. L. Bloebaum, "Development of a multidisciplinary design optimization test simulator," *Structural and Multidisciplinary Optimization*, vol. 14, pp. 129–137, 1997. 10.1007/BF01812515.
- [27] K. Hulme and C. Bloebaum, "A comparison of formal and heuristic strategies for iterative convergence of a coupled multidisciplinary analysis," in *World Congresses of Structural and Multidisciplinary Optimization*, 1999.
- [28] R. Filomeno Coelho, P. Breitkopf, and C. Knopf-Lenoir, "Model reduction for multidisciplinary optimization - application to a 2d wing," *Structural and Multidisciplinary Optimization*, vol. 37, pp. 29–48, Dec. 2008.
- [29] Yoshida, "Wind turbine tower optimization method using a genetic algorithm," *Wind Eng. (UK)*, vol. 30, no. 6, pp. 453–469, 2006.

- [30] G. Q.-V. J. R. M. Olimpo Anaya-Lara, ZiFa Liu, "Optimal dfig crowbar resistor design under different controllers during grid faults," *DRPT2008*, 2008.
- [31] D. Aguglia, P. Viarouge, R. Wamkeue, and J. Cros, "Analytical determination of steady-state converter control laws for wind turbines equipped with doubly fed induction generators," *IET Renew. Power Gener.*, vol. 2, no. 1, pp. 16–25, 2008.
- [32] W. Xudong, W. Z. Shen, W. J. Zhu, J. N. SÅžrensen, and C. Jin, "Shape optimization of wind turbine blades," *Wind Energ.*, vol. 12, no. 8, pp. 781–803, 2009.
- [33] D. Aguglia and R. Rebeschini, "Power transformer role for gearbox mechanical stress mitigation during voltage dips applied to doubly-fed induction generator based wind turbines," in *European Wind Energy Conference*, 2010.
- [34] L. Sass, *Symbolic Modeling of Electromechanical Multibody Systems*. PhD thesis, Université catholique de Louvain, 2004.
- [35] R. Kübler and W. Schiehlen, "Modular simulation in multibody system dynamics," *Multibody System Dynamics*, vol. 4, pp. 107 – 127, 2000.
- [36] B. Gu and H. H. Asada, "Co-simulation of algebraically coupled dynamic subsystems without disclosure of proprietary subsystem models," *Journal of Dynamic Systems, Measurement, and Control*, vol. 126, pp. 1 – 13, 2004.
- [37] G. M. Hulbert, Z.-D. Ma, and J. Wang, "Gluing for dynamic simulation of distributed mechanical systems," in *Advances in Computational Multibody Systems*, pp. 69 – 94, Springer, 2005.
- [38] C. Batlle and A. Doria-Cerezo, "Energy-based modelling and simulation of the interconnection of a back-to-back converter and a doubly-fed induction machine," in *American Control Conference*, 2006.
- [39] T. G. van Engelen, "Control design based on aero-hydro-servo-elastic linear models from TURBU," tech. rep., Energy Research Centre of the Netherlands (ECN), 2007.
- [40] H. Song and Y. Qu, "Energy-based modelling and control of wind energy conversion system with dfig," *International Journal of Control*, vol. 84, pp. 281–292, Feb. 2011.
- [41] J. A. C. Ambrósio, "Multibody dynamics: Bridging for multidisciplinary applications," in *XXI ICTAM*, 2004.

- [42] J. Peeters, *Simulation of Dynamic Drive Train Loads in a Wind Turbine*. PhD thesis, Katholieke Universiteit Leuven - Faculteit Ingenieurswetenschappen, 2006.
- [43] P. Passon, M. Kühn, S. Butterfield, J. Jonkman, and T. Larsen, “OC3—Benchmark Exercise of Aero-elastic Offshore Wind Turbine Codes,” in *The Science of Making Torque from Wind*, no. 012071 in Journal of Physics: Conference Series 75, 2007.
- [44] J. Jonkman, “FAST - an aeroelastic design code for horizontal axis wind turbines.” <http://wind.nrel.gov/designcodes/simulators/fast/>, December 2011.
- [45] T. J. Larsen, “How 2 HAWC2, the user’s manual,” tech. rep., Risø DTU, January 2009.
- [46] SIMPACK, “Multi-Body Simulation Software.” <http://www.simpack.com/industrial-sectors-wind.html>, December 2011.
- [47] Politecnico di Milano, “MBDyn - MultiBody Dynamics Software.” <http://www.aero.polimi.it/~mbdyn/>, December 2011.
- [48] S. Miller, “Wind turbine model.” <http://www.mathworks.com/matlabcentral/fileexchange/25752-wind-turbine-model>, April 2011.
- [49] S. Dominguez and W. Leithead, “Control Design Toolbox for Large-Scale PRVS Wind Turbines,” in *European Wind Energy Conference (EWEC)*, 2007.
- [50] A. D. Hansen, F. Iov, P. Sørensen, N. Cutululis, C. Jauch, and F. Blaabjerg, “Dynamic wind turbine models in power system simulation tool digsilent,” Tech. Rep. Risø-R-1400(ed.2)(EN), Risø DTU, 2007.
- [51] A. D. Hansen, P. Sørensen, F. Iov, and F. Blaabjerg, “Control of variable speed wind turbines with doubly-fed induction generators,” *Wind Engineering*, vol. 28, no. 4, pp. 411 – 432, 2004.
- [52] A. D. Hansen and G. Michalke, “Fault ride-through capability of DFIG wind turbines,” *Renewable Energy*, vol. 32, pp. 1594 – 1610, December 2006.
- [53] A. D. Hansen, G. Michalke, P. Sørensen, T. Lund, and F. Iov, “Co-ordinated voltage control of DFIG wind turbines in uninterrupted operation during grid faults,” *Wind Energy*, vol. 10, no. 1, pp. 51–68, 2007.

- [54] DIgSILENT GmbH, *DIgSILENT Technical Documentation - Power-Factory DSL Models*, August 2008.
- [55] A. Gole and A. Daneshpooy, "Towards Open: Systems A PSCAD/EMTDC to MATLAB Interface," in *ISPT '97*, June 1997.
- [56] S. Uski, B. Lemström, J. Kiviluoma, S. Rissanen, and P. Antikainen, "Adjoint wind turbine modeling with ADAMS, Simulink and PSCAD/EMTDC," in *Nordic Wind Power Conference*, VTT Processes, Energy Production, March 2004.
- [57] S. Wünsche, C. Clauß, P. Schwarz, and F. Winkler, "Electro-thermal circuit simulation using simulator coupling," *IEEE TRANSACTIONS ON VERY LARGE SCALE INTEGRATION (VLSI) SYSTEMS*, vol. 3, pp. 277 – 282, 1997.
- [58] M. C. Ferris, "Matlab and GAMS: Interfacing Optimization and Visualization Software," *University of Wisconsin, Computer Science Department*.
- [59] R. Choy and A. Edelman, "Parallel MATLAB: Doing it Right," *Proceedings of the IEEE*, vol. 93, pp. 331–341, February 2005.
- [60] The MathWorks Inc., *MATLAB Distributed Computing Server 4.0*.
- [61] The MathWorks, Inc., *MATLAB External Interfaces*, online ed., October 2008.
- [62] The MathWorks Inc., *Writing S-functions*, on line ed., October 2008.
- [63] A. S. Tanenbaum, *Computer Networks*. Pearson Education International, 4 ed., 2003.
- [64] The MathWorks, Inc., *Instrument Control Toolbox*, online ed., July 2005.
- [65] E. J. Mayhew, "Building a Distributed Aircraft Tracking Simulation Using TCP/IP," *MATLAB Digest*, July 2005.
- [66] B. Barahona, P. B. Adersen, A. D. Hansen, N. A. Cutululis, and P. Sørensen, "Integrated design of wind power systems: MATLAB-HAWC2 interface," in *50th International Conference of Scandinavian Simulation Society (SIMS 50)*, 2009.
- [67] R. Thomson, *TCP/IP Socket Communications in MATLAB*. The-MathWorks, online ed., August 2008.
- [68] B. S. Kallesøe, "HAWC2 - Course," in *Course lectures*, May 2009.

- [69] J. L. Peeters, D. Vandepitte, and P. Sas, "Analysis of internal drive train dynamics in a wind turbine," *Wind Energy*, vol. 9, pp. 141 – 161, 2006.
- [70] A. M. Hansen, "Detailed nacelle dynamics –Research in Aeroelasticity EFP-2006," Tech. Rep. Risø-R-1611, Risø DTU, July 2007.
- [71] T. J. Larsen, M. H. Hansen, and F. Iov, "Generator Dynamics in Aeroelastic Analysis and Simulations," tech. rep., Risø DTU, 2003.
- [72] N. A. Cutululis, T. J. Larsen, P. Sørensen, F. Iov, and A. D. Hansen, "Electrical Components Library for HAWC2," tech. rep., Risø DTU, 2007.
- [73] T. J. Larsen, "Slip generator model implemented in HAWC2 as an external DLL," Note J.nr. 200500523, Risø, 2005.
- [74] V. Akhmatov, *Analysis of Dynamic Behaviour of Electric Power Systems with Large Amount of Wind Power*. PhD thesis, Technical University of Denmark, 2003.
- [75] O. Anaya-Lara, N. Jenkins, J. Ekanayake, P. Cartwright, and M. Huges, *Wind Energy Generation: Modelling and Control*. Wiley, 2009.
- [76] P. Kundur, *Power System Stability and Control*. McGraw-Hill, 1994.
- [77] G. Michalke, *Variable Speed Wind Turbines - Modelling, Control and Impact on Power Systems*. PhD thesis, Darmstadt Technical University, 2008.
- [78] J. Ekanayake and N. Jenkins, "Comparison of the response of doubly fed and fixed-speed induction generator wind turbines to changes in network frequency," *IEEE Transactions on Energy Conversion*, vol. 19, pp. 800 – 802, 2004.
- [79] L. Holdsworth, I. Charalambous, N. Jenkins, J. Ekanayake, J. Ekanayake, and N. Jenkins, "Power system fault ride through capabilities of induction generator based wind turbines," *Wind Eng.*, vol. 28, no. 4, pp. 399–409, 2004.
- [80] J. Morren, J. Pierik, and S. W. de Haan, "Inertial response of variable speed wind turbines," *Electric Power Systems Research*, vol. 76, pp. 980 – 987, 2006.
- [81] A. Mullane and M. O'Malley, "The inertial response of induction-machine-based wind turbines," *IEEE Transactions on Power Systems*, vol. 20, pp. 1496 –1503, 2005.

- [82] J. Morren, S. W. de Haan, W. L. Kling, and J. Ferreira, "Wind turbines emulating inertia and supporting primary frequency control," *IEEE Transactions on Power Systems*, vol. 21, pp. 433 – 434, 2006.
- [83] N. R. Ullah, T. Thiringer, and D. Karlsson, "Temporary primary frequency control support by variable speed wind turbines - potential and applications," *IEEE Transactions on Power Systems*, vol. 23, pp. 601 – 612, 2008.
- [84] G. C. Tarnowski, P. C. Kjær, P. E. Sørensen, and J. Østergaard, "Study on variable speed wind turbines capability for frequency response," in *European Wind Energy Conference*, 2009.
- [85] G. C. Tarnowski, P. C. Kjær, P. Sørensen, and J. Østergaard, "Variable speed wind turbines capability for temporary over-production," in *IEEE Power & Energy Society General Meeting*, pp. 1 – 7, 2009.
- [86] B. Rawn, *Ensuring safe exploitation of wind turbine kinetic energy: and invariance kernel formulation*. PhD thesis, Graduate Department of Electrical and Computer Engineering University of Toronto, 2009.
- [87] B. Barahona, "Integrated design and control of wind turbines." Conference contribution - [Slide show presentation] Presented at: 4. Wind Energy Systems Workshop, 2010, Risø (DK), Status: unpublished, November 2010.
- [88] B. Barahona, C. Wessels, A. D. Hansen, and P. Sørensen, "Loads on DFIG wind turbines due to unbalanced voltage faults," in *7th PhD Seminar on Wind Energy in Europe*, European Academy of Wind Energy (EAWE), October 2011.
- [89] T. K. A. Brekken and N. Mohan, "Control of a doubly fed induction wind generator under unbalance grid voltage conditions," *IEEE Transactions on Energy Conversion*, vol. 22, pp. 129 – 135, March 2007.
- [90] P. C. Krause, O. Wasynczuk, and S. D. Sudhoff, *Analysis of Electric Machinery and Drive Systems*. IEEE Press Series on Power Engineering, WileyBlackwell, 2 ed., 2002.
- [91] F. Iov, A. D. Hansen, P. Sørensen, and N. Cutululis, "Mapping of grid faults and grid codes," tech. rep., Risø National Laboratory - Technical University of Denmark, 2007.
- [92] Z. Yong, D. Zhengang, and L. Xuelian, "Comparison of grid code requirements with wind turbine in china and europe," in *Power and Energy Engineering Conference (APPEEC), 2010 Asia-Pacific*, pp. 1 –4, March 2010.

- [93] V. Akhmatov, "Variable-speed wind turbines with doubly-fed induction generators part i: Modelling in dynamic simulation tools," *Wind Engineering*, vol. 26, no. 2, pp. 85 – 108, 2002.
- [94] J. B. Ekanayake, L. Holdsworth, X. Wu, and N. Jenkins, "Dynamic modeling of double fed induction generator wind turbines," *IEEE Transactions on Power Systems*, vol. 18, pp. 803 – 809, 2003.
- [95] S. M. Bolik, *Modelling and Analysis of variable speed Wind Turbines with Induction Generator during grid fault*. PhD thesis, Institute of Energy Technology, Aalborg University, 2004.
- [96] O. Anaya-Lara, X. Wu, P. Cartwright, J. Ekanayake, and N. Jenkins, "Performance of Doubly Fed Induction Generator (DFIG) During Network Faults," *Wind Engineering*, vol. 29, pp. 49 – 66, 2005.
- [97] A. Petersson, *Analysis, Modeling and Control of Doubly-Fed Induction Generators for Wind Turbines*. PhD thesis, Chalmers University of Technology, 2005.
- [98] J. Fortmann, S. Engelhardt, J. Kretschmann, C. Feltes, and P. I. Erlich, "Validation of an RMS DFIG Simulation Model According to New German Model Validation Standard FGW TR4 at Balanced and Unbalanced Grid Faults," in *8th International Workshop on Large-Scale Integration of Wind Power into Power Systems as well as on Transmission Networks for Offshore Wind Farms*, 2009.
- [99] V. Akhmatov, B. Andresen, J. N. Nielsen, K. H. Jensen, N. M. Goldenbaum, J. Thisted, and M. Frydensbjerg, "Unbalanced short-circuit faults: Siemens wind power full scale converter interfaced wind turbine model and certified fault-ride-through validation," in *European Wind Energy Conference & Exhibition*, 2010.
- [100] V. Akhmatov, J. Nygaard, K. H. Jensen, N. Goldenbaum, J. Thisted, M. Frydensbjerg, and B. Andresen, "Siemens wind power variable-speed full scale frequency converter wind turbine model for balanced and unbalanced short-circuit faults," *Wind Engineering*, vol. 34, no. 2, pp. 139 – 156, 2010.
- [101] E. Muljadi, T. Batan, D. Yildirim, and C. Butterfield, "Understanding the unbalance-voltage problem in wind turbine generation," in *IAS Annual Meeting (IEEE Industry Applications Society)*, vol. 2, pp. 1359 – 1365, 1999.
- [102] T. Brekken and N. Mohan, "A novel doubly-fed induction wind generator control scheme for reactive power control and torque pulsation compensation under unbalanced grid voltage conditions," in *PESC*, vol. 2, pp. 760 – 764, 2003.

- [103] O. Gomis-Bellmunt, A. Junyent-Ferre, A. Sumper, and J. Bergas-Jan, "Ride-through control of a doubly fed induction generator under unbalanced voltage sags," *IEEE Trans. On Energy Conversion*, vol. 23, no. 4, pp. 1036–1045, 2008.
- [104] G. Abad, M. Rodriguez, G. Iwanski, and J. Poza, "Direct power control of doubly-fed-induction-generator-based wind turbines under unbalanced grid voltage," *IEEE Trans. Power Electron.*, vol. 25, no. 2, pp. 442–452, 2010.
- [105] M. Kiani and W.-J. Lee, "Effects of voltage unbalance and system harmonics on the performance of doubly fed induction wind generators," *IEEE Trans. on Ind. Applicat.*, vol. 46, no. 2, pp. 562–568, 2010.
- [106] D. Xiang, L. Ran, P. J. Tavner, and S. Yang, "Control of a doubly fed induction generator in a wind turbine during grid fault ride-through," *IEEE Transactions on Energy Conversion*, vol. 21, pp. 652 – 662, 2006.
- [107] L. Xu and Y. Wang, "Dynamic Modeling and Control of DFIG-Based Wind Turbines Under Unbalanced Network Conditions," *IEEE Transactions on Power Systems*, vol. 22, pp. 314 –323, 2007.
- [108] D. Santos-Martin, J. Rodriguez-Amenedo, and S. Arnalte, "Direct power control applied to doubly fed induction generator under unbalanced grid voltage conditions," *IEEE Trans. Power Electron.*, vol. 23, no. 5, pp. 2328–2336, 2008.
- [109] L. Xu, "Coordinated Control of DFIG's Rotor and Grid Side Converters During Network Unbalance," *IEEE Transactions on Power Electronics*, vol. 23, no. 3, pp. 1041 – 1049, 2008.
- [110] P. Flannery and G. Venkataramanan, "Unbalanced voltage sag ride-through of a doubly fed induction generator wind turbine with series grid-side converter," *IEEE Trans. on Ind. Applicat.*, vol. 45, no. 5, pp. 1879–1887, 2009.
- [111] P. Zhou, Y. He, and D. Sun, "Improved direct power control of a dfig-based wind turbine during network unbalance," *IEEE Trans. Power Electron.*, vol. 24, no. 11, pp. 2465–2474, 2009.
- [112] J. Hu, Y. He, L. Xu, and B. Williams, "Improved Control of DFIG Systems During Network Unbalance Using PI-R Current Regulators," *IEEE Trans. Ind. Electron.*, vol. 56, no. 2, pp. 439–451, 2009.
- [113] J. Hu and Y. He, "Reinforced control and operation of dfig-based wind-power-generation system under unbalanced grid voltage conditions," *IEEE Trans. Energy Convers.*, vol. 24, no. 4, pp. 905–915, 2009.

- [114] S. Z. Chen, N. C. Cheung, K. C. Wong, and J. Wu, "Integral sliding-mode direct torque control of doubly-fed induction generators under unbalanced grid voltage," *IEEE Transactions on Energy Conversion*, vol. 25, no. 2, 2010.
- [115] C. Wessels, F. Gebhardt, and F. W. Fuchs, "Fault ride-through of a dfig wind turbine using a dynamic voltage restorer during symmetrical and asymmetrical grid faults," *IEEE Transactions on Power Electronics*, vol. 26, no. 4-4, 2011.
- [116] H. Nian, Y. Song, P. Zhou, and Y. He, "Improved direct power control of a wind turbine driven doubly fed induction generator during transient grid voltage unbalance," *IEEE Trans. Energy Convers.*, vol. 26, no. 3, pp. 976–986, 2011.
- [117] R. Teodorescu, F. Blaabjerg, M. Liserre, and P. Loh, "Proportional-resonant controllers and filters for grid-connected voltage-source converters," *IEE Proceedings - Electric Power Applications*, vol. 153, no. 5, pp. 750–762, 2006.
- [118] B. Barahona, N. A. Cutululis, A. D. Hansen, and P. Sørensen, "Unbalanced voltage faults: the impact on structural loads of DFIG wind turbines," *submitted to Wind Energy*, January 2012.
- [119] P. H. Madsen, S. Frandsen, W. E. Holley, and J. C. Hansen, "Dynamics and fatigue damage of wind turbine rotors during steady operation," Tech. Rep. Risø-R-512, Risø National Laboratory, July 1984.
- [120] H. Hendriks and B. Bulder, "Fatigue Equivalent Load Cycle Method. A General Method to Compare the Fatigue Loading of Different Load Spectrums," Tech. Rep. ECN-95-074, ECN, October 1995.
- [121] F. Mouzakis, E. Morfiadakis, and P. Dellaportas, "Fatigue loading parameter identification of a wind turbine operating in complex terrain," *Journal of Wind Engineering and Industrial Aerodynamics*, vol. 82, pp. 69 – 88, November 1998.
- [122] G. Freebury and W. Musial, "Determining equivalent damage loading for full-scale wind turbine blade fatigue tests," in *19th American Society of Mechanical Engineers Wind Energy Symposium*, American Society of Mechanical Engineers (ASME), January 2000.
- [123] S. T. Frandsen, "Turbulence and turbulence-generated structural loading in wind turbine clusters," tech. rep., Risø National Laboratory, January 2007.

- [124] A. Nieslony, "Rain flow counting algorithm." Matlab Central, <http://www.mathworks.com/matlabcentral/fileexchange/3026>, April 2010.
- [125] R. P. Downey, "Uncertainty in wind turbine life equivalent load due to variation of site conditions," Master's thesis, Technical University of Denmark, May 2006.
- [126] P. Sen, *Principles of Electric Machines and Power Electronics*. John Wiley & Sons, 1997.
- [127] C.-M. Ong, *Dynamic Simulation of Electric Machinery using Matlab/Simulink*. Prentice Hall PRT, 1998.
- [128] T. Wildi, *Electrical Machines, Drives and Power Systems*. Prentice Hall, 2005.
- [129] T. Lund and P. Sørensen, "Reactive Power Capability of a Wind Turbine with Doubly Fed Induction Generator," *Wind Energy*, vol. 10, pp. 379 – 394, 2007.
- [130] S. Engelhardt, I. Erlich, C. Feltes, J. Kretschmann, and F. Shewarega, "Reactive Power Capability of Wind Turbines Based on Doubly Fed Induction Generators," *IEEE Transactions on Energy Conversion*, vol. 26, pp. 364 – 372, 2011.
- [131] P. K. Kovács, *Transient phenomena in electrical machines*. ELSEVIER, 1984.
- [132] P. Vas, *Sensorless vector and direct torque control*. OXFORD UNIVERSITY PRESS, 1998.
- [133] T. Thiringer, *Measurements and Modelling of Low-Frequency Disturbances in Induction Machines*. PhD thesis, Chalmers University of Technology, 1996.
- [134] F. Iov, F. Blaabjerg, and A. D. Hansen, "Analysis of a variable-speed wind energy conversion scheme with doubly-fed induction generator," *International Journal of Electronics*, vol. 90, no. 11-12, pp. 779 – 794, 2003.
- [135] W. Leonhard, *Control of Electrical Drives*. Springer, 3rd ed., 2001.
- [136] R. Pena, J. Clare, and G. Asher, "Doubly fed induction generator using back-to-back PWM converters and its application to variable-speed wind-energy generation," *IEE Proc.-Electr. Power Appl.*, vol. 143, pp. 231 – 241, 1996.

- [137] N. Quang, A. Dittrich, and A. Thieme, "Doubly-fed induction machine as generator: control algorithms with decoupling of torque and power factor," *Electrical Engineering*, vol. 80, pp. 325 – 335, 1997.
- [138] S. Seman, J. Niiramen, and A. Arkkio, "Ride-through analysis of doubly fed induction wind-power generator under unsymmetrical network disturbance," *IEEE Transactions on Power Systems*, vol. 21, no. 4, pp. 1782 – 1789, 2006.
- [139] B. C. Rabelo, W. Hofmann, J. L. da Silva, R. G. de Oliveira, and S. R. Silva, "Reactive power control design in doubly fed induction generators for wind turbines," *IEEE Transactions on Industrial Electronics*, vol. 56, pp. 4154 – 4162, 2009.
- [140] O. S. Ebrahim, P. K. Jain, and G. Nishith, "New control scheme for the wind-driven doubly fed induction generator under normal and abnormal grid voltage conditions," *Journal of Power Electronics*, vol. 8, pp. 10 – 22, January 2008.
- [141] L. Harnefors and H.-P. Nee, "Model-Based Current Control of AC Machines Using the Internal Model Control Method," *IEEE Trans. On Industry Applications*, vol. 34, pp. 133 – 141, 1998.
- [142] E. Ceangă, C. Nichita, L. Protin, and N. A. Cutululis, *Théorie de la commande des systèmes*. Editura Tehnică, 1997.
- [143] K. Ogata, *Modern Control Engineering*. Prentice Hall, 4 ed., 2001.
- [144] C. Bajracharya, M. Molinas, J. A. Suul, and T. M. Undeland, "Understanding of tuning techniques of converter controllers for VSC-HVDC," in *Nordic Workshop on Power and Industrial Electronics (NORPIE)*, June 2008.
- [145] A. Constantin, "Advanced Modelling and Control of Wind Power Systems," Master's thesis, Aalborg University, 2009.
- [146] K. Lacanette, "A Basic Introduction to Filters -Active, Passive, and Switched-Capacitor," Application Note 779, National Semiconductor, April 1995.
- [147] Y. W. Li, F. Blaabjerg, D. M. Vilathgamuwa, and P. C. Loh, "Design and comparison of high performance stationary-frame controllers for dvr implementation," *IEEE Trans. Power Electron.*, vol. 22, no. 2, pp. 602–612, 2007.
- [148] A. G. Yepes, F. D. Freijedo, O. Lopez, and J. Doval-Gandoy, "Analysis and design of resonant current controllers for voltage-source converters by means of nyquist diagrams and sensitivity function," *IEEE Trans. Ind. Electron.*, vol. 58, no. 11, pp. 5231–5250, 2011.

- [149] W. Messner, M. Bedillion, L. Xia, and D. Karns, "Lead and lag compensators with complex poles and zeros design formulas for modeling and loop shaping," *IEEE Control Syst. Mag.*, vol. 27, no. 1, pp. 44–54, 2007.
- [150] Holdsworth, Wu, Ekanayake, and Jenkins, "Direct solution method for initialising doubly-fed induction wind turbines in power system dynamic models," *IEE proceedings. Generation, transmission and distribution*, vol. 150, no. 3, pp. 334–342, 2003.
- [151] S. Timoshenko, *Vibration Problems in Engineering*. D. van Nostrand Company, Inc., 1937.

www.vindenergi.dtu.dk

DTU Wind Energy
Technical University of Denmark
Frederiksborgvej 399
DK-2800 Kgs. Lyngby
Denmark
Tel: (+45) 46 77 46 77
Fax: (+45) 46 77 56 88
E-mail: risoe@risoe.dk